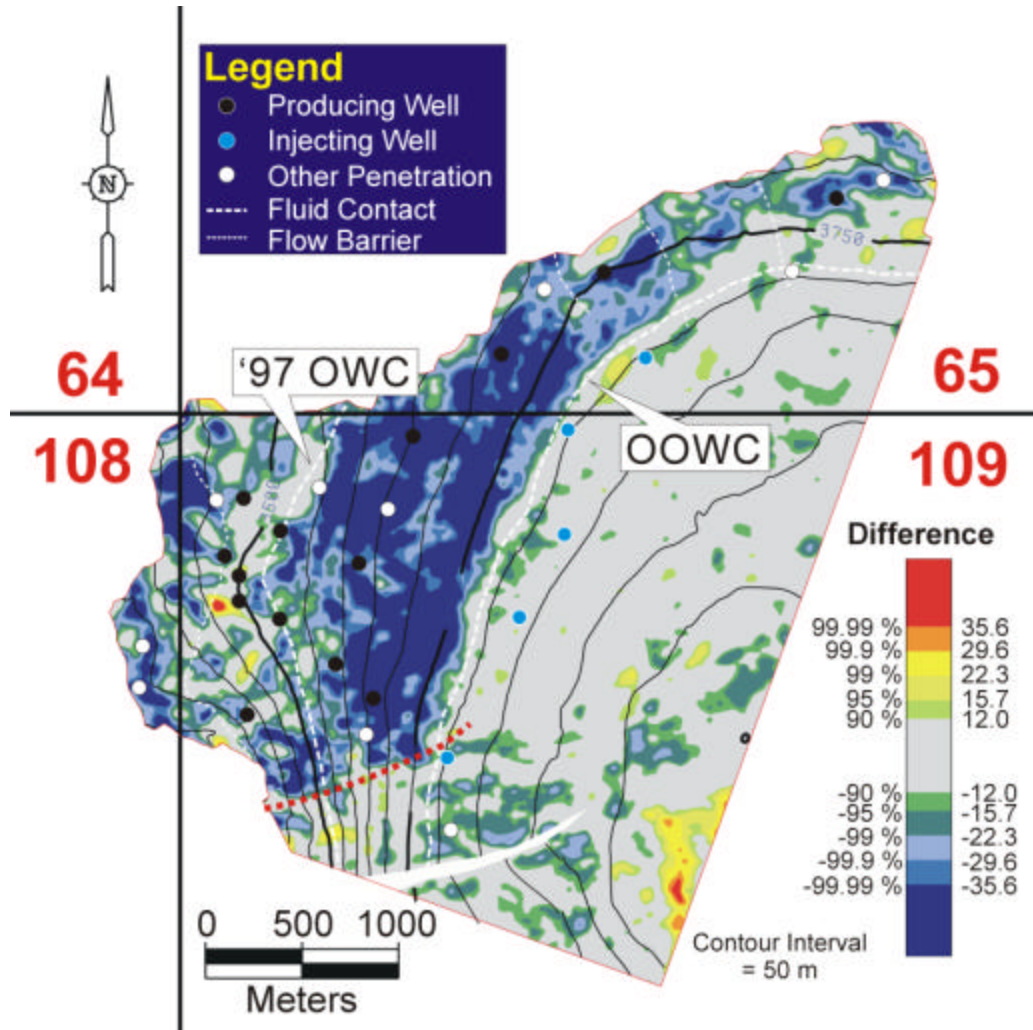


# IMAGING DRAINAGE OF TURBIDITE RESERVOIRS THROUGH TIME-LAPSE SEISMIC ANALYSIS AT BULLWINKLE, GREEN CANYON BLOCK 65, OFFSHORE GULF OF MEXICO



ALASTAIR SWANSTON  
The Pennsylvania State University  
December 2001

The Pennsylvania State University  
The Graduate School  
College of Earth and Mineral Sciences

**IMAGING DRAINAGE OF TURBIDITE RESERVOIRS THROUGH TIME-LAPSE  
SEISMIC ANALYSIS AT BULLWINKLE, GREEN CANYON BLOCK 65,  
OFFSHORE GULF OF MEXICO**

A Thesis in  
Geosciences  
by  
Alastair Swanston

Copyright 2001 Alastair Swanston

Submitted in Partial Fulfillment  
of the Requirements  
for the Degree of

Master of Science

December 2001

We approve the thesis of Alastair Swanston.

Date of Signature

---

Peter B. Flemings  
Associate Professor of Geosciences  
Thesis Advisor

---

Kevin P. Furlong  
Professor of Geosciences

---

Turgay Ertekin  
Professor of Petroleum and Natural Gas Engineering

---

Peter Deines  
Professor of Geochemistry  
Associate Head for Graduate Programs and Research

I grant The Pennsylvania State University the non-exclusive right to use this work for the University's own purposes and to make single copies of the work available to the public on a not-for-profit basis if copies are not otherwise available.

---

Alastair Swanston

## ABSTRACT

Two orthogonal pre-production seismic surveys and a seismic survey acquired after eight years of production from the Bullwinkle field (GC 65, Gulf of Mexico) reveal extraordinary seismic differences that are attributed to production-induced changes in rock and fluid properties. Separate normalizations of these surveys demonstrate that time-lapse results are improved by utilizing seismic surveys that were acquired in similar orientations, and also that clearer difference images are obtained from comparing lower frequency datasets. Amplitude reduction is documented where production and log data show that water has replaced hydrocarbons as the oil-water-contact moved upwards. A smaller decrease in seismic amplitude in response to sediment compaction is also observed in the aquifer of the main reservoir sand. An otherwise convincing time-lapse result from the near-perpendicularly orientated surveys is undermined by dimming above the oil water contact and lower aquifer correlation. This provides a warning of the danger of using dissimilar baseline and monitor surveys. After normalization, the non-whitened (lower frequency) surveys are more similar than the whitened surveys, and give the clearest image of large changes in seismic events. At Bullwinkle, this occurs to some extent at the expense of the ability to resolve smaller hydrocarbon reservoirs. Spectral whitening may therefore be useful if it is necessary to investigate changes in closely stacked reservoirs sands.

## Contents

List of Figures	vi
List of Tables	x
Acknowledgements	xi
Introduction	1
Background	4
The Bullwinkle Field	4
3-D Seismic Surveys	6
Normalization Methodology	7
Rebinning	8
Global Shifting	8
Frequency Filtering	9
Wiener Filtering	9
Amplitude Scaling	10
Statistical Analysis	11
Quantifying Repeatability	11
Correlation	11
Regression Model	12
RMS Ratio	13
Prediction Bands	13
Results	14
Aquifer Volume Statistics	14
Horizon Statistics	15
Differencing	16
J2 Differences	17
Interpretation	19
Influence of Orientation and Bandwidth	19
Orientation	19
Bandwidth	22

J2 Drainage	24
Discussion	27
Conclusion	32
Appendix A: RMS Ratio - Correlation Coefficient Relationship	62
RMS Ratio	62
Correlation Coefficient	63
Appendix B: Seismological Characterization of Bullwinkle	64
Summary	64
Bullwinkle 3-D Seismic Survey Overview	64
Offset	66
Differences in Processing	66
Integration and Phase	67
Frequency	68
Depth Conversion	70
Amplitude and Structure Maps	71
J4 Sand	71
J3 Sand	72
J2 Sand	73
J1 Sand	74
I10 and Rocky Sands	75
Conclusion	76
References	109

## List of Figures

1.	Basemap showing the location of the Bullwinkle Field in the Gulf of Mexico	34
2.	Green Canyon basemap depicting the baseline and monitor 3-D seismic surveys.	35
3.	J2 amplitude and structure map showing the 4-D Volume, the Aquifer Volume, the J2 Aquifer Horizon, and the J2 Reservoir Horizon.	36
4.	Seismic section illustrating the vertical extent of the 4-D Volume and the Aquifer Volume.	37
5.	Power spectra of the survey volumes before and after normalization	38
	(a) 1988 E-W HF and 1997 data	
	(b) 1988 E-W HF' and 1997a' data	
	(c) 1988 N-S HF and 1997 data	
	(d) 1988 N-S HF' and 1997b' data	
	(e) 1988 N-S LF and 1997 data	
	(f) 1988 N-S LF' and 1997c'	
6.	Cross-equalization filters used to reshape the 1997 data to match the 1988 data	39
	(a) E-W HF cross-equalization filter	
	(b) N-S HF cross-equalization filter	
	(c) N-S LF cross-equalization filter	
7.	Correlation coefficient, RMS ratio, and RMS Amplitude during each normalization step as a function of travel time.	40
	(a) The E-W HF normalization	
	(b) The N-S HF normalization	
	(c) The N-S LF normalization	
	(d) Final correlation achieved in the three normalizations	
8.	Cross-plots of normalized 1997 amplitudes vs. normalized 1988 amplitudes from the Aquifer Volume	41
	(a) The E-W HF normalization	
	(b) The N-S HF normalization	
	(c) The N-S LF normalization	
9.	Cross-plots of normalized 1997 amplitudes vs. normalized 1988 amplitudes in the N-S LF normalization	42
	(a) The G2 Horizon	
	(b) The J2 Aquifer Horizon	
	(c) The J2 Reservoir Horizon	



10.	Travel-time difference map of the 1988 N-S LF' and 1997c' J2 horizons	43
11.	J2 amplitude and difference maps in the E-W HF normalization	44
	(a) 1997a' amplitude map	
	(b) 1997 original amplitude map	
	(c) 1988 E-W HF' amplitude map	
	(d) 1988 E-W HF' – 1997a' difference map	
12.	J2 amplitude and difference maps in the N-S HF normalization	45
	(a) 1997b' amplitude map	
	(b) 1997 original amplitude map	
	(c) 1988 N-S HF' amplitude map	
	(d) 1988 N-S HF' – 1997b' difference map	
13.	J2 amplitude and difference maps in the N-S LF normalization	46
	(a) 1997c' amplitude map	
	(b) 1997 original amplitude map	
	(c) 1988 N-S LF' amplitude map	
	(d) 1988 N-S LF' – 1997c' difference map	
14.	J2 difference maps displayed with prediction band color scales	47
	(a) E-W HF J2 differences	
	(b) N-S HF J2 differences	
15.	Diagrammatic Amplitude Histograms for the 1988 E-W HF and 1988 N-S HF surveys	48
	(a) Flat Aquifer Region	
	(b) Dipping Reservoir Region	
16.	N-S LF J2 difference map displayed with the N-S LF Aquifer Volume prediction band color scale	49
17.	Extracted traces and production history plot from wells 109-1 and A-32-BP	50
	(a) 1988 N-S LF' and 1997c' traces extracted from the location of well 109-1	
	(b) Well A-32-BP production history	
18.	Extracted traces and production history plot from well A-33	51
	(a) 1988 N-S LF' and 1997c' traces extracted from the location of well A-33	
	(b) Well A-33 production history	
19.	Cross-section showing the upper J2 seismic discontinuity in the 1988 N-S HF survey	52
20.	J1 difference maps displayed with prediction band color scales	53
	(a) N-S HF J1 differences	
	(b) N-S LF J1 differences	

21.	Correlation coefficient between two Ricker wavelets separated by 4 ms as a function of center frequency	54
B-1.	Green Canyon basemap depicting the Bullwinkle 3-D seismic surveys.	77
B-2.	Offset tapering functions used on the 1988 and 1997 data	78
B-3.	Theoretical zero-phase and integrated trace image of an oil-filled sand (a) Thick sand body (b) Thin sand body	79
B-4.	Seismic survey power spectra (a) 1988 E-W HF data (b) 1988 N-S HF data (c) 1988 N-S LF data (d) 1997 data	80
B-5.	Map showing the J-sand bounding polygons	81
B-6.	Type dip-section from the 1988 E-W HF survey (wiggle trace)	82
B-7.	Type dip-section from the 1988 E-W HF survey (variable density)	83
B-8.	Type dip-section from the 1988 N-S HF survey (variable density)	84
B-9.	Type dip-section from the 1988 N-S LF survey (variable density)	85
B-10.	Type dip-section from the 1997 survey (variable density)	86
B-11.	Diagram illustrating the back-interpolation method of depth error estimation	87
B-12.	1988 E-W HF J4 Amplitude and Structure Map	88
B-13.	1988 N-S HF J4 Amplitude and Structure Map	89
B-14.	1997 J4 Amplitude and Structure Map	90
B-15.	1988 E-W HF J3 Amplitude and Structure Map	91
B-16.	1988 N-S HF J3 Amplitude and Structure Map	92
B-17.	1988 N-S LF J3 Amplitude and Structure Map	93
B-18.	1997 J3 Amplitude and Structure Map	94

B-19.	1988 E-W HF J2 Amplitude and Structure Map	95
B-20.	1988 N-S HF J2 Amplitude and Structure Map	96
B-21.	1988 N-S LF J2 Amplitude and Structure Map	97
B-22.	1997 J2 Amplitude and Structure Map	98
B-23.	1988 E-W HF J1 Amplitude and Structure Map	99
B-24.	1988 N-S HF J1 Amplitude and Structure Map	100
B-25.	1988 N-S LF J1 Amplitude and Structure Map	101
B-26.	1997 J1 Amplitude and Structure Map	102
B-27.	1988 E-W HF I10 and Rocky Amplitude and Structure Map	103
B-28.	1988 N-S HF I10 and Rocky Amplitude and Structure Map	104
B-29.	1988 N-S LF I10 and Rocky Amplitude and Structure Map	105
B-30.	1997 I10 and Rocky Amplitude and Structure Map	106

## List of Tables

1. Nomenclature	55
2. Definition of Acronyms and Abbreviations	56
3. Seismic Survey Acquisition and Processing Flow Summary	58
4. Global Shifts and High-Cut Filters Applied to the 1997 Data	59
5. Aquifer Volume Statistics	59
6. Horizon Amplitude Extraction Statistics	60
7. Final Correlation Coefficients and Difference Volume Standard Deviations	60
8. Prediction Band Widths	61
9. Comparison of Achieved Repeatability in Time-Lapse Studies	61
B-1 Appendix B Nomenclature	107
B-2 Comparison of Minimum Resolvable Thickness	108

## ACKNOWLEDGEMENTS

This research is part of the Penn State Petroleum GeoSystems Initiative, which is sponsored by Shell Exploration and Production Company (SEPCo), the Shell Foundation, IBM and Landmark Graphics. Additional support was provided by the Penn State Time-lapse Consortium, whose members include Chevron, Conoco, Statoil, and Texaco. Shell were very helpful in providing and releasing much of the data used in this project. Software support was supplied by AVS, Lamont 4-D, the Landmark Graphics Corporation and Mincom Ltd.

I am indebted to T. Burkhart, M. Kohli, and T. C. Jones of SEPCo. for their helpful advice and support. Tucker Burkhart provided the foundation for this thesis through his excellent time-lapse analysis of South Timbalier 295. He always generously took time out of his busy schedule to answer any of my questions swiftly and elegantly.

I would like to thank Dr. Peter Flemings for his guidance and support in shaping both this thesis, and my graduate career. I am also very grateful for his unwavering confidence in my abilities, and for his efforts to help me secure employment in a position that will allow me to continue to develop my keen interest in time-lapse seismology.

My fellow Petroleum GeoSystems teammates, Kevin Best and Joe Comisky, have played instrumental parts in this research. Beyond that, they have been great friends, lab-partners and roommates. I would like to thank the whole Basin Research Group for their cheerful assistance. A special mention goes to Aaron Janssen and Nate Kaleta who supplied me with many intriguing geophysical discussions and invaluable computational advice. My thesis committee members, Dr. Kevin Furlong, and Dr. Turgay Ertekin, have

also given me useful advice and suggestions. I am grateful to everyone in the Department of Geosciences for making my time in Pennsylvania so enjoyable.

My greatest thanks go to my parents and loved ones back in Britain. They have been the defining influence in my life, and have given me enormous support and encouragement to pursue all that I could ever wished to have done.

## INTRODUCTION

Time-lapse seismic analysis is the study of two or more seismic surveys acquired over the same location at different times, and has the principle aim of imaging movement of reservoir fluids in response to production. This is possible because changes in fluid saturation and reservoir pressure can produce differences in seismic response (Landrø et al, 1999). If rock-properties and structure are assumed to be time-invariant during production then, ideally, the only differences observed in the seismic surveys should be those due to production effects. Time-lapse datasets are often referred to as 4-D seismic because the passage of calendar time provides an additional dimension to the 3-dimensional seismic surveys that are usually acquired over today's hydrocarbon fields.

Time-lapse studies have the potential to increase the lifespan of declining fields through the identification of bypassed pay zones (Lumley, 2001). They may be used to optimize the number and location of infill wells to access these untapped reserves, or to accelerate production (Koster et al., 2000). 4-D seismic analysis can map reservoir compartmentalization, determine fluid-flow properties of faults, and monitor the progress of expensive enhanced oil recovery (EOR) processes (Lumley, 2001).

Primary production of a water drive reservoir causes the oil-water contact to migrate up dip. Modeling and observation demonstrates that regions in which water has replaced oil will undergo an increase in acoustic impedance (Wang et al., 1991). Conversely, the exsolution of free gas into a reservoir can significantly decrease the rock's impedance (Lumley, 2001). The acoustic properties of a hydrocarbon reservoir can also be altered during primary production by changes in pressure and temperature (Batzle and Wang, 1992).

This study uses seismic surveys shot for exploration purposes to study the drainage of the water-drive J2 reservoir of the Bullwinkle field (Green Canyon 65) in the Gulf of Mexico (Figure 1). Two seismic surveys were acquired orthogonally to each other in early 1988, one year before production from the field commenced (O'Connell et al., 1993). These surveys have since been reprocessed, which included a spectral whitening procedure to increase resolution. We compare these surveys with a survey acquired in 1997, after over eight years of production from the field (Figure 2).

We perform a poststack normalization procedure that builds upon the method presented by Burkhart et al. (2000) in order to maximize the similarity between the seismic data in zones unaffected by production. We then statistically characterize the similarity between the surveys in these zones to determine the significance of the differences that we observe in the reservoir.

We investigate the influence of survey orientation and spectral whitening on time-lapse repeatability and interpretability by performing separate normalizations of the two whitened 1988 surveys with the 1997 survey, and with both of the whitened and non-whitened versions of the 1988 survey acquired in a closer direction to the 1997 survey. Additionally, we compare the time-lapse seismic amplitude changes in the J2 reservoir with independent evidence of drainage from log and production data, and show that the observed differences are compatible with changes predicted by Gassmann modeling.

Intuition and seismic modeling suggest that it is desirable to compare surveys shot in the same orientation. The Bullwinkle seismic surveys provide one of the few data sets where this can be tested in practice. O'Connell et al. (1993) show that the perpendicular orientation of the 1988 surveys results in differing stratigraphic resolution of sediments in



the Bullwinkle basin. This is due to ray path distortions caused by Bullwinkle's complex salt geometry, by vertical and lateral velocity gradients, and by different sampling intervals in the down dip direction.

The J2 event exhibits strong and consistent amplitude reduction (dimming) in the water-swept section of the reservoir. We observe fewer significant changes above the 1997 oil-water-contact, although some updip areas display brightening as a consequence of gas exsolution. However, the degree of amplitude increase is perhaps reduced by sediment compaction and the influx heavier hydrocarbons from lower in the reservoir. Compaction also causes the J2 aquifer to reduce in amplitude over calendar time.

Our statistical analysis of time-lapse repeatability, combined with interpretations of the difference results, demonstrates that time-lapse analyses involving surveys with closer acquisition directions produces normalized surveys with greater similarity and more meaningful differences. We use the same techniques to quantify the benefit of spectral whitening on our Bullwinkle time-lapse efforts. Several workers have presented methods to equalize bandwidth in 4-D data. Bandpass filtering (Burkhart et al, 2000) and cross-equalization (Rickett and Lumley, 2001) are common approaches, whereas Davies and Warner (1999) present a more complex neural network approach. However, less work has been published on the desirability of high frequencies and spectral balancing in time-lapse analysis.

We use a Wiener cross-equalization filter (Robinson and Treitel, 1967) to match the frequency content of the 1997 survey to both the whitened and non-whitened versions of the N-S 1988 survey. We find that the whitened data exhibits more variable differences, and provides a poorer quality J2 difference result. However, the Bullwinkle

J-sands consist of several closely stacked turbidite hydrocarbon reservoirs, which are generally below tuning thickness. A study of the superjacent J1 event reveals that the whitened data, with its improved stratigraphic resolution, results in an improved difference image. Therefore, we conclude that spectral whitening can have a role to play in time-lapse analysis in certain situations.

## **BACKGROUND**

### ***The Bullwinkle Field***

The Bullwinkle Field lies 240 km southwest of New Orleans, Louisiana, in Green Canyon blocks 64, 65 and 109 (Figure 1). The water depth ranges from 400-550 m (O'Connell et al., 1993). It is situated along the western margin of a Plio-Pleistocene salt withdrawal mini-basin (Holman and Robertson, 1994). The field was discovered in 1983 and initial production began in July 1989 from a 60-slot conventional platform. Total reserves are estimated at 160 MMBOE (Million barrels of oil-equivalent), of which over 130 MMBOE have been produced to date.

The majority of the reserves are contained in five interconnected deepwater channel and sheet turbidite sands (the I10 and the J1-J4) that are collectively known as the J-sands. The J-sands are early Nebraskan (3.35 Ma) in age and presently lie 3300 – 4000 m below sea level. They are composed of unconsolidated, well-sorted, fine-to-very-fine grained sands, with a generally coarsening upwards grain size distribution (Holman and Robertson, 1994). The sands are interbedded with debris flow deposits and shales (Flemings et al., 2001). The J-sands have excellent porosity (30-34 %) and

permeability (0.5-2 Darcy) (O'Connell, 1993). The pressure communication between the sands and their high compressibility means that all the J-sand reservoirs have a strong water/compaction drive mechanism (Holman and Robertson, 1994).

As is frequently observed in the Gulf of Mexico, the J-sand hydrocarbon reservoirs have lower density and velocity than the bounding shales. The impedance contrast is particularly strong at Bullwinkle because the undersaturated oil hydrocarbon column has a high gas-oil ratio (GOR) (500-1300 SCF/STB). The aquifer regions of the sands are brine saturated and have a small impedance contrast with their adjacent shales. This affords easy identification of hydrocarbon-water contacts (O'Connell, 1993), and also makes events such as the Bullwinkle J-sands ideal locations for observing oil-water movement using time-lapse seismic analysis (Lumley, 2001).

This study concentrates on the J2 sand, which is the major hydrocarbon producer at Bullwinkle, with over 50% of the total reserves. It is laterally extensive in the northern and western section of the minibasin and is typically 10-30 m thick. Dips are steepest against the western salt flank and exceed 20° in the southern region of the reservoir (Figure 3). It appears that the J2 sand extends across the southern extremity of the basin, which may provide a channel for water influx. The 1988 pre-production surveys exhibit a clear seismic OOWC at 3785 m (Figure 3). Production data and pulsed neutron capture (PNC) logs show that this moved up to around 3535 m in 1997 in the main section of the J2 reservoir.

Early J2 deposition is dominated by laterally extensive sheet lobes with local interbedded debris flows (Holman and Robertson, 1994). They have high net-to-gross sand ratios and blocky gamma ray log signatures. Later J2 deposition is more

channelized. The upper J2 sand in the western portion of the basin consists of an elongate region of fine-grained channel fill and thin-bedded shale prone channel overbank deposits.

### **3-D Seismic Surveys**

Three 3-D seismic surveys are considered in this study (Figure 2). Two were acquired just prior to the onset of production in 1988. They were shot orthogonally with the intention of investigating the effect of shooting direction in the presence of complex salt geometry (O'Connell, 1993). One is orientated at 020-200° and is referred to here as the 1988 N-S LF survey (Table 2). The second, the 1988 E-W HF survey (Table 2), has an inline direction of 110-290°. The third survey, the 1997 survey (Table 2) is a regional non-proprietary survey acquired in a due north-south orientation in 1997, after over eight years of production from the field.

A prestack trace-by-trace running summation (numerical integration (Deshpande et al., 1997)), was performed on the 1988 surveys during original processing (Table 3). The 1988 surveys were later reprocessed and poststack spectral equalization was performed. These versions of the surveys are known as the “whitened” 1988 surveys. We consider both the whitened (1988 N-S HF) and non-whitened (1988 N-S LF) surveys, and solely the whitened (1988 E-W HF) survey (Table 2).

None of the surveys were acquired for time-lapse purposes and they have considerable differences in acquisition and processing (Table 3). This dictates that they must be normalized before they can be compared directly (Ross et al., 1996). Although the maximum offset in the 1997 survey is nearly double that of the 1988 surveys (6010 m

versus 3930 m, Table 3), the offset weighting and mute applied to the datasets means that approximately the range of offsets are present at the J-sand level in all the surveys (Appendix B). Since we have pre-production surveys with different orientations and bandwidths, we can investigate the effect of acquisition direction and frequency content on time-lapse repeatability, and examine the drainage history of the Bullwinkle hydrocarbon reservoirs.

## **NORMALIZATION METHODOLOGY**

We perform poststack normalizations upon the Bullwinkle seismic surveys in order to maximize the similarity between the surveys in regions unaffected by production. In each case, we alter the 1997 survey to match the 1988 surveys. The normalization methodology is similar to that of Burkhart et al. (2000), and also Johnston et al. (2000), except that Johnston et al.'s (2000) final step of time alignment and residual migration is not performed.

We consider a sub-volume from each of the surveys that includes the main J-sand reservoirs (the 4-D Volume, Table 2). Normalization parameters are calculated from a region within the 4-D Volume (the Aquifer Volume, Table 2) in which we assume that production effects are minimal. These parameters are then applied to the entire normalization volumes, so that real differences due to production are not falsely reduced.

Separate normalizations are performed for three pairs of seismic volumes: the 1988 E-W HF survey and the 1997 survey; the 1988 N-S HF survey and the 1997 survey; and the 1988 N-S LF survey with the 1997 survey. These will be referred to subsequently as the E-W HF (east-west, high frequency) normalization, the N-S HF

(north-south, high frequency) normalization and the N-S LF (north-south, low frequency) normalization, respectively (Table 2).

### ***Rebinning***

One of the surveys is rebinned so that they have identical orientation, trace locations, and bin sizes. In all normalizations, the more closely spaced 1997 survey traces were rebinned in order to match the trace locations of the 1988 surveys. This was done to ensure that spatial aliasing did not occur (Berni et al, 1997). Rebinning was implemented using a weighted linear interpolation (Burkhart et al., 2000).

### ***Global Shifting***

The next process in the normalization is to apply a bulk shift of the datasets in the x, y, and time directions. The optimal shift is determined by cross-correlating the 1988 data with the 1997 data in order to find the position in which the datasets have greatest similarity. The 1997 data were shifted in a similar manner in each of the normalizations, with the largest shift being necessary in the time (vertical) direction, of 20 to 28 ms upwards (Table 4). Eastwards shifts of 15 m in the E-W normalization, and of 46 m in the N-S normalizations were also required. These horizontal shifts may have resulted from different imaging of dipping events or navigational errors. In general, the bulk shifts correct for differences in the data due to navigational errors, static time differences and processing differences.

## ***Frequency Filtering***

Identical high-cut filters were applied to both data volumes in each normalization (Table 4). The high-cut frequency was chosen to represent the frequency limit of significant power in the lower frequency volumes. After high-cut filtering, the 1988 surveys are referred to as the 1988 E-W HF' survey, the 1988 N-S HF' survey, and the 1988 N-S LF survey (Table 2).

## ***Wiener Filtering***

A cross-equalization or Wiener matching filter (Robinson and Treitel, 1967) is used to reshape the 1997 data so that it is more similar to the 1988 data. We use the matching filter as a transfer function to apply to the reflection coefficient (RFC) 1997 data in order to modify it to resemble the integrated 1988 data. Since the whitened 1988 surveys contain higher frequencies than the 1997 data, the matching filter also acts as a spectral whitening filter in the E-W HF and N-S HF normalizations (Figure 5). This is not the case in the N-S LF normalization, in which the cross-equalization filter reduces frequency content of the 1997 data. The Wiener filters do not time-shift the 1997 data (Figure 6).

A Wiener filter is calculated in the time domain for each corresponding pair of traces in the Aquifer Volume. The filter minimizes the energy of the differences between the traces in a least-squares sense (Robinson and Treitel, 1967) and assumes the data to be stationary. A preliminary amplitude balance is performed prior to Wiener filtering so that the match filter can have the greatest effect in equalizing the phase and time-

alignment of the embedded wavelets. The filter coefficients are then averaged to derive a single filter to apply to the whole 4-D Volume. The Aquifer Volume was chosen to be in a shallowly dipping section of the aquifer (Figure 3), which reduces the need for the filter time-alignment procedure applied by Johnston et al. (2000). The cross-equalized 1997 surveys are referred to as the 1997a' survey (reshaped to match the 1988 E-W HF' survey), the 1997b' survey (reshaped to match the 1988 N-S HF' survey), and the 1997c' survey (reshaped to match the 1988 N-S LF survey) (Table 2).

### ***Amplitude Scaling***

The final step is to statistically balance the amplitudes of the surveys. Amplitude scaling is accomplished using the following equation, which utilizes the mean ( $\bar{y}$ ) and standard deviation ( $s_y$ ) of the Aquifer Volume of dataset  $y$ :

$$\hat{y}_i = \frac{10}{s_y}(y_i - \bar{y}) \quad (1)$$

Only the Aquifer Volumes of the seismic cubes are used to calculate the scaling parameters because real amplitude changes in the reservoir can have a noticeable affect on the seismic data. The result is a normalized seismic volume ( $\hat{y}$ ) whose Aquifer Volume has a standard deviation of ten and mean of zero. The amplitudes of the different normalized surveys can now be directly compared. The means and standard deviations of the Aquifer Volumes in each of the normalizations before and after amplitude scaling are listed in Table 5.



## STATISTICAL ANALYSIS

### *Quantifying Repeatability*

We use the differences in three separate regions to quantify the similarity of the normalized surveys, and hence the repeatability achieved by each normalization. Any differences between the normalized seismic datasets in regions that should remain unchanged between the acquisition of the 1988 and 1997 surveys can be considered to be noise, or error in the data. Error can arise from differences in the acquisition and processing of the surveys and the presence of ambient noise during acquisition (Stephen, 2000). We consider the Aquifer Volume, the J2 Aquifer Horizon, and the G2 Horizon (Table 2). The G2 is a volcanic ash event located approximately 300 ms above the J2 sand, and should be unaffected by hydrocarbon production.

**Correlation.-** The correlation coefficient between two datasets, a measure of their similarity, can be defined as

$$r = \frac{\mathbf{s}_{xy}}{\mathbf{s}_x \mathbf{s}_y} \quad (2)$$

where  $\mathbf{s}_{xy}$  is the covariance of datasets  $x$  and  $y$ . We use correlation in the Aquifer Volume to quantify the success of each normalization step. We also use equation (2) to determine correlation at the horizon level. When  $r = 1$ , the data are perfectly correlated and all points on a cross-plot of amplitudes from the 1988 and 1997 surveys lie on a straight line. When  $r < 1$ , the data are not perfectly correlated. This is a result of changes in rock and fluid properties, or error in the data ( $u$  and  $v$ ).

**Regression Model.-** We assume that the normalized 1988 ( $\hat{x}$ ) and 1997 ( $\hat{y}$ ) seismic data are composed of earth properties ( $\mathbf{x}$  and  $\mathbf{h}$ ) and random error ( $u$  and  $v$ ) (Burkhart et al., 2000). The earth properties are assumed to be perfectly correlated, with means  $\bar{\mathbf{x}} = 0$  and  $\bar{\mathbf{h}} = 0$  and standard deviations  $\mathbf{s}_x$  and  $\mathbf{s}_h$ . The error terms are uncorrelated with means  $\bar{u} = 0$  and  $\bar{v} = 0$ , and standard deviations  $\mathbf{s}_u$  and  $\mathbf{s}_v$ . Therefore,

$$\mathbf{s}_x = \mathbf{s}_x + \mathbf{s}_u \quad (3a)$$

and

$$\mathbf{s}_y = \mathbf{s}_h + \mathbf{s}_v \quad (3b)$$

Furthermore, we assume that the signal to noise ratio (SNR) of the surveys is the same. It then follows that  $\mathbf{s}_u = \mathbf{s}_v$  after normalization. The implications of variable S/N ratios are discussed by Burkhart et al. (2000) and by Rickett and Lumley (2001).

The geometric mean regression line (GMRL) for each normalized Aquifer Volume cross-plot (Figure 8) minimizes the sum of the products of the absolute vertical and horizontal deviations from the regression line (Ricker, 1973). The GMRL is generated using the following equation:

$$y_i = b_0 + b_1 x_i \quad (4)$$

where  $b_1 = \mathbf{s}_x/\mathbf{s}_y$  and  $b_0 = \hat{y} - b_1 \bar{x}$ . The parameters  $\bar{x}$  and  $\bar{y}$  are the means of normalized seismic datasets  $x$  and  $\hat{y}$ . Consequently, the Aquifer Volume regression lines have a slope of one and an intercept of zero.

The scatter of the data perpendicular to the GMRL ( $p$ ) is an important parameter in determining the similarity of the two datasets. We expect  $p$  to be normally distributed

with mean  $\bar{p} = 0$  and standard deviation  $\mathbf{s}_p$ . If  $b_0 = 0$  and  $b_1 = 1$ , then its variance ( $\mathbf{s}_p^2$ ) is equal to the variance of the difference between the seismic volumes ( $\mathbf{s}_{diff}^2$ ). Additionally,  $\mathbf{s}_p^2$  is equal to twice the error variance (Burkhart et al., 2000):

$$\mathbf{s}_p^2 = \mathbf{s}_u^2 + \mathbf{s}_v^2 = 2\mathbf{s}_u^2 \quad (5)$$

**RMS Ratio.-** The RMS ratio ( $RR$ ) (equation (A-1)) is a commonly used measure of repeatability in time-lapse data (Kragh and Christie, 2001). In the Appendix, we show that the correlation coefficient of normalized seismic data with equal SNR is related to the RMS ratio through the following equation:

$$r = 1 - \frac{1}{2}RR^2 \quad (6)$$

We also demonstrate that the relation between  $r$  and  $\mathbf{s}_p$  is

$$r = \frac{\mathbf{s}_x^2 - \frac{1}{2}\mathbf{s}_p^2}{\mathbf{s}_x^2}. \quad (7)$$

**Prediction Bands.-** We use the deviations from the GM regression line to determine the noise level in the normalizations, and to discriminate changes that have a higher probability of representing true changes in rock and fluid properties. This is done through the calculation of prediction bands (Burkhart et al., 2000). The 95 % prediction bands contain 95 % of the data and there is consequently a 95 % probability that a data point in the Aquifer Volume will lie within them. We assume that real differences that lie within the 90 % prediction bands cannot be distinguished from noise and color them gray on subsequent difference maps. The width of the prediction bands is dependent on  $\mathbf{s}_p$  and describes the amount the noise or error present in the data after normalization.

## RESULTS

### *Aquifer Volume Statistics*

Correlation increases with every step in all the normalizations (Figure 7). In all cases, the 1988 and 1997 volumes are uncorrelated after rebinning. This is because they are misplaced by approximately 25 ms two-way travel time (TWT) (Table 4), causing events to be improperly aligned. The global shifting operation accounts for most of this error, giving a large increase in correlation at all depths (Figure 7). High-cut filtering produces a very small, or negligible increase in similarity. Cross-equalization filtering increases correlation by approximately 10 % over the frequency-filtered volumes. The N-S LF normalization produces the highest overall correlation and the E-W normalization gives the lowest correlation (Table 5).

Correlation is generally greatest in all cases around 3300 ms and 3800 ms (Figure 7). These depths correspond to the G2 horizon and a combination of the J-sands and the top-salt event, respectively. We interpret that the higher correlation reflects the fact that the noise is constant, whilst the signal is large where large amplitudes are present.

The normalized Aquifer Volume cross-plots of 1997 versus 1988 data exhibit significant scatter above and below their respective GMR lines (Figure 8). Greater scatter results in a larger  $\mathbf{s}_p$  and therefore reduced correlation (equation (7)). The greatest scatter is evident in the E-W HF normalization ( $\mathbf{s}_p = 7.64$ ), and least in the N-S LF normalization ( $\mathbf{s}_p = 6.60$ ) (Table 7). This demonstrates that the 1988 and 1997 Aquifer Volumes are least similar in the E-W HF normalization and most similar in the N-S LF normalization. Consequently, the prediction bands are widest in the E-W HF

normalization, narrowest in the in the N-S LF normalization and have intermediate width in the N-S HF normalization.

### ***Horizon Statistics***

A cross-plot of amplitudes from the normalized 1988 and 1997 data from the N-S LF normalization extracted from a 40 ms window centered on the G2 event shows that the G2 amplitudes follow the trend of the N-S LF Aquifer Volume very closely (Figure 9). The GMRL calculated for the G2 Horizon is extremely similar to that calculated for the N-S LF Aquifer Volume. This supports the interpretation that the G2 did not change with time.

The G2 ash event has less scatter than the Aquifer Volume as a whole (Figure 9a versus Figure 8a). For example, in the best case (the N-S LF normalization),  $s_p = 5.37$  and the correlation is correspondingly high ( $r = 0.831$ ) (Table 7). We surmise that the lesser scatter in the G2 event is a result of an improved SNR in this shallower portion of the seismic volumes. We also observe similar results for the G2 event in the high frequency normalizations, in which it also exhibits the highest correlation and least amplitude difference variance (Table 7).

The J2 Aquifer Horizon shows much less scatter than the J2 Reservoir Horizon (Figure 9b versus Figure 9c). This is expected because the aquifer pore-fluid is not changing, whereas in the reservoir, water is replacing oil. However, it is interesting that the slope of the GMRL is flatter for the J2 Aquifer Horizon than for the Aquifer Volume (Figure 9b). This means that the J2 Aquifer Horizon has dimmed over calendar time. We attribute the J2 Aquifer dimming to compaction in response to a decrease in pore-

pressure. Landrø (2001) shows that this can give rise to a significant increase in acoustic impedance over time and hence reduce the impedance contrast of the sand with its adjacent shales. Other workers have modeled this compaction affect (e.g. Batzle & Wang, 1992; Landrø, 2001), but it has rarely been observed in practice.

In general, the absolute values of the 1997 amplitudes are less than those of the 1988 amplitudes in the J2 Reservoir Horizon, with many lying outside the 99.99 % prediction bands. These changes individually have less than a one in ten thousand probability of being due to noise or error. The N-S LF J2 reservoir GMRL has a slope of 0.71 indicating that very significant dimming has occurred in this horizon. The J2 Reservoir Horizon amplitude extractions also exhibit a substantial reduction of mean amplitude (−50.05 to −21.79 in the N-S LF normalization) (Table 6).

## ***Differencing***

Normalized 1997 amplitudes are subtracted from the normalized 1988 amplitudes to illustrate the change in seismic response over calendar time. Difference cubes were produced for the three normalizations. However, these are of limited value because differences are present that are a result of misalignment of seismic reflectors between the surveys. The travel-time differences range up to 60 ms for the J2 event after normalization (Figure 10). Johnston et al. (2000) attribute similar travel-time differences in the Lena (Offshore Gulf of Mexico) seismic surveys to different migration velocities and algorithms used in the original processing of the data. This is confirmed by the fact that the differences are greatest where the dips are steepest (Figure 10). Leggott et al. (2000) showed that the travel-time differences much smaller than this magnitude can

produce substantial differencing errors. Gently dipping regions exhibit very minor or nonexistent misalignment. We combat these travel-time differences by interpreting events separately in the normalized data and then differencing the resulting amplitude extractions. This procedure is less sensitive to event positioning errors in the normalized surveys.

The J2 difference maps (Figures 11-13) provide a spatial picture of how the amplitudes in the J2 horizon have changed over time. They are closely related to the horizon cross-plots (Figure 9), which show the change in amplitude in a window around the horizon. In the maps, the difference between the normalized 1988 and 1997 amplitudes (or the distance that the amplitudes plot from the GMRL) is represented by a color scale. Blue colors correspond to points where troughs have decreased in absolute amplitude over time (dimming), or where seismic peaks have increased in amplitude over time. Warm colors represent regions where negative troughs have increased in absolute amplitude (brightening), or where peaks have weakened.

We then use the prediction bands derived from the whole Aquifer Volumes to describe the magnitude of the observed differences in J2 horizon in their corresponding normalizations (Figures 14 and 16). In these prediction band maps, the prediction bands define the difference color scale. Amplitudes that plot within the 90 % prediction bands are shaded gray.

## ***J2 Differences***

The J2 difference maps from all three normalizations exhibit significant dimming in the structurally lower two thirds of the reservoir (Figures 11d, 12d, 13d, 14 and 16).

The E-W HF normalization difference map contains many regions of very strong dimming within the reservoir, but also areas that show no significant change (Figure 11d). The N-S HF normalization dims more patchily and less significantly (Figure 12d), whilst the N-S LF normalization shows the most pervasive amplitude reduction (Figure 13d). The dimming tends to be strongest in all three normalizations in the main section of the reservoir, where the original amplitudes were greatest (Figures 11c, 12c, and 13c).

We estimate the oil-water-contact (OWC) at the time of the later survey from well log (PNC) and production data. The difference maps show that it correlates well with the updip limit of dimming, particularly in the N-S normalizations (Figures 12d, 13d, 14b and 16). The zone of dimming in the E-W HF normalization often extends beyond the 1997 OWC in the order of 100 m horizontal distance (Figures 11d and 14a). This is most noticeable in the southern portion of the reservoir. The downdip limit follows the seismic original oil-water-contact (OOWC) within the oil-water contact feather in all cases (Figures 11-14 and 16).

We observe less significant change in the northeastern region of the reservoir. Regions of dimming do exist and appear to be separated to some extent by the seismic discontinuities present in the reservoir (Figures 11d-13d, 14, 15 and 16). The differences in the updip reservoir above the 1997 OWC tend to be small and more random in nature. All the normalizations show evidence of small regions of brightening in the shallowest portions of the main J2 reservoir. The region around well 108-2 above this appears to dim in the N-S normalizations (Figures 12d, 13d, 14b and 16) and shows variable character in the E-W HF normalization (Figures 11d and 14a).



As anticipated, little significant change is imaged in the aquifer regions, although an area of substantial brightening is apparent in the all the difference maps (Figures 11d-13d, 14, and 15). This occurs in the southwestern region of the aquifer where the J2 sand merges with the GC 110 “Rocky event” (Kinaki and Smith, 1996). Elsewhere, the J2 aquifer generally dims more often than it brightens, most noticeably in the N-S HF normalization (Figures 12d and 14b). Aquifer dimming is further illuminated by an enlarged region of the 1988 N-S LF J2 aquifer with an expanded color scale (Figure 16).

## **INTERPRETATION**

### ***Influence of Orientation and Bandwidth***

***Orientation.-*** The E-W HF normalization produces less similar traces in the Aquifer Volume than the N-S HF normalization, despite the application of an identical normalization procedure. This is evident from the E-W HF normalization’s lower Aquifer Volume correlation (Figure 7), wider prediction bands (Table 8), and greater variance in the difference volume (Table 7). Although these results are dependent upon one another, the greater similarity of the N-S HF normalization is significant. For example, its overall Aquifer Volume correlation coefficient is 0.700, compared to the value of 0.591 for the E-W HF survey (Table 7). Furthermore, the similarity between the N-S HF traces is substantially greater in both the J2 Aquifer (0.698 vs. 0.597) and G2 Horizons (0.810 vs. 0.780) (Table 7). This result is not surprising because the acquisition direction of the E-W 1988 survey is 70° different to the 1997 survey, whilst the orientation of the N-S 1988 survey is only 20° apart from the 1997 survey (Table 3).

The prediction band difference maps from the high frequency normalizations (Figure 14) show that the E-W normalization images a greater area of apparently significant drainage. This is most evident in the northern section of the main J2 reservoir, and also around the 1997 OWC. However, a close inspection of the E-W HF normalization difference and original amplitude maps (Figure 11c and 11d) reveal that the areas of strong dimming in the E-W HF normalization correspond almost exactly to where the 1988 amplitude is greatest, suggesting that the 1988 E-W HF' amplitudes are systematically higher than the 1997a' amplitudes.

O'Connell et al. (1993) state that the shooting direction of a survey can effect the stratigraphic resolution of sediments in the presence of the complex salt geometry and steep dips that are found at Bullwinkle. In the J2 reservoir, the finer dip sampling of the 1988 E-W HF survey provides a definite improvement in illumination over the 1988 N-S HF survey, since the Jsand package is disrupted by stair-step noises and migration "rooster tails" in the north-south survey (O'Connell et al., 1993). The 1988 N-S HF survey also suffers from acoustic energy being scattered out of the plane of the receivers, since it was acquired perpendicularly to the dip of the main J-sand reservoir region.

These factors cause the SNR to vary in different regions of the 1988 N-S HF survey, and in a different way to the 1988 E-W survey. This has a significant impact on the amplitudes distributions of the two surveys (Figure 15). We assume that the noise variance in the 1988 surveys ( $\mathbf{s}_x^2$ ) is smaller than the signal variance ( $\mathbf{s}_u^2$ ). In the shallowly dipping Aquifer Volume, events are imaged similarly. The 1988 surveys consequently have similar S/N ratios and their amplitude histograms match closely (Figure 15a). However, in the dipping reservoir region, greater signal is recorded in the

1988 E-W HF survey. Additionally, more noise may be present in the 1988 N-S survey due to amplitude scaling during processing, and from migration and stair-step noises. Therefore, the total seismic record has greater variance in the 1988 E-W HF survey than the 1988 N-S HF survey in the J-sand reservoirs (Figure 15b).

This is supported by the mean and variance of the J2 reservoir amplitude extractions (Table 6). The J2 reservoir event has mean maximum trough amplitude of  $-48.94$  and standard deviation of  $22.57$  in the normalized E-W 1988 survey, but only a mean of  $-27.51$  and standard deviation of  $17.04$  in the N-S 1988 survey (Table 6). Since the variance of the identical Aquifer Volumes is identical, this shows that the J2 event is more strongly imaged in the E-W 1988 survey.

We also notice that the 1997 survey J2 reservoir mean amplitudes are lower ( $-21.22$  versus  $-15.97$ ) in the N-S HF normalization compared to the E-W HF normalization (Table 6). This suggests that the embedded wavelet in the N-S HF normalization does not strongly image the J2 event, in response to the sand thickness and interference with adjacent events.

Stronger stratigraphic imaging in the 1988 E-W HF survey relative to the 1988 N-S HF survey may explain why the zone of dimming in the E-W HF normalization extends above the 1997 OWC. This is because the 1988 E-W HF survey will image the J2 sand more clearly than the north-south 1997 survey, even where the J2 event is hydrocarbon-filled in the later survey. Additionally, the observed dimming above the 1997 OWC may be a result of lateral mispositioning of the J2 event between the E-W 1988 and 1997 surveys due to different migration and DMO velocities and algorithms (Table 3). Consequently, although the N-S HF difference map is less striking than the E-W HF

difference map, the differences that do exist are more likely to represent real rock and fluid changes in the reservoir, rather than being artifacts of different acquisitional parameters.

**Bandwidth.-** Our measures of repeatability demonstrate that the N-S LF normalization provides a more dependable time-lapse difference result than the N-S HF normalization. It has slightly greater correlation at all depths (Figure 7), with the total Aquifer Volume correlation coefficient being 0.70 compared to the correlation of 0.68 observed in the normalized higher frequency data. This is supported by the N-S LF normalized data having narrower prediction bands and a correspondingly smaller standard deviation in the Aquifer difference volume ( $s_p = 6.60$  in the N-S LF normalization, whereas  $s_p = 6.89$  in the N-S HF normalization) (Table 7).

The N-S LF normalization illuminates much more widespread and significant J2 differences (Figures 14b and 16). Again, a nearly identical normalization procedure was followed in both cases. The only difference is that the cross-normalization filter was used in the high frequency normalization to increase the spectral bandwidth of the 1997 survey by shaping it to match the whitened 1988 survey (Figures 5c and 5d). The Wiener filter reduced the bandwidth of the 1997 data in the N-S LF normalization to match that of the non-whitened 1988 survey (Figures 5e and 5f).

The lesser similarity between high frequency normalized surveys is likely to have arisen from two mechanisms. Firstly, spectral whitening increases the power of higher frequencies in the data. Although the process was constructed to minimize the amplification of noise, it is inevitable that some noise will be increased in power (Davies

and Warner, 1999). This will occur in both the original spectral balancing applied to the 1988 data, and also by the cross-equalization filter convolved with the 1997 survey traces during normalization. The data volumes will therefore have decreased S/N ratios and will consequently be more dissimilar. We determine the signal to noise ratio of the normalized data through the following equation (after Burkhart et al., 2000):

$$SNR = \frac{\mathbf{s}_x}{\mathbf{s}_u} = \frac{\mathbf{s}_x}{\sqrt{\mathbf{s}_p^2/2}} \quad (6)$$

The N-S HF normalization has a lower S/N ratio of 1.794 compared to 1.900 than the N-S LF normalization (Table 5).

The second reason for decreased similarity in the whitened data stems from the fundamental observation that small misalignments are more significant in high frequency wavelets. We demonstrate this by considering the correlation between two Ricker wavelets (Sheriff and Geldart, 1995) separated by a time shift of 4 ms (equal to one sample in the seismic data). At very low frequencies, this time shift is almost negligible and the correlation between the wavelets is very high (Figure 21). However, at high frequencies, the time shift is much more significant since the wavelength is shorter. Therefore, if the same time misalignment errors are present in the higher frequency data, we expect to find that they do not match each other as closely. This also has the affect of decreasing our measure of SNR. Additionally, interpretational errors are more important in the high frequency data and may obscure a substantial portion of the J2 amplitude changes over time.

The N-S LF difference map shows markedly more widespread significant dimming within water swept region of the J2 reservoir than the N-S HF normalization

(Figure 16). The improvement in dimming imaging is surprisingly large, given the relative closeness in correlation between the two N-S normalizations. It is likely that it is exaggerated by the combination of lower SNR and greater influence of interpretational errors in the higher frequency data. Additionally, the 1988 N-S HF data suffers from more pronounced dip-related imaging distortions in the reservoir, which are not picked up by observing correlation in the downdip aquifer.

## ***J2 Drainage***

We use the N-S LF normalization J2 difference map (Figure 16) to characterize the drainage of the main J2 reservoir. We also use Gassmann fluid substitution to support the observed differences by comparing them to predictions for one well that has been water swept (well 109-1), and a well above the estimated 1997 OWC (well A-33). The more complex northwestern section of the reservoir, with several pressure and flow barriers (obstructions in the sand that fluids cannot flow across over production time-scales), and different fluid compositions, is not discussed here

We observe even drainage of the J2 sand in response to a strong water drive mechanism through a study of the PNC and production data for the J2 event. This is compatible with the high porosity and permeability of the J2 sand, combined with its good lateral and vertical continuity (Holman and Robertson, 1994). Based on the log and production data, we interpret that the OWC lay at a sub sea depth of approximately 3540 m throughout most of the J2 reservoir during the acquisition of the 1997 survey, only deepening at the northern margin of the sand where water sweep has tended to lag behind the reservoir center. The non-horizontal oil-water contact at the northern sand fringe is a

consequence of hydrocarbons being bypassed due to strong production from the center of the reservoir, and has been verified by production data and reservoir simulation studies.

The N-S LF difference map (Figure 16) shows excellent agreement with the independently derived 1997 OWC prediction. The zone of water sweep corresponds to a broad region of consistent dimming. Well 109-1 is situated in the water-swept section of the reservoir. The oil-water contact moved upwards past the well three years before the 1997 survey was acquired, which is clearly demonstrated by the production history of nearby well A-32-BP (Figure 17b). Figure 17a shows traces extracted at the 109-1 location from both the normalized 1988 and 1997 surveys in the N-S LF normalization. Also shown is the difference between them, which reaches a maximum of 71 % of the original normalized 1988 amplitude in the J2 event.

We use the Gassmann equations (Gassmann, 1951) to model how compaction, porosity and fluid saturation changes affect the acoustic impedance of the J2 sand in well 109-1. The elastic constants used in the Gassmann equations are calibrated in the water-saturated J3 sand and then applied to the oil-saturated J2. The effect that water sweep and pressure decline has on the sonic velocity of the J2 is investigated by compacting the sand, draining the rock to an irreducible water saturation of 20 % and then re-applying the Gassmann equations. This rock-physics approach confirms that a predicted increase in acoustic impedance by 20% can cause the seismic amplitudes to dim by up to 70%.

Areas of no discernable amplitude change over time, interspersed with small discontinuous patches of brightening and dimming characterize the region above the 1997 OWC. This is consistent with this area being oil saturated during the acquisition of both the 1988 and 1997 surveys. The brightening may be a consequence of free-gas

exsolving from the hydrocarbon column as the reservoir pressure in the uppermost regions falls below its bubble point. The production history of well A-33 (Figure 18b) shows the recorded reservoir pressure dropping below the predicted original bubble point pressure in 1992. Gas production rises rapidly at this point, which can decrease the rock's impedance (Lumley, 2001). The difference between extracted traces from the A-33 location in the N-S LF normalization (Figure 18a) shows a small degree of brightening over time, which is consistent with the application of our Gassmann modeling procedure to well A-33.

The region of dimming appears to terminate to the south against a small fault that does not displace the J2 horizon in the seismic surveys (Figure 16). It does, however, offset the J4 event 100 m below, and its path can be traced by a reduction in horizon amplitude. The large amplitudes in the original amplitude maps die out against this fault, suggesting that it is sealing. It is possible that this feature defines the edge of the J2 reservoir, and not the larger fault further to the south.

The shallowest section of the J2 sand in block 108 (Figure 16) tends to decrease in amplitude between 1988 and 1997, despite the fact that no production has occurred from this area. Pressure measurements and the presence of a perched oil-water contact confirm that this updip region is not in communication with the rest of the J2 sand. An observable seismic discontinuity can often be seen to separate this section of the J2 event, particularly in the higher frequency datasets (Figure 19). The observed dimming may arise from imaging differences due to the close proximity of a salt body, since the event is stronger in the N-S 1988 surveys than either the E-W 1988 survey or the 1997 survey. Other possible causes for amplitude reduction include interference from changes in the



overlying J1 reservoir, and extensive well testing in the exploration wells that penetrated this compartment.

## DISCUSSION

We have presented a methodology to perform a relatively fast and inexpensive normalization of legacy seismic data. We then statistically evaluate the repeatability achieved by the normalization and qualitatively describe the differences observed in a producing hydrocarbon reservoir. The application of this procedure to the unique collection of 3-D seismic surveys acquired over the Bullwinkle has enabled us to evaluate the drainage pattern of the field's major hydrocarbon reservoir. Furthermore, we can separately determine the influence of both survey orientation and spectral whitening upon time-lapse repeatability.

We have shown that we can use existing seismic data and a poststack normalization procedure to successfully image water sweep in the J2 reservoir. A broad region of uniform dimming corresponds very well to where production and well data show that water has evenly replaced oil in the reservoir. This contrasts with the K40 horizon at ST 295, where Hoover et al. (1999) find that poor drainage of low permeability lithofacies results in a lack of seismic dimming in some parts of the reservoir. Seismic dimming is expected because the replacement of oil by water in the reservoir increases the sonic velocity of the rock and hence its acoustic impedance (Landrø, 2001). This has the effect of reducing the impedance contrast with the sand's adjacent shale interfaces and decreasing the amplitude of the J2 event.

The even sweep of the reservoir observed in this study suggests that the J2 reservoir may have been produced equally effectively using fewer production wells, and that the water injection wells may have been unnecessary. These are complex issues that require extensive reservoir simulation to answer quantitatively. This study has shown that there are few areas of bypassed hydrocarbons within the reservoir, indicating that secondary recovery techniques are likely to be uneconomic at Bullwinkle. However, we have highlighted a region in southern portion of the reservoir, whose amplitudes have not changed significantly over time. Further evaluation may be worthwhile in order to determine whether this region contains trapped hydrocarbons, or was initially water saturated.

We also observe a small degree of amplitude reduction in the J2 Aquifer Horizon in all three normalizations. The change in aquifer amplitudes over time produces greater scatter in the Aquifer Horizon cross-plots (Figure 9) and reduced correlation between the 1988 and 1997 data (Figure 7). More importantly, it has significant implications for amplitude scaling. If the aquifer regions of producing horizons compact (and reduce in amplitude) over time, the Aquifer Volume will dim as a whole. Therefore, when we force the Aquifer Volume amplitudes in the 1988 and 1997 data to match, we will falsely increase the amplitudes of the monitor survey. As a consequence, more dimming may be occurring in the 1997 data than we observe with our amplitude scaling approach.

Since the G2 event is a volcanic ash and has not experienced production, we expect it to have compacted little in response to production from the field. As a result, it should appear to brighten in the 1997 survey if the Aquifer Volume amplitudes are systematically being reduced by compaction. However, the G2 cross-plot (Figure 9a)

shows that the G2 Horizon amplitudes are essentially unchanged in the normalized 1988 and 1997 surveys. This is supported by the closeness of the extracted G2 amplitudes from the normalized surveys (Table 6). We conclude that the amplitude change in the J2 aquifer is minor in relation to the total amplitudes of the whole Aquifer Volume, so its affect is minimal.

We found that steeply dipping events in the 1988 and 1997 surveys were not exactly aligned, even after normalization. This is likely to be predominantly a result of different DMO velocities and algorithms being used in the original processing of the surveys, as Johnson et al. (2000) found in their time-lapse analysis at Lena. This event misalignment precludes the use of difference volumes and cross-sections, and necessitates our horizon differencing approach.

Although the favorable rock properties at Bullwinkle allow our approach to be more than adequate for us to gain a useful time-lapse result in this situation, it is possible that further steps may need to be taken in order to successfully image fluid movement at other fields. Other researchers have presented methods to reduce these residual event misalignments. A common procedure is to apply trace-by-trace static time corrections, which is effectively equivalent to our horizon differencing approach. However, as Rickett and Lumley (2001) point out, static corrections do not account for spatial mispositioning due to different event dip angles, and do not allow for time-shifts that vary as a function of travel time. A better procedure would be to apply a dynamically varying shift procedure, such as Leggott et al.'s (2000) rotation, Johnston et al.'s (2000) residual migration, or Rickett and Lumley's (2001) warping.

Another methodology would be to reprocess the 1988 and 1997 data in a consistent manner, using similar velocity fields (Harris and Henry, 1988; Johnston et al., 2000). Reprocessing the Bullwinkle seismic surveys before normalization should give greater similarity in the Aquifer Volume, particularly because there would be no need to attempt to account for the integration and whitening procedures performed on the original data. This may result in greater confidence being placed in the observed variations of dimming within the J2 reservoir, and possibly enable the identification of bypassed pay in the field.

Our time-lapse repeatability results are comparable to those found by other workers (Table 9), despite the fact that our streamer data were not acquired for time-lapse purposes and have markedly different original acquisition and processing parameters. We compare correlation coefficient results to RMS ratios through equation (6), which is valid when comparing normalized seismic data with zero mean and equal amplitude and noise variance. We find that poststack normalizations that do not involve reprocessing of the seismic data produced normalized seismic volumes that are less similar than those datasets that have been reprocessed in parallel. Greater repeatability is achieved by using purposely-acquired surveys, particularly ones that were recorded with ocean bottom cables.

We have shown that it is advantageous to use the N-S 1988 data as the baseline survey for our time-lapse analysis, despite the fact that the 1988 E-W HF survey provides the best original imaging of the J-sand reservoirs. This is because the 1988 N-S surveys were acquired in a direction closer to that of the 1997 survey, and therefore image the J2 event more similarly. We have also shown that the EW normalization did appear to

produce a reasonable successful result, but the disparity between the time-lapse 1997 OWC and that predicted by PNC log and production data calls this into question. The reduced similarity between the EW HF normalization surveys may also mean that is impossible to image fluid movements in other fields with less favorable rock properties by comparing surveys with markedly different orientations.

The benefit of spectral whitening in the normalization process is more difficult to assess. Although we have demonstrated that the higher frequency N-S normalization is noisier and more variable than the low frequency version, it does have the advantage of improved stratigraphic resolution. This is particularly important for the Bullwinkle J-sands, where the sands are frequently below tuning thickness and interfere with each other. All of these sands are significant hydrocarbon reservoirs and it could be desirable to gain a time-lapse image of their drainage from a production point of view. We investigate this by considering the J1 event, which lies very closely above the J2 horizon and originally contained approximately 35 MMBBL ( $35 \times 10^6$  Barrels) of oil.

The J1 event is difficult to resolve and interpret in the low frequency normalized data but is imaged much more clearly in the whitened dataset (Figure 20). Therefore, it is not surprising to find that fewer significant differences were observed in the low frequency normalization (Figure 20b). The high frequency J1 difference map (Figure 20a) does show coherent dimming above the original oil-water contact. However, the differences observed updip do not provide a clear image of fluid changes, with pockets of both brightening and dimming being evident.

A useful strategy to gain the most time-lapse information from multiple closely stacked reservoirs such as the Bullwinkle J-sands would be to perform both a high and

low frequency normalization. Together, they should provide the most robust difference of the dominant events in the section, and more interpretable images of the thinner sands. Another approach would be to calculate the coherence between the two surveys as a function of frequency. One could then filter out frequencies displaying low coherence, leaving more coherent frequencies in the data. If sufficient high frequencies could be retained, then one would expect to be left with highly repeatable, yet usefully interpretable normalized seismic surveys.

## CONCLUSION

A poststack normalization procedure has allowed us to compare two vintages of legacy seismic data in order to successfully image drainage of the major Bullwinkle hydrocarbon reservoir. Additionally, the unique existence of two contemporaneous orthogonal pre-production surveys and the application of a spectral whitening procedure have enabled us to investigate the influence of survey orientation and bandwidth on time-lapse repeatability and interpretability.

The J2 turbidite event, the major Bullwinkle reservoir, exhibits extraordinary seismic dimming. The region of amplitude reduction corresponds to where production and log data show that the oil-water-contact has moved upwards in response to a strong water drive mechanism, indicating even drainage of the J2 reservoir. The magnitude of dimming is consistent with that predicted by Gassmann modeling of water replacing oil in the reservoir in combination with sediment compaction in response to pressure decline.

Our statistical methods of evaluating the similarity of the seismic datasets in areas unaffected by production, combined with our interpretations of seismic difference maps,

shows that time-lapse analysis results are strengthened by utilizing seismic surveys that were acquired in similar orientations. We have also shown that non-whitened surveys tend to have greater similarity after normalization and can give a clearer difference image of large seismic events. However, at Bullwinkle, this occurs at some extent to the expense of the ability to resolve smaller reservoirs nearby. Spectral whitening may therefore be useful if it is necessary to investigate changes in closely stacked hydrocarbon reservoirs.

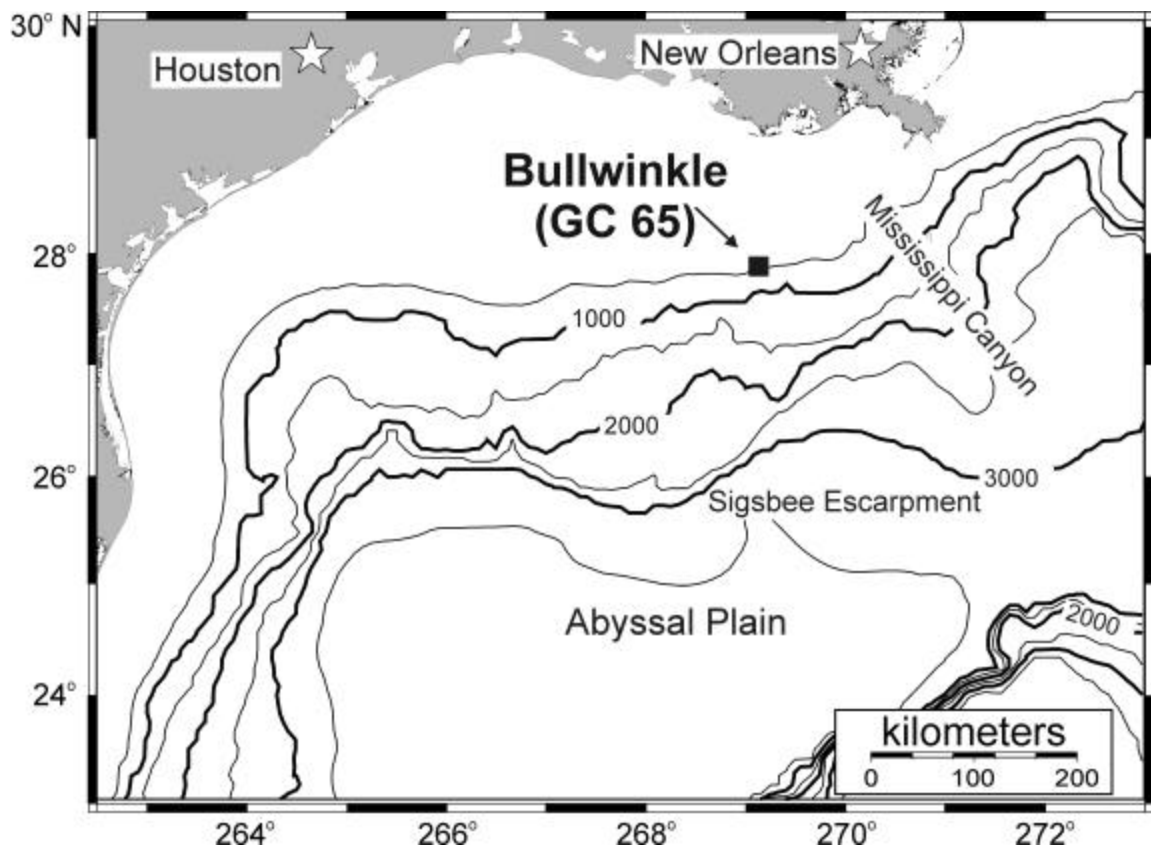


**Figure 1:** Location map showing the Gulf of Mexico and the Texas/ Louisiana coastline. Bathymetric contours are in meters, with an interval of 500 m. The Bullwinkle field is located in Green Canyon block 65, approximately 240 km southwest of New Orleans.



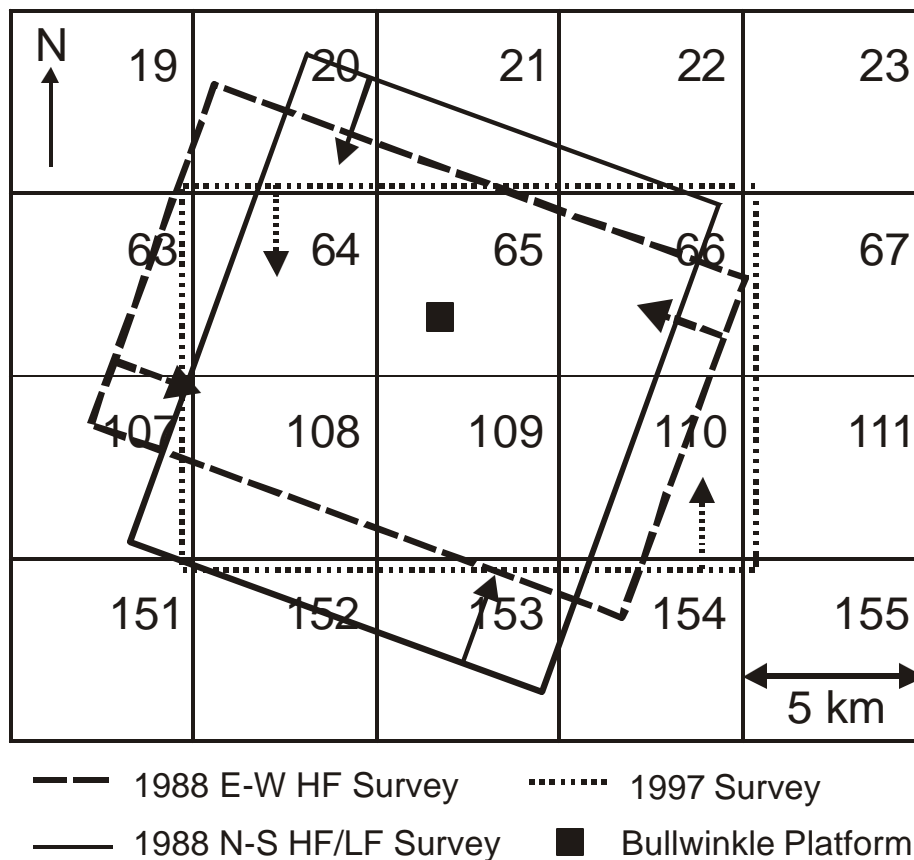


**Figure 2:** Green Canyon basemap showing the perimeters of the 3-D surveys considered in this project and location of the Bullwinkle platform. Arrows represent the survey acquisition directions. Numbered boxes signify the Green Canyon grid blocks. The 1988 surveys were acquired orthogonally to each other, prior to production from the field. The 1997 survey was shot due north-south, after over eight years of production.

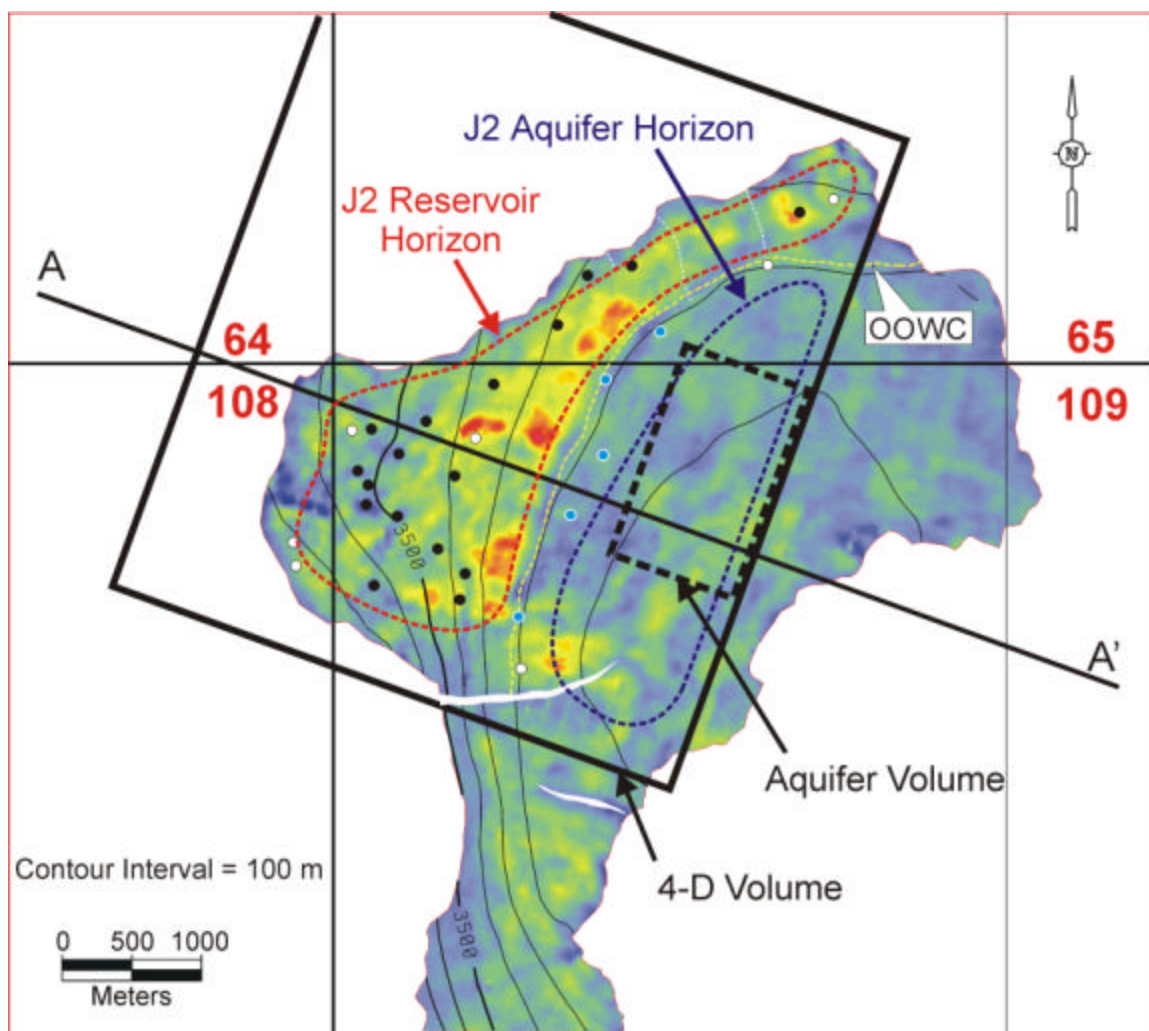


**Figure 3:** Amplitude and depth-converted structure map of the J2 event showing the lateral extent of the 4-D Volume (solid box), which extends from 3.1 to 4.0 seconds in two-way travel time. The dashed box represents the Aquifer Region used to determine the normalization parameters. The dashed red and dark blue lines delimit the J2 Aquifer Horizon and J2 Reservoir Horizon, respectively. Circles delineate well penetrations; black circles represent production wells, blue circles are injection wells and white circles show the location of other penetrations. A-A' corresponds to the cross-section presented in Figure 4.

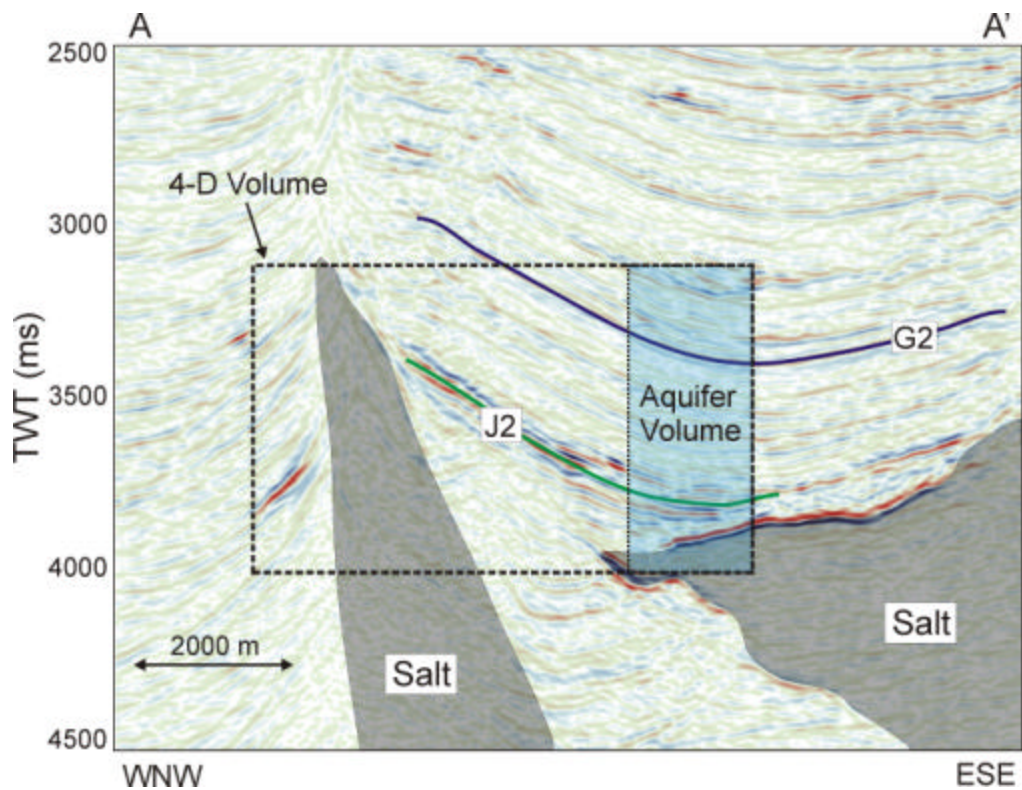


**Figure 4:** WNW-ESE (crossline) seismic section A-A' from the 1988 N-S HF survey, showing the extent of the 4-D Volume and the Aquifer Volume. The G2 and J2 horizons and adjacent salt bodies are delineated.

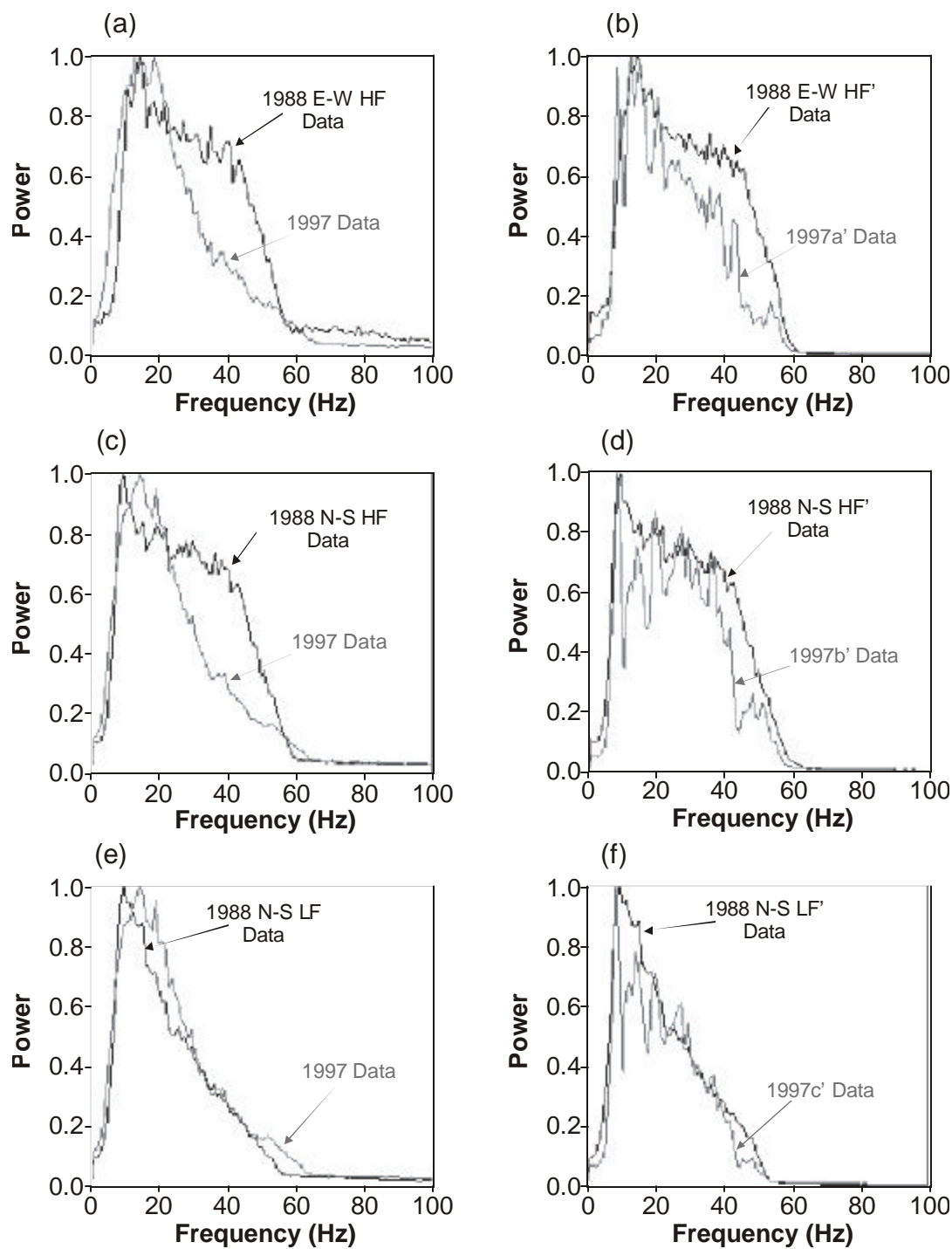


**Figure 5:** Power spectra of the 1997 (gray) and 1988 (black) surveys. The left column shows the survey spectra after only rebinning of the 1997 survey in (a) the E-W HF normalization, (c) the N-S HF normalization, and (e) the N-S LF normalization. The right column contains the survey spectra after normalization in (b) the E-W HF normalization, (d) the N-S HF normalization, and (f) the N-S LF normalization.

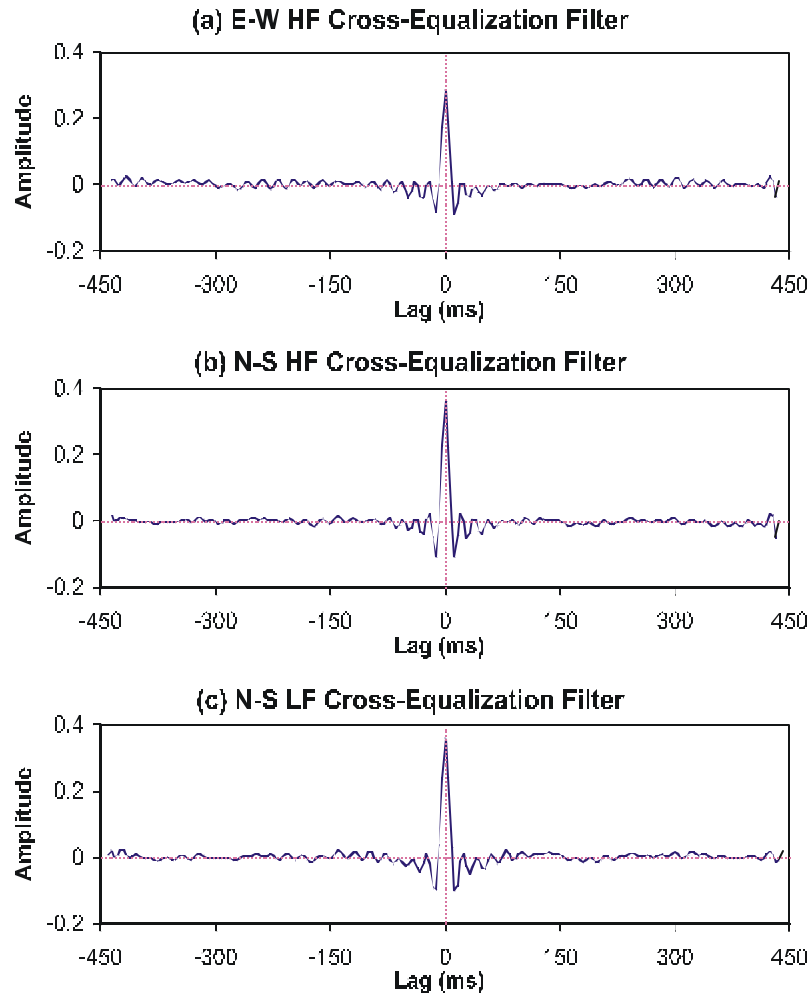


**Figure 6:** Cross-equalization filters used to reshape the 1997 data to match the 1988 data in (a) the E-W HF normalization, (b) the N-S HF normalization, and (c) the N-S LF normalization. Greatest energy is centered upon zero lag time, indicating that the filters do not time-shift the 1997 data.

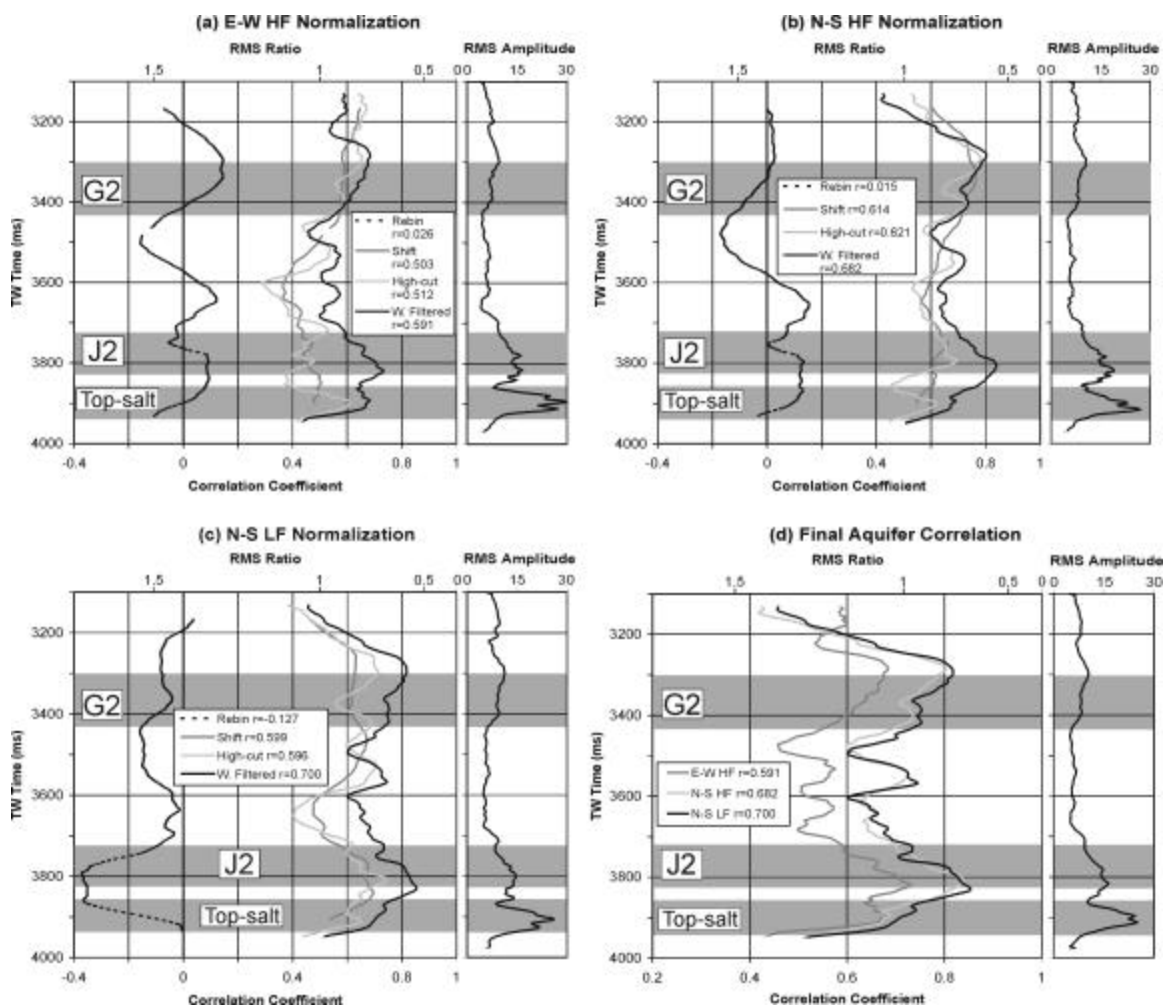


**Figure 7:** Correlation between the 1997 and 1988 seismic data in the Aquifer Volume in (a) the E-W HF normalization, (b) N-S HF normalization, (c) and N-S LF normalization. Correlation is calculated over a 60 ms moving time window after rebinning (Rebin), global shifting (Shift), high-cut filtering (High-cut) and cross-equalization (W. Filtered). The equivalent RMS ratio (equation (6)) is shown on the secondary  $x$ -axis. Correlation increases in every case after each normalization step, but most significantly with global shifting. Correlation also tends to be higher where amplitudes are strongest, as shown by the 1988 survey RMS amplitude plots. The plot of final aquifer correlation for all three normalizations (d) shows that overall correlation is greatest in the N-S LF normalization and least in the E-W normalization. The gray horizon bands represent the vertical extent of the G2, J2, and top-salt events in the Aquifer Volume.



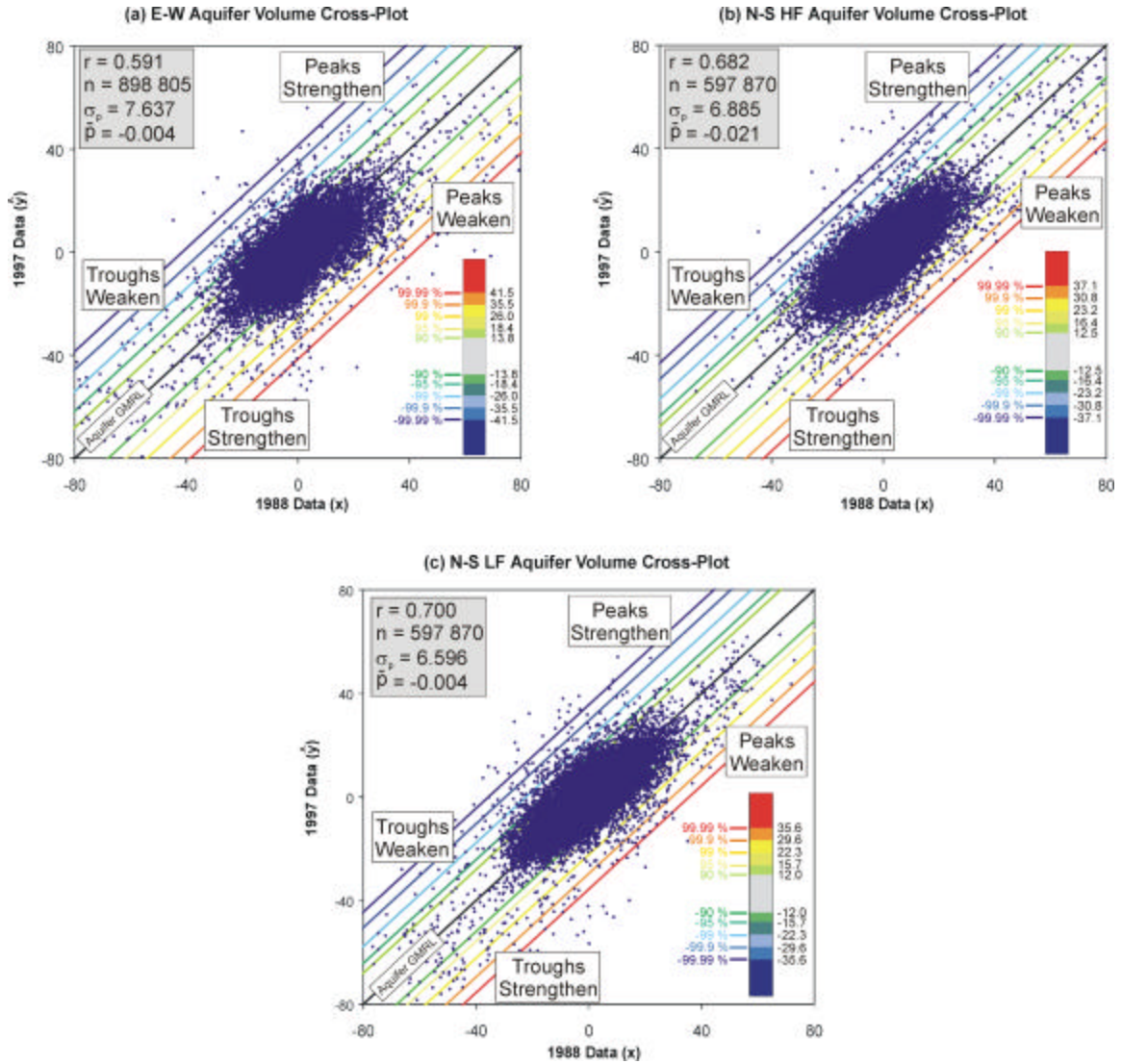


**Figure 8:** Cross-plots of normalized 1997 amplitudes ( $\hat{y}$ ) versus normalized 1988 amplitudes ( $x$ ) from the Aquifer Volume (Table 2) in (a) the E-W HF normalization, (b) the N-S HF normalization, and (c) the N-S LF normalization. The geometric mean regression lines (equation (4)) (black lines) and prediction bands (colored lines) are shown. The prediction band value corresponds to the color key legend. The mean difference ( $m$ ) between the 1988 and 1997 data is also calculated. The N-S LF cross-plot (c) exhibits least scatter in the cross-plot and has correspondingly narrowest prediction bands, greatest correlation ( $r$ ) (equation (2)), and lowest difference volume standard deviation ( $s_p$ ) (equation (7)). Conversely, the E-W HF cross-plot (a) exhibits most scatter in the cross-plot and therefore has the widest prediction bands, lowest correlation ( $r$ ), and greatest difference volume standard deviation ( $s_p$ ). The Aquifer Volumes cover the same area, but the E-W HF normalization contains a greater number of data points ( $n$ ) because the bin size is smaller in the E-W direction.

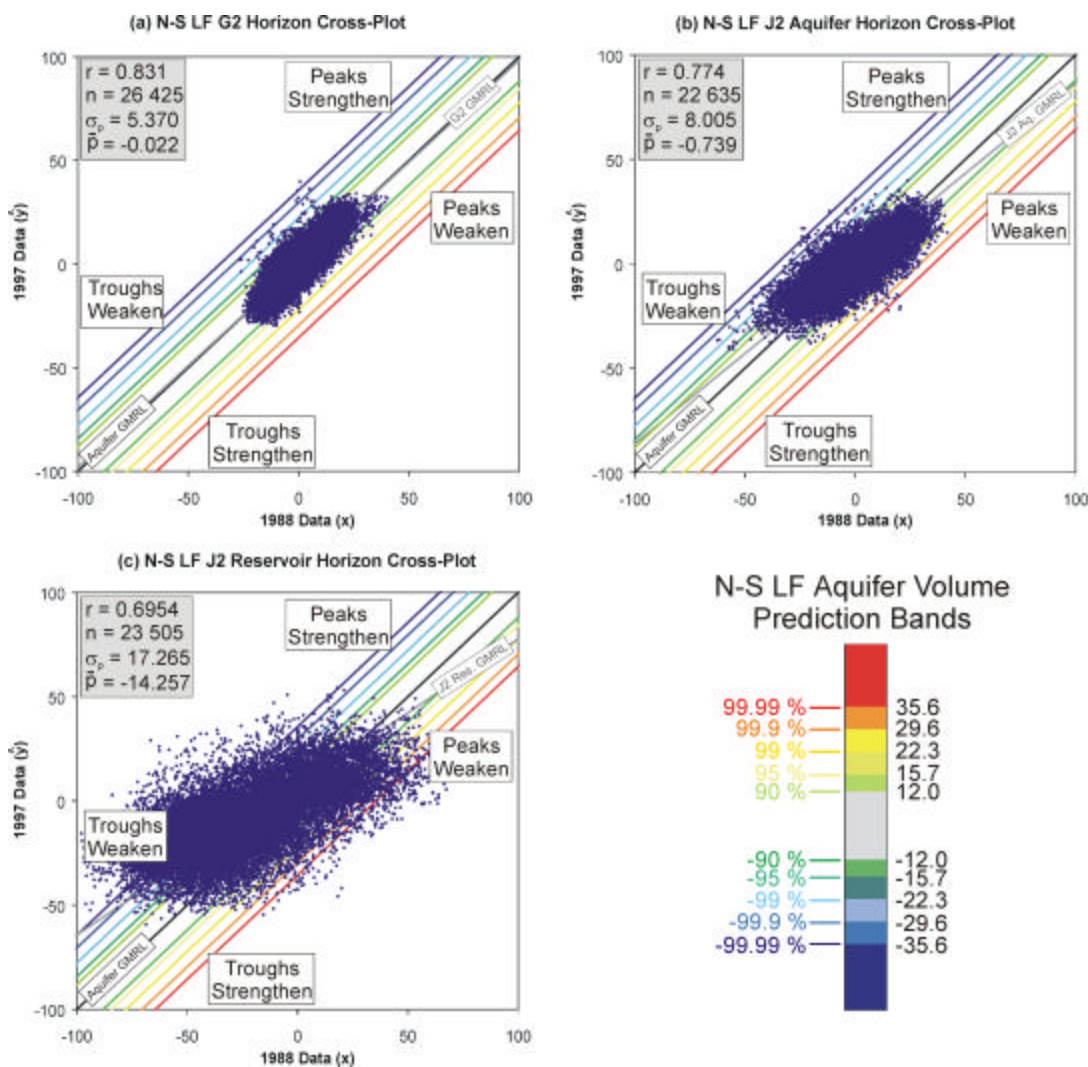


**Figure 9:** Cross-plots of 1997c' amplitudes ( $\hat{y}$ ) versus 1988 N-S LF' amplitudes ( $x$ ) taken from 40 ms time windows centered on (a) the G2 Horizon, (b) the J2 aquifer region, and (c) the J2 reservoir region. The geometric mean regression line and prediction bands from the N-S LF normalization aquifer region are plotted in the same way as Figure 8c. Also shown are the geometric mean regression lines for the plotted horizon data (equation 4) (gray lines). Cool prediction band colors show that the absolute value of a trough (negative amplitude) decreases over time (dimming), or that a peak (positive amplitude) strengthens. Warm colors represent a trough increasing in amplitude over time (brightening), or a peak weakening. The G2 cross-plot exhibits least scatter and has correspondingly narrowest prediction bands, greatest correlation ( $r$ ), and lowest difference volume standard deviation ( $\sigma_p$ ). The trend of the data follows the Aquifer Volume regression line (black line) indicating that the G2 Horizon rock and fluid properties have not changed over time. The J2 Aquifer Horizon amplitudes have greater scatter and tend to weaken slightly over time. The J2 Reservoir Horizon cross-plot contains a large number of troughs that have reduced in amplitude sufficiently to lie outside the 99.99 % prediction band, indicating that very significant dimming has occurred.



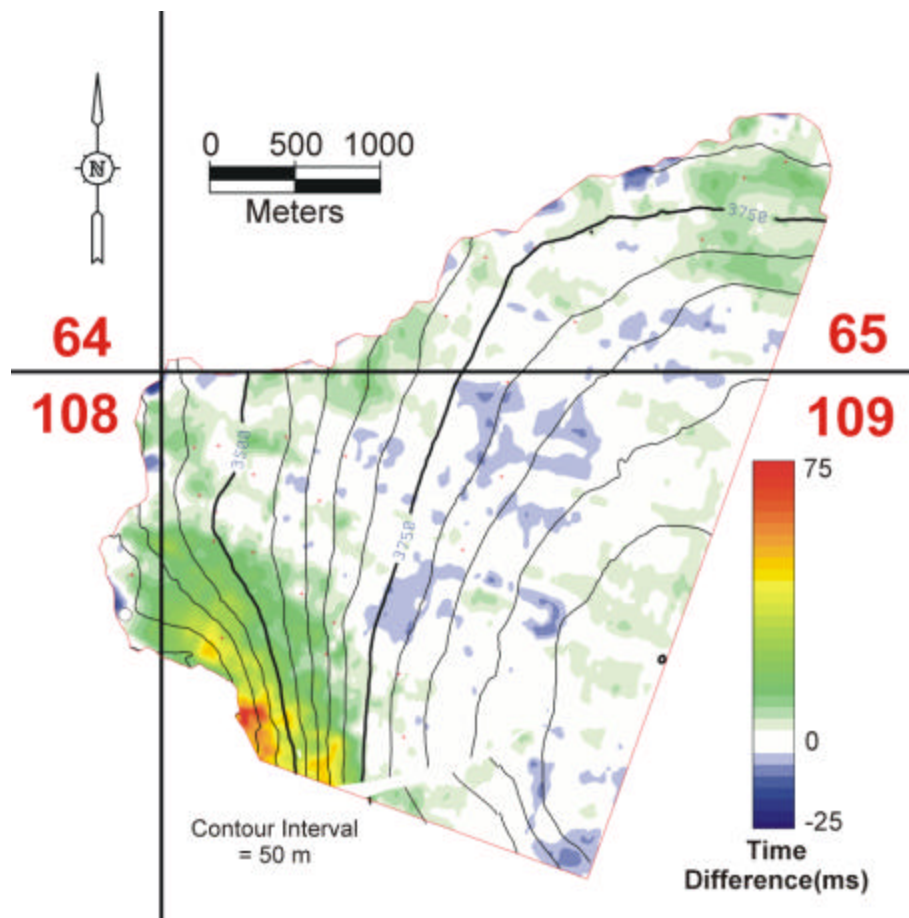


**Figure 10:** Travel time difference map for the J2 horizon produced by subtracting the J2 event interpreted in the 1997c' 4-D Volume from the 1988 N-S LF' J2 interpretation. The horizon travel times are similar where the dip is gentle, but the 1997c' J2 horizon is imaged over 50 ms above the 1988 N-S LF' J2 event where the dip is steepest.

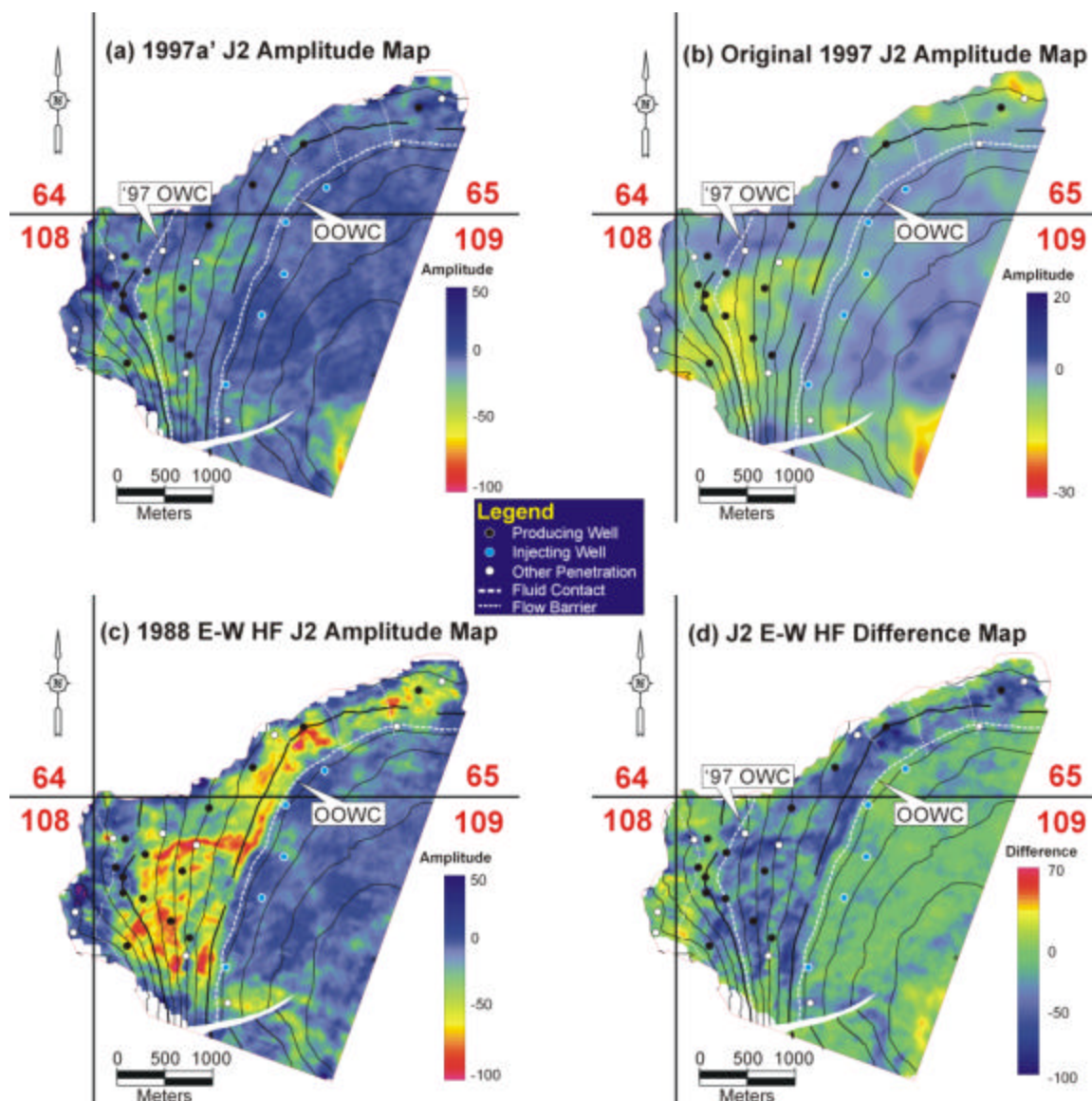


**Figure 11:** Amplitude and difference maps of the J2 event in the E-W HF normalization: (a) 1997a', (b) original 1997, (c) 1988 E-W HF, and (d) difference of 11(a) and 11(c). The amplitude maps were created by extracting the interpreted maximum trough (or occasionally peak) corresponding to the J2 event. The J2 well penetrations and depth converted structure contours (50 m contour interval) are delineated. Warm colors correspond to large negative amplitudes and to where the J2 event has increased in absolute amplitude over time (brightening). Cool colors represent small amplitudes and where the J2 event has decreased in absolute amplitude over time (dimming).

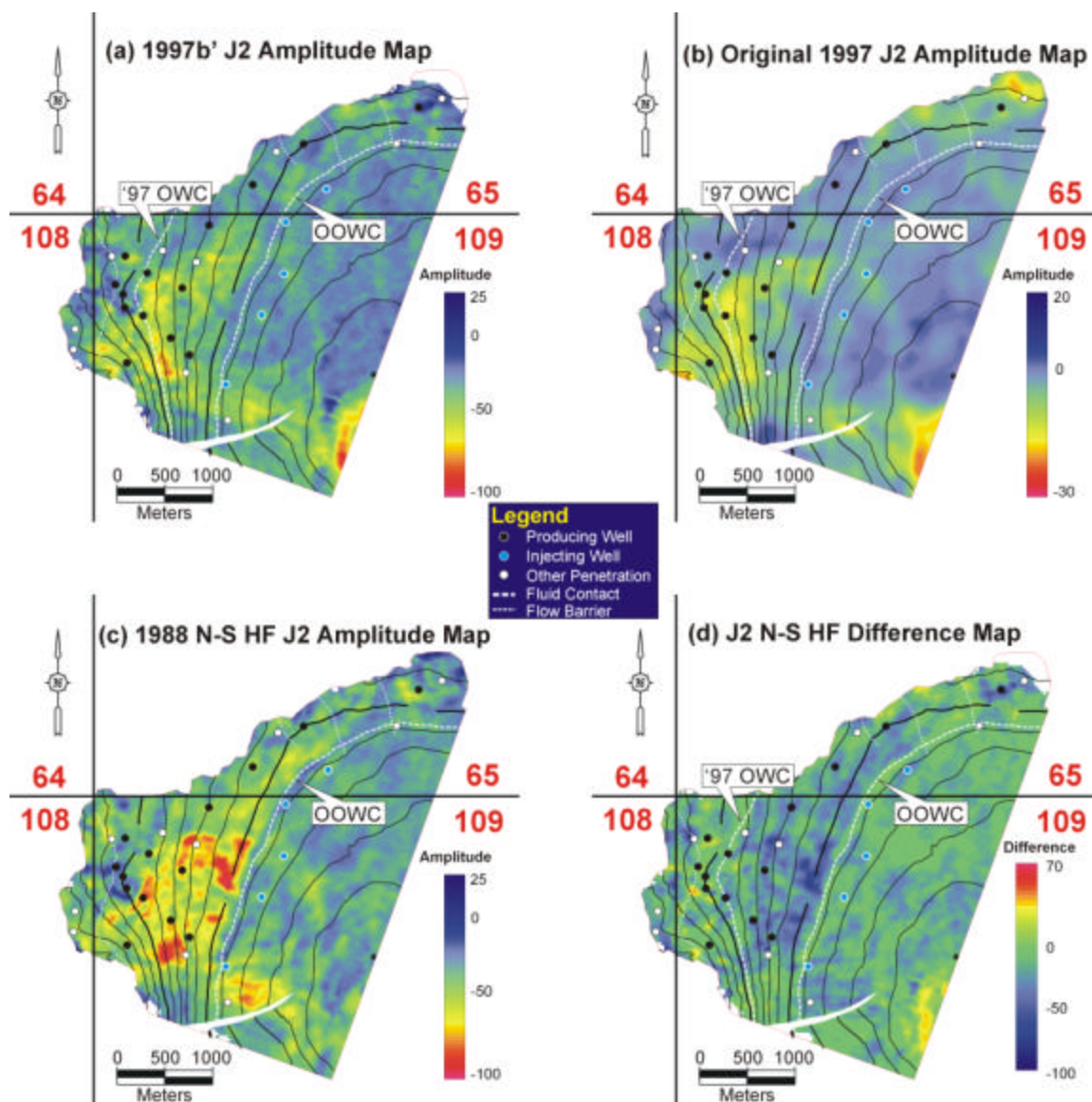


**Figure 12:** Amplitude and difference maps of the J2 event in the N-S HF normalization: (a) 1997b', (b) original 1997, (c) 1988 H-S HF', and (d) difference of 12(a) and 12(c). The amplitude maps were created by extracting the interpreted maximum trough (or occasionally peak) corresponding to the J2 event. The J2 well penetrations and depth converted structure contours (50 m contour interval) are delineated. Warm colors correspond to large negative amplitudes and to where the J2 event has increased in absolute amplitude over time (brightening). Cool colors represent small amplitudes and where the J2 event has decreased in absolute amplitude over time (dimming).



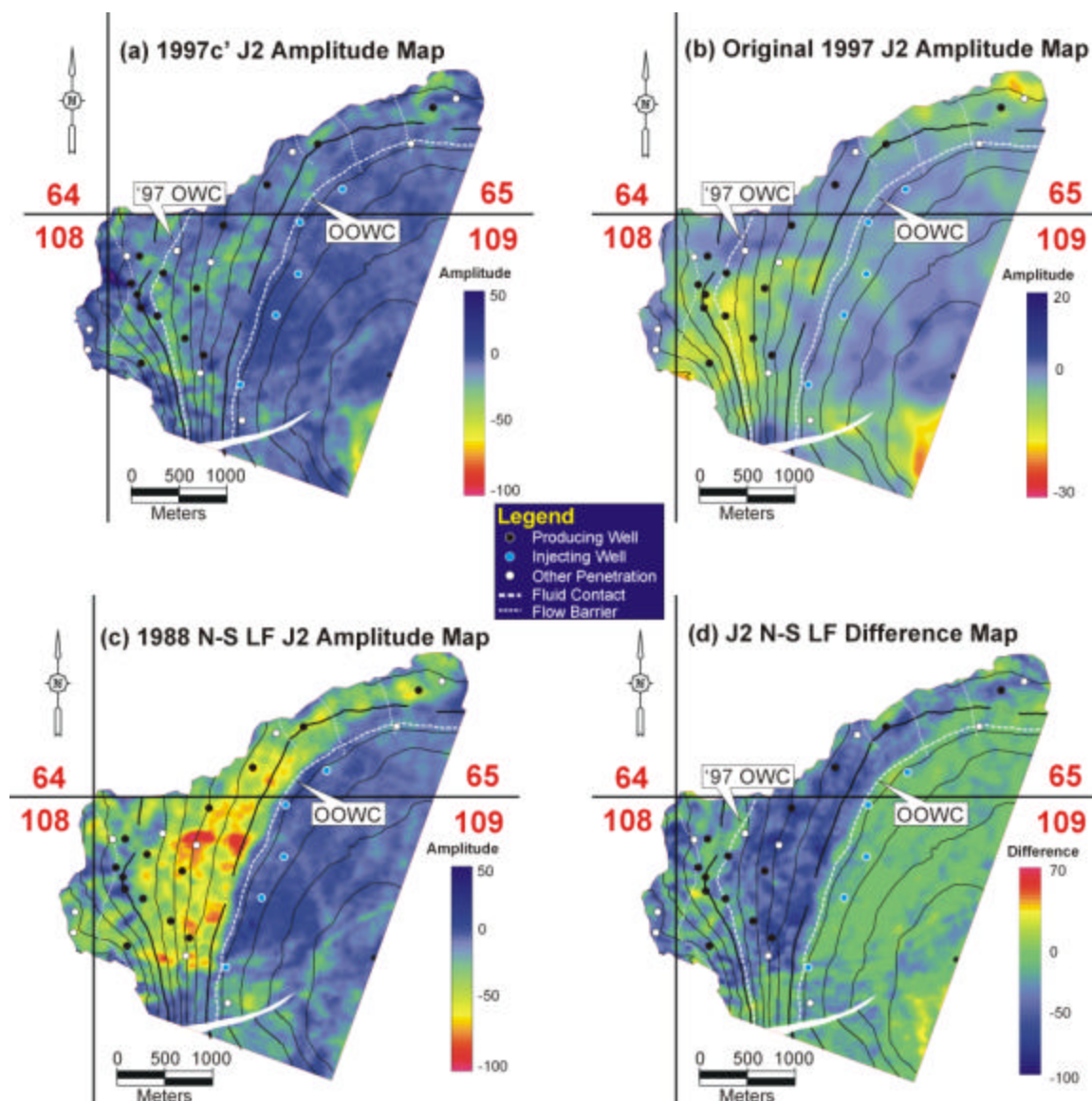


**Figure 13:** Amplitude and difference maps of the J2 event in the N-S LF normalization: (a) normalized 1997, (b) original 1997, (c) normalized 1988, and (d) difference of 13(a) and 13(c). The amplitude maps were created by extracting the interpreted maximum trough (or occasionally peak) corresponding to the J2 event. The J2 well penetrations and depth converted structure contours (50 m contour interval) are delineated. Warm colors correspond to large negative amplitudes and to where the J2 event has increased in absolute amplitude over time (brightening). Cool colors represent small amplitudes and where the J2 event has decreased in absolute amplitude over time (dimming).

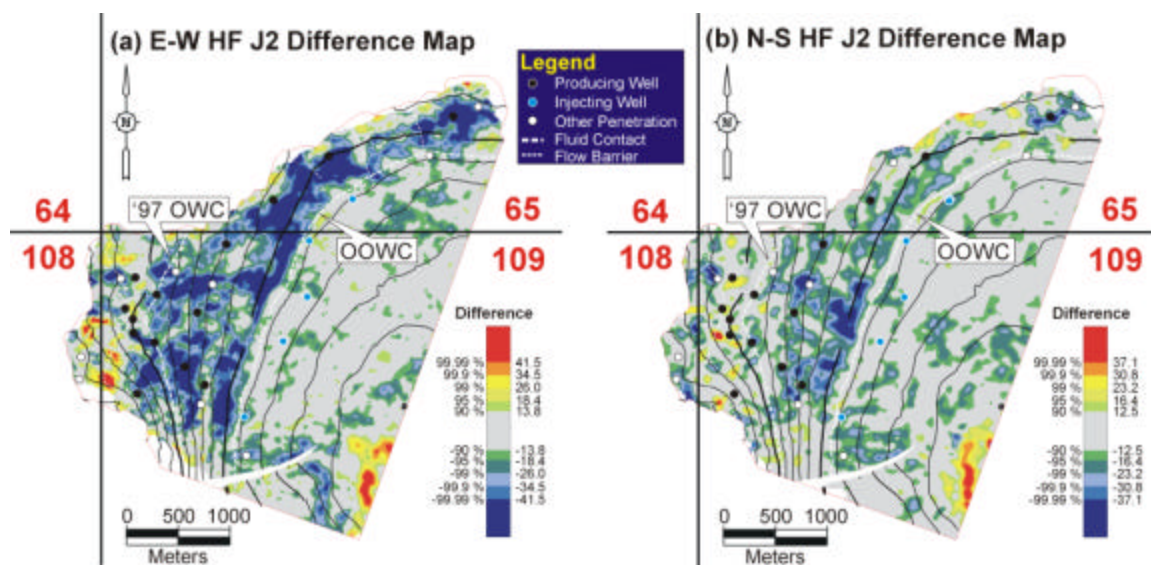


**Figure 14:** J2 difference map from the E-W HF normalization (a) and the N-S HF normalization (b), displayed with 90 %, 95 %, 99 %, 99.9 %, and 99.99% prediction bands derived from their respective Aquifer Volumes. The color scheme is derived from the Aquifer Volume cross-plots, with warm colors corresponding to where the J2 event has increased in absolute amplitude over time (brightening) and cool colors showing where the J2 event has decreased in absolute amplitude (dimming). Gray indicates small changes that are indistinguishable from noise. Thick dashed white lines denote the original and 1997 oil-water contacts interpreted from well and production data. Thin dashed white lines demark barriers in the reservoir across which fluids cannot flow over production time-scales. J2 well penetrations and depth converted structure contours (50 m contour interval) are also shown. The region of dimming (negative differences) between the original and 1997 oil-water contacts is interpreted to represent the replacement of oil with water in the reservoir. The E-W HF map shows more consistent dimming, but this extends above the 1997 OWC and casts doubt on the difference image.

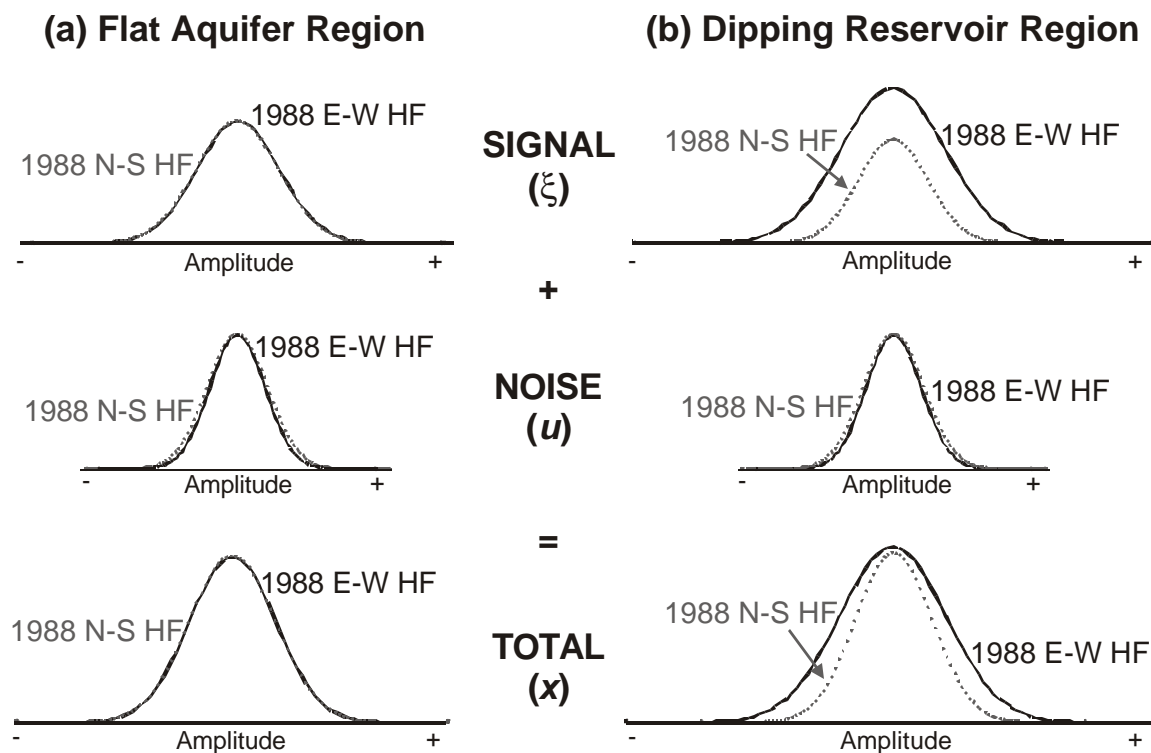


**Figure 15:** Diagrammatic amplitude histograms for the 1988 E-W HF survey (black, solid lines) and the 1988 N-S HF survey (gray, dashed lines) in (a) the Aquifer Volume, and (b) the reservoir region. The total seismic amplitude distribution ( $x$ ) is assumed to be composed of noise ( $u$ ), and signal ( $\xi$ ). The noise variance in the 1988 surveys ( $\sigma_u^2$ ) is assumed to be smaller than the signal variance ( $\sigma_x^2$ ). In the shallowly dipping Aquifer Volume, events are imaged similarly. In the dipping reservoir region, greater signal is recorded in the 1988 E-W HF survey. Therefore, the total seismic record has greater variance in the 1988 E-W HF survey than the 1988 N-S HF survey in the J-sand reservoirs.

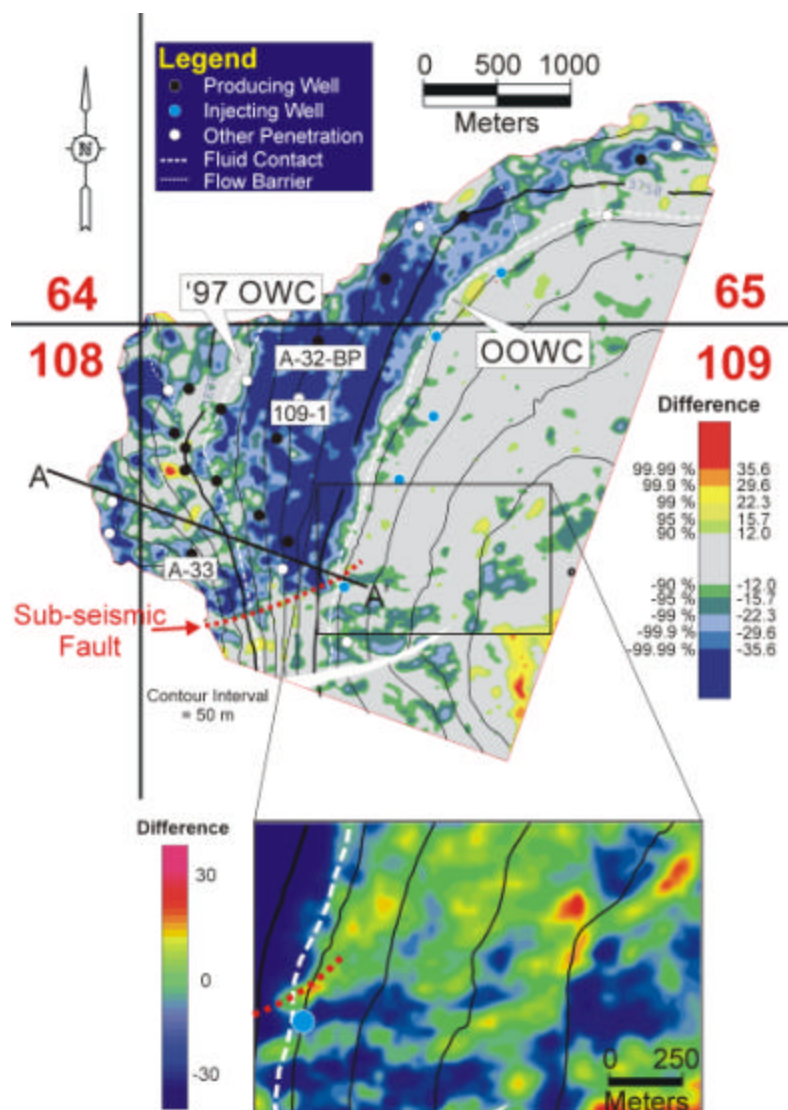


**Figure 16:** J2 difference map from the N-S LF normalization displayed with 90 %, 95 %, 99 %, 99.9 %, and 99.99% prediction bands derived from the N-S LF Aquifer Volume. The color scheme is derived from the Aquifer Volume cross-plots, with warm colors corresponding to where the J2 event has increased in absolute amplitude over time (brightening) and cool colors showing where the J2 event has decreased in absolute amplitude (dimming). Thick dashed white lines denote the original and 1997 oil-water contacts interpreted from well and production data. Thin dashed white lines demarcate barriers in the reservoir across which fluids cannot flow over production time-scales. J2 well penetrations and depth converted structure contours (50 m contour interval) are also shown. The annotated wells names correspond to the wells described in Figures 17 and 18. The region of dimming (negative differences) between the original and 1997 oil-water contacts is interpreted to represent the replacement of oil with water in the reservoir, and appears to terminate against a small fault that does not offset the J2 event in the seismic data. The enlarged aquifer section (within the black box) emphasizes weak dimming of the J2 aquifer though the use of an expanded color scale. The line A-A' corresponds to the seismic cross-section in Figure 19.

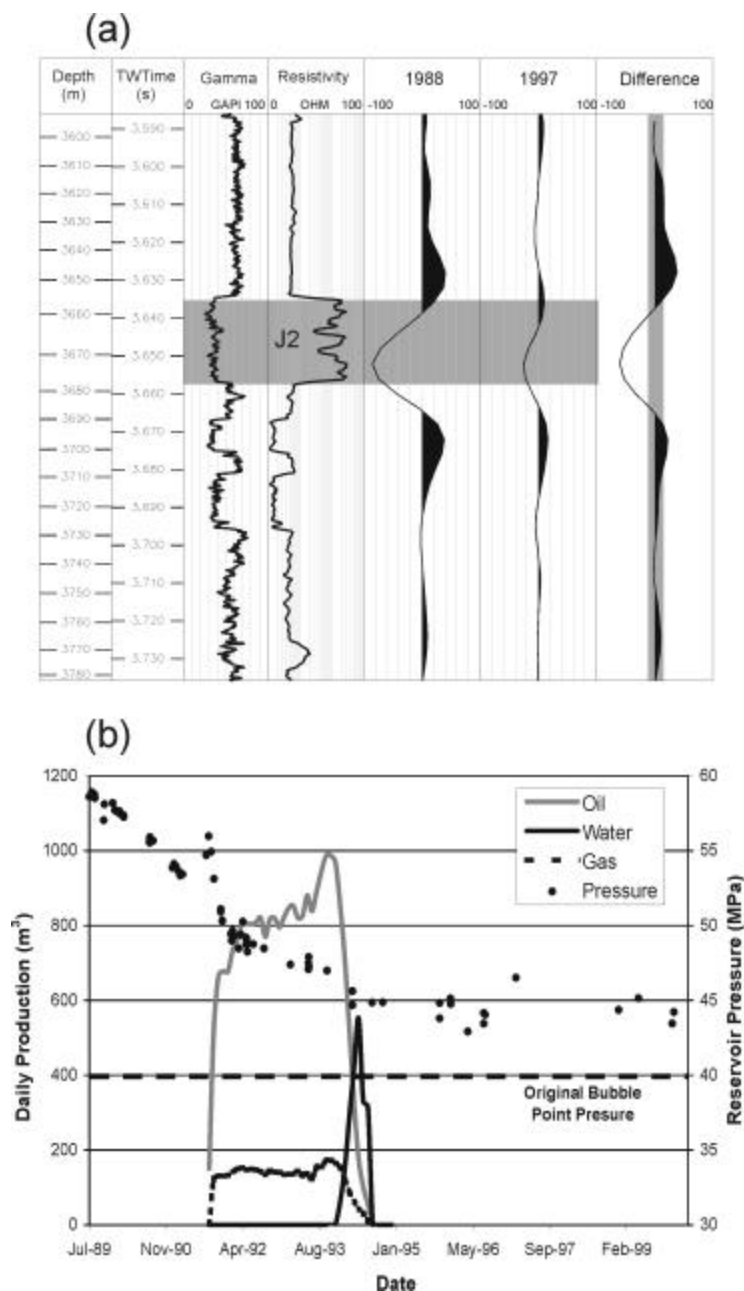


**Figure 17:** Normalized traces extracted from the 1988 and 1997 N-S LF normalization volumes at the location of well 109-1, and the difference between them (a). Also shown are the gamma ray and resistivity logs and the J2 sand. The 1997 trace dims substantially, by 71 %, resulting in a difference that lies well outside the 90 % prediction bands (gray box). The production history plot from nearby well A-32-BP (b) shows the well watering out in 1994, when water production (black line) increases and oil (gray line) and gas (dashed line) production falls off. This occurs when the reservoir pressure (circles) is well above the original bubble point pressure (horizontal dashed line).



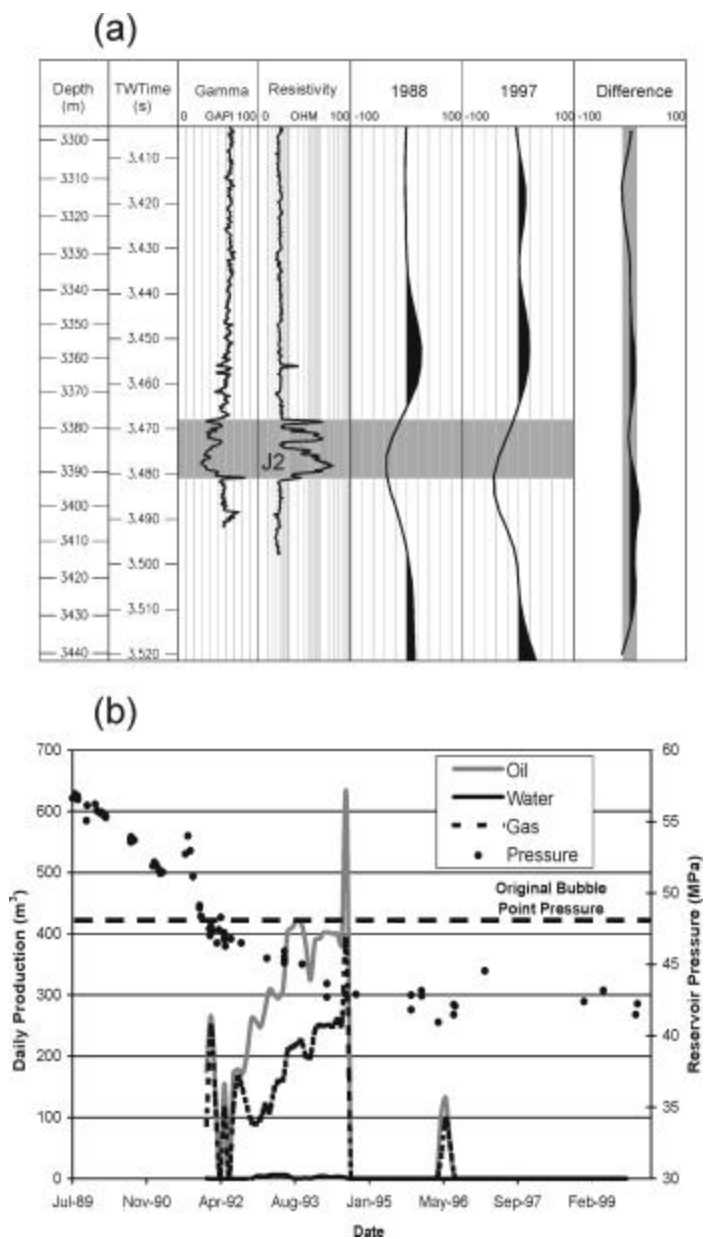


**Figure 18:** Normalized traces extracted from the 1988 and 1997 N-S LF normalization volumes at the location of updip well A33, and the difference between them (a). The extracted traces were re-aligned by shifting the 1997 trace downwards by 24 ms. Also shown are the gamma ray and resistivity logs and the J2 sand. The 1997 trace tends to brighten at the J2 horizon level, but the amplitude difference that lies within the 90 % prediction bands (gray box). The production history plot from nearby well A-32-BP (b) shows gas production (dashed line) increasing in 1992 as the reservoir pressure (circles) drops below the original bubble point pressure (horizontal dashed line). The bubble point pressure is greater than in well A-32-BP because heavier hydrocarbon components have been drawn up into the well.

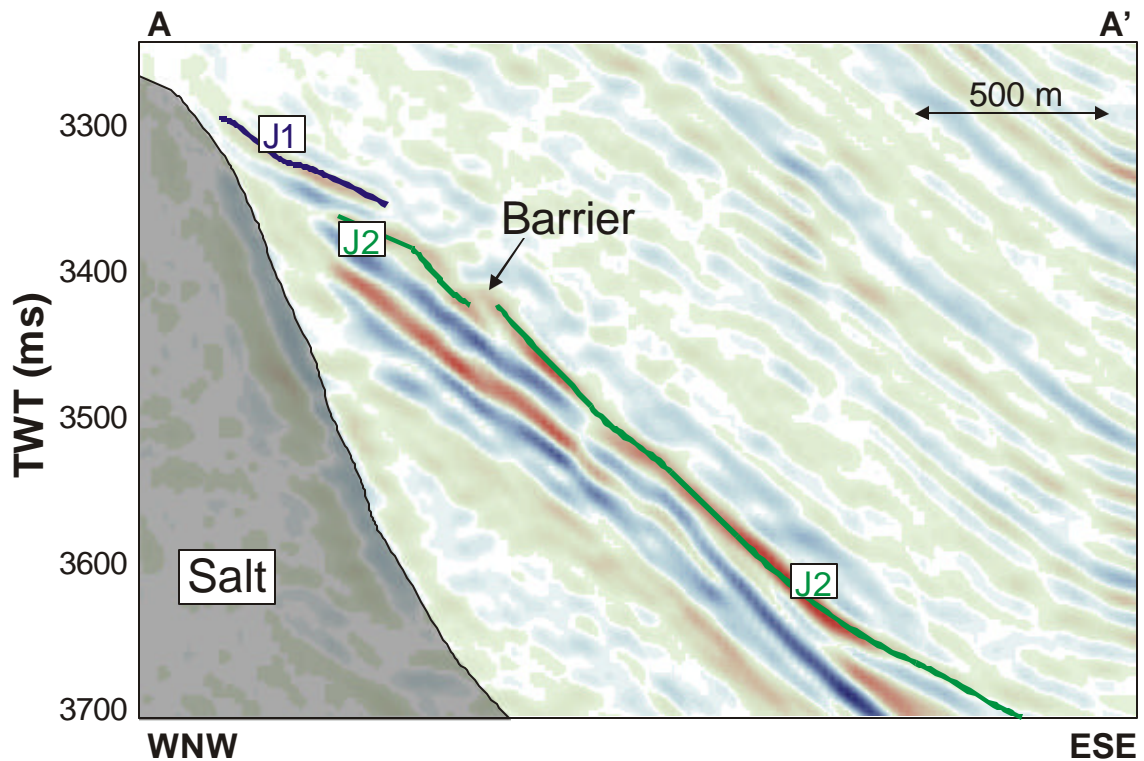


**Figure 19:** Cross-section A-A' (depicted on Figure 16) from the 198 N-S HF' survey, illustrating the seismic discontinuity separating the uppermost J2 sand from the main J2 reservoir. The discontinuity is interpreted to be a flow barrier since the upper J2 compartment has a different pressure regime and contains a perched oil-water-contact.

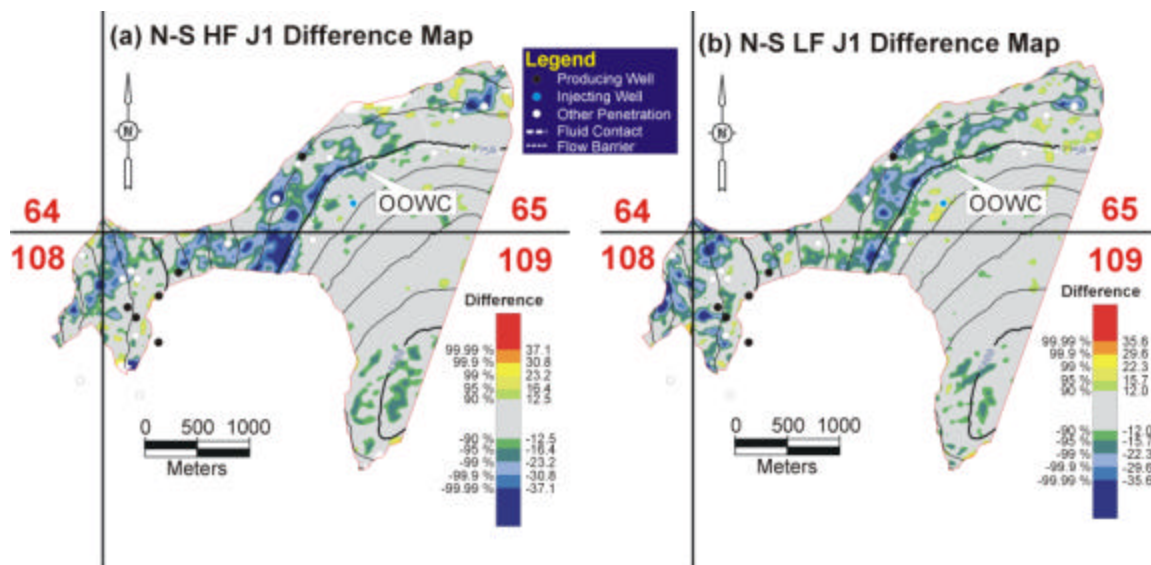


**Figure 20:** J1 difference map from the N-S LF normalization (a) and the N-S HF normalization (b), displayed with 90 %, 95 %, 99 %, 99.9 %, and 99.99% prediction bands from the N-S LF aquifer volume. The color scheme is derived from the Aquifer Volume cross-plots, with warm colors corresponding to where the J1 event has increased in absolute amplitude over time (brightening) and cool colors showing where the J1 event has decreased in absolute amplitude (dimming). Thick dashed white lines denote the original oil-water contacts interpreted from well and seismic data. Thin dashed white lines demark barriers in the reservoir across which fluids cannot flow over production time-scales. J1 well penetrations (producing wells are colored black) and depth converted structure contours (50 m contour interval) are also shown. The N-S HF map shows greater dimming where the oil-water-contact has swept upwards, but both maps inexplicably exhibit dimming in updip regions.

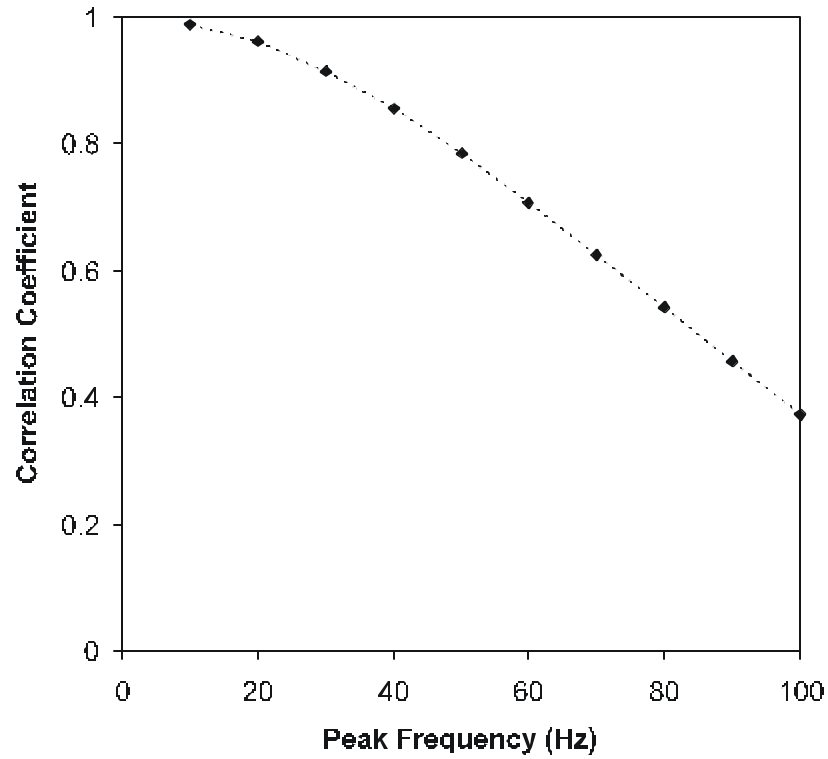


**Figure 21:** Graph of the correlation coefficient between two Ricker wavelets offset by 4 ms as a function of peak frequency. The wavelets are almost perfectly correlated at low frequencies. However, their correlation is reduced to less than 0.4 at 100 Hz when the 4 ms time-shift becomes a much more significant proportion of their wavelength.

**Table 1:** Nomenclature

Variable	Description	Variable	Description
$\mathbf{h}$	Set of amplitudes from true earth response (signal) in normalized 1997 data	$b_1$	Slope of GMRL
$\bar{\mathbf{h}}$	Mean of $\mathbf{h}$	$n$	Number of observations / samples
$\mathbf{m}$	Mean of horizon amplitudes	$p$	Set of perpendicular distances of amplitudes from GMRL,
$\mathbf{s}_{diff}$	Standard deviation of the set of differences ( $x-y$ )	$\bar{p}$	Mean of $p$
$\mathbf{s}_h$	Standard deviation of $\mathbf{h}$	$r$	Correlation coefficient
$\mathbf{s}_p$	Standard deviation $p$	$u$	Set of error amplitudes in the normalized 1988 data
$\mathbf{s}_p^2$	Variance of $p$	$\bar{u}$	Mean of $u$
$\mathbf{s}_\xi$	Standard deviation of $\xi$	$v$	Set of error amplitudes in the normalized 1997 data
$\mathbf{s}_u$	Standard deviation of $u$	$\bar{v}$	Mean of $v$
$\mathbf{s}_u^2$	Variance of $u$	$x$	Set of amplitudes from the 1988 data (after bandpass filtering)
$\mathbf{s}_v$	Standard deviation of $v$	$\bar{x}$	Mean of $x$
$\mathbf{s}_v^2$	Variance of $v$	$x_i$	Value of $x$ at the $i$ th location
$\mathbf{s}_x$	Standard deviation of $x$	$y$	Set of amplitudes from the 1997 data
$\mathbf{s}_x^2$	Variance of $x$	$\bar{y}$	Mean of $y$
$\mathbf{s}_{xy}$	Covariance of $x$ and $y$	$y_i$	Value of $y$ at the $i$ th location
$\mathbf{s}_y$	Standard deviation of $y$	$\hat{y}$	Set of normalized amplitudes from the 1997 data
$\mathbf{x}$	Set of amplitudes from true earth response (signal) in normalized 1988 data	$\bar{\hat{y}}$	Mean of $\hat{y}$
$\bar{\mathbf{x}}$	Mean of $\mathbf{x}$	$\hat{y}_i$	Value of $\hat{y}$ at the $i$ th location
$b_0$	Y-intercept for GMRL		

**Table 2:** Definition of Acronyms and Abbreviations

<b>Acronym</b>	<b>Description</b>
<i>1988 E-W HF</i>	1988 east-west high frequency (whitened) survey. Extent defined in Figure 2, processing flow in Table 3.
<i>1988 N-S HF</i>	1988 north-south high frequency (whitened) survey. Extent defined in Figure 2, processing flow in Table 3.
<i>1988 N-S LF</i>	1988 north-south low frequency (non-whitened) survey. Extent defined in Figure 2, processing flow in Table 3.
<i>1997</i>	1997 survey. Extent defined in Figure 2, processing flow in Table 3.
<i>1988 E-W HF'</i>	1988 E-W HF survey after bandpass filtering.
<i>1988 N-S HF'</i>	1988 N-S HF survey after bandpass filtering.
<i>1988 N-S LF'</i>	1988 N-S LF survey after bandpass filtering.
<i>1997a'</i>	1997 survey normalized to the 1988 E-W HF survey
<i>1997b'</i>	1997 survey normalized to the 1988 N-S HF survey
<i>1997c'</i>	1997 survey normalized to the 1988 N-S LF survey
<i>E-W HF</i>	Normalization of 1997 survey with 1988 E-W HF survey
<i>N-S HF</i>	Normalization of 1997 survey with 1988 N-S HF survey
<i>N-S LF</i>	Normalization of 1997 survey with 1988 N-S LF survey
<i>4-D Volume</i>	Seismic volume used for time-lapse analysis. Extent defined in Figures 3 and 4.
<i>Aquifer Volume</i>	Water-saturated sub-volume of 4-D volume used to calculate normalization parameters. Extent defined in Figures 3 and 4.
<i>BBL</i>	Barrel of fluid (1 BBL = 0.159 m <sup>3</sup> )
<i>EOR</i>	Enhanced Oil Recovery
<i>G2 Horizon</i>	Region of the G2 horizon from which horizon cross-plot and minimum trough amplitudes were extracted. Extent defined in Figures 3 and 4.
<i>GOR</i>	Gas-oil ratio (SCF/STB)
<i>J2 Aquifer Horizon</i>	Aquifer region of the J2 horizon from which horizon cross-plot and minimum trough amplitudes were extracted. Extent defined in Figures 3 and 4.
<i>J2 Reservoir Horizon</i>	Reservoir region of the J2 horizon from which horizon cross-plot and minimum trough amplitudes were extracted. Extent defined in Figures 3 and 4.
<i>MMBBL</i>	Million barrels

**Table 2:** Definition of Acronyms and Abbreviations (cont.)

<b>Acronym</b>	<b>Description</b>
<i>MMBOE</i>	Million barrels of oil-equivalent
<i>OWC</i>	Oil-water contact
<i>OOWC</i>	Original oil-water contact
<i>PNC</i>	Pulsed Neutron Capture
<i>RFC</i>	Reflection Coefficient
<i>RMS</i>	Root-mean-square (equation (A-2))
<i>SCF</i>	Cubic feet (of gas) at standard conditions ( $1 \text{ ft}^3 = 0.028 \text{ m}^3$ )
<i>SNR</i>	Signal-to-noise ratio
<i>STB</i>	Barrel of fluid at standard conditions
<i>TWT</i>	Two-way travel time

**Table 3:** Processing flow summary for the 1988 N-S HF and the 1997 surveys.

1988 N-S HF Survey	1997 Survey
Orientation: 020-200° Number of cables: 2 Maximum Offset: 3980 m Number of vessels: 2 Source depth: 9 m Nominal fold: 20 Sampling interval: 3 ms Summation of adjacent traces Bin size: 15 m inline, 46 m crossline	Orientation: 360-180° Number of cables: 6 Maximum Offset: 6010 m Number of vessels: 1 Source depth: 6 m Nominal fold: 39 Sampling interval: 4 ms Bandpass filter: 3-90 Hz Bin size: 12.5 m inline, 40 m crossline
Source signature deconvolution Natural binning Spherical spreading compensation Noise spike attenuation Sort to CMP gathers Mute and offset weighting 3-D DMO Dip corrected interpolation ⇒ 31 m inline, 23 m crossline Inverse NMO Deabsorption NMO Offset interpolation Inverse NMO Integration Low-cut: 4 Hz Ramp: -3dB/octave Two-pass inline Prestack Time Migration NMO Offset Interpolation Inverse NMO Two-pass crossline Prestack Migration Final Stack Post-stack whitening <i>(Not performed on the 1988 N-S LF survey)</i>	Source signature deconvolution Spherical spreading compensation Navigation merge and sort to CMP gathers Q compensation Pre-stack predictive deconvolution NMO Mute 3-D DMO Weighted Stack Phase Rotation Statics Amplitude Scaling Poststack predictive deconvolution 3-D FXY filtering Low cut filter: 4 Hz FX Interpolation ⇒ 12.5 m inline, 20 m crossline 1 pass 3-D phase shift migration

The 1988 E-W HF survey was acquired and processed using a very similar methodology. However, its orientation was 070-290° and the final bin dimensions were 15 m inline, 31 m crossline.



**Table 4:** Global Shifts and High-Cut Filters applied to the 1997 Data during normalization.

Normalization Step		Normalization		
		E-W HF	N-S HF	N-S LF
Shift	Time	- 28 ms (up)	- 28 ms (up)	- 20 ms (up)
	Inline	15 m (east)	0 m	0 m
	Crossline	0 m	46 m (east)	46 m (east)
High-cut Filter (Applied to 1988 and 1997 volumes)		55 Hz	60 Hz	50 Hz

**Table 5:** Aquifer Volume Statistics

Statistic		Normalization					
		E-W HF		N-S HF		N-S LF	
		1988	1997	1988	1997	1988	1997
Before Amplitude Scaling	Mean	-0.282	0.003	0.170	0.003	-0.001	0.004
	$\sigma$	116.25	7.402	9.229	7.408	8.034	7.410
After Amplitude Scaling	Mean	0.000	0.000	0.000	0.000	0.000	0.000
	$\sigma$	10.000	10.000	10.000	10.000	10.000	10.000
S/N Ratio		1.559		1.794		1.900	
Correlation Coefficient		0.591		0.682		0.700	
RMS Ratio		0.825		0.767		0.775	

**Table 6:** Horizon Minimum-Trough Amplitude Extraction Statistics

Horizon		Normalization								
		E-W HF			N-S HF			N-S LF		
		1988	1997	Diff	1988	1997	Diff	1988	1997	Diff
G2	Mean	-13.73	-16.47	2.73	-19.35	-16.50	-2.85	-9.43	-12.05	2.62
	$\sigma$	6.29	5.76	6.24	6.73	5.61	6.16	5.28	5.68	5.08
J2 Aquifer	Mean	-7.69	-7.96	0.27	5.79	-3.57	-2.23	-14.55	-10.44	-4.11
	$\sigma$	8.69	5.64	9.21	9.02	7.37	8.152	9.70	7.26	8.38
J2 Reservoir	Mean	-48.94	-21.22	-27.73	-27.51	-15.97	-11.65	-50.05	-21.79	-28.26
	$\sigma$	22.57	12.23	22.23	17.04	13.83	14.64	16.03	10.01	16.81

**Table 7:** Final Normalized Correlation Coefficients and Difference Volume Standard Deviation

Normalization	Region	Correlation Coefficient	$S_p$ (to Aquifer Volume GMRL)
E-W HF	Aquifer Volume	0.591	7.637
	G2	0.780	6.155
	J2 Aquifer	0.597	11.763
	J2 Reservoir	0.685	24.217
N-S HF	Aquifer Volume	0.682	6.885
	G2	0.810	6.705
	J2 Aquifer	0.698	9.425
	J2 Reservoir	0.713	16.403
N-S LF	Aquifer Volume	0.700	6.596
	G2	0.831	5.370
	J2 Aquifer	0.774	8.005
	J2 Reservoir	0.695	17.265

**Table 8:** Prediction Band Widths (in Units of Amplitude)

Normalization	Confidence Level (%)				
	90	95	99	99.9	99.99
E-W	13.85	18.35	25.95	34.48	41.49
N-S HF	12.48	16.40	23.19	30.81	37.07
N-S LF	11.96	15.74	22.26	29.56	35.58

**Table 9:** Comparison of Achieved Repeatability in Time-Lapse Studies

Field	Author	Years Separating Surveys	Description	RMS ratio	Correlation Coefficient
ST 295, GOM	Burkhart et al., 2000	6	Poststack, Legacy	0.602	<b>0.819</b>
Draugen, NS	Koster et al., 2000	8	Parallel, TL	<b>0.35</b>	0.94
Foinaven, NS	Kristiansen et al., 2000	3	Parallel, TL	0.37	<b>0.93</b>
Foinaven, NS	Kristiansen et al., 2000	3	OBC, Parallel, TL	0.28	<b>0.96</b>
Gullfaks, NS	Landrø et al., 1999	10	Parallel, TL	<b>0.66</b>	0.782
GOM	Ricket and Lumley, 2001	12	Poststack, Legacy	<b>0.78</b>	0.71
Snore, NS	Smith et al., 2001	14	Poststack, TL	<b>0.733</b>	0.731
Snore, NS	Smith et al., 2001	14	Parallel, TL	<b>0.370</b>	0.932
Bullwinkle, GOM	This paper, 2001	9	Poststack, Legacy	0.775	<b>0.700</b>

Date = Date published, GOM = Gulf of Mexico, NS = North Sea, OBC = Ocean Bottom Cable surveys, Legacy = Legacy seismic data sets, Parallel = Surveys processed in parallel, or in the same way, TL = Surveys acquired for time-lapse purposes. Boldface type indicates the repeatability measure originally quoted. RMS ratio and correlation coefficient are mapped to each other through equation (A-9).

## APPENDIX A

### RMS RATIO – CORRELATION COEFFICIENT RELATIONSHIP IN NORMALIZED SEISMIC DATA

#### ***RMS Ratio***

The RMS ratio (RR) of two seismic datasets  $x$  and  $y$  is a commonly used measure of time-lapse repeatability. It is given by the following equation:

$$RR = \frac{RMS(x - y)}{\frac{1}{2}[RMS(x) + RMS(y)]} \quad (A-1)$$

where the RMS operator is defined as

$$RMS(x) = \sqrt{\frac{\sum_{i=1}^{i=n} (x_i^2)}{n}} \quad (A-2)$$

and  $n$  is the number of samples in  $x$ .

After normalization,

$$\bar{x} = \bar{y} = 0 \quad (A-3a)$$

$$\mathbf{s}_x = \mathbf{s}_y \quad (A-3b)$$

Therefore, since  $RMS(x) = \mathbf{s}_x$ , when  $\bar{x} = 0$ ,

$$RR = \frac{\mathbf{s}_p}{\frac{1}{2}[\mathbf{s}_x + \mathbf{s}_y]} = \frac{\mathbf{s}_p}{\mathbf{s}_x} \quad (A-4)$$

## Correlation Coefficient

The correlation between two surveys can also be expressed in terms of their total variance and noise variance (Burkhart et al., 2000):

$$r = \frac{\mathbf{s}_x^2 + \mathbf{s}_u^2}{\mathbf{s}_x^2} \quad (\text{A-5})$$

We know from equation (5) (if  $\sigma_u = \sigma_v$ ) that:

$$\mathbf{s}_u^2 = \frac{\mathbf{s}_p^2}{2} \quad (\text{A-6})$$

Therefore,

$$r = \frac{\mathbf{s}_x^2 - \frac{1}{2}\mathbf{s}_p^2}{\mathbf{s}_x^2} \quad (\text{A-7})$$

By combining equation (A-4) with (A-7), we can express the correlation coefficient of our normalized data in terms of their RMS ratio:

$$r = \frac{\mathbf{s}_x^2 - \frac{1}{2}(RR\mathbf{s}_x)^2}{\mathbf{s}_x^2} \quad (\text{A-8})$$

This expression simplifies to:

$$r = 1 - \frac{1}{2}RR^2 \quad (\text{A-9})$$

## **APPENDIX B**

# **SEISMOLOGICAL CHARACTERIZATION OF BULLWINKLE**

### ***Summary***

Four high quality 3-D seismic surveys acquired at Bullwinkle, Green Canyon 65, enable consistent interpretation of the Bullwinkle J-sands. Amplitude and structure maps of the sands exhibit many similarities, but also reveal changes that result from differences in the way that the data were acquired and processed. Comparison of a 1997 seismic survey with three pre-production surveys acquired in 1988 indicates some ways in which the reservoirs have changed over time.

This Appendix section discusses the acquisition, processing and imaging characteristics of the Bullwinkle seismic surveys with reference to a type dip-section running through the main hydrocarbon reservoir region at Bullwinkle. The method used for seismic time-to-depth conversion is outlined. Finally, amplitude and structure maps from each seismic survey are presented for the field's five major hydrocarbon reservoirs.

### ***Bullwinkle 3-D Seismic Survey Overview***

Four 3-D seismic surveys have been acquired over the Bullwinkle Field, Green Canyon Block 65. The first ("Bullwinkle") was obtained by Shell in 1984 (Figure B-1). It suffered from considerable navigational errors and poor lateral and vertical resolution, and is not considered in this analysis. Two orthogonal surveys were acquired prior to production in 1988, with the intention of investigating the effect of shooting direction in

the presence of complex salt geometry (O'Connell et al., 1993). These are referred to here as the 1988 E-W HF survey and the 1988 N-S LF survey (Table 2). The fourth survey was a regional non-proprietary survey acquired by in 1997 (the 1997 survey, Table 2), after over eight years of production from the field.

The 1988 E-W HF survey was acquired with a shooting direction of 110-290°. The bin size was 7.6 m in the inline direction and 45.7 m in the crossline direction. However, after data smashing (summation of adjacent traces) and migration, these became 15.2 m and 30.5 m respectively. The survey has 20-fold inline coverage and no multiplicity in the crossline direction. The main processing steps are shown in Table 3. The survey was later reprocessed and spectral normalization was performed in order to increase bandwidth. It has excellent vertical resolution and images the important events on the eastern edge of the salt body in Block 108 clearly.

The 1988 N-S LF survey was acquired and processed in a similar fashion, but with a shooting direction of 020-200°. Bin size after migration is 30.5 m inline, 22.9 m crossline. The 30.5 m inline bin size is equal to the crossline CMP spacing of the 1988 E-W HF survey, which assisted in the shooting direction comparison of the surveys. The 1988 N-S LF survey was also whitened. This version of the 1988 north-south survey is referred to as the 1988 N-S HF survey (Table 2). The 1988 N-S HF survey generally has excellent vertical resolution, but suffers from poor imaging where the Jsands dips steeply and perpendicularly to its acquisition direction (O'Connell et al., 1993).

The 1997 survey was shot in a north-south direction. The bin size was 12.5 m in the inline direction and 20 m in the crossline direction, with a nominal fold of 39. These dimensions were maintained in the final migrated dataset. Undershooting was also

performed to provide coverage underneath the Bullwinkle Platform. The processing sequence is summarized in Table 3.

*Offset.-* The 1997 and 1988 surveys were acquired with very different maximum offsets (6010 m and 3930 m, respectively). However, the offset tapering applied to the CDP gathers means that a much closer range of offsets are present at most depths in the different surveys after trace muting (Figure B-2). It is therefore expected that there will be no significant imaging differences between the surveys that result from amplitude variation with offset effects.

In the 1997 survey, offsets greater than the function shown in Figure B-2 were muted. Shell performed a more complex procedure to the 1988 surveys. A blanket offset taper was applied to all data that was recorded after the theoretical arrival time of a direct wave traveling through the water at 1370 m/s, resulting in the mute function shown in Figure B-2. Additionally, near offsets were muted using a different time-offset function. A weighting function is also applied on bin-by-bin basis such that greater offsets are given less weight. The goal of the weighting operation is to derive CMP gathers that can be accurately stacked by a non-weighted stacking algorithm (Jones, 2001). A stacking algorithm that weighted each sample by the inverse of the square root of the number of traces that contributed to the sample in question was used to stack the 1997 survey.

### ***Differences in Processing***

There are many acquisitional and processing differences between the 1988 surveys and the 1997 survey. For example, the 1997 survey has a smaller bin size and almost double the nominal fold of the 1988 surveys. A “Q Compensation Filter” was



applied to the 1997 survey, in addition to both prestack and poststack predictive deconvolution following source signature deconvolution. The 1988 data were migrated prestack using a two-pass migration algorithm, which approximates a 3-D prestack Kirchhoff Migration (Gardner et al., 1986). The 1997 data were migrated using a post-stack one-pass 3-D phase-shift migration that requires interval velocities rather than the RMS velocities used in the 1988 survey migrations. However, whilst these factors may be important in a time-lapse analysis, the processing differences that have the most impact on the interpretability of the data are the running summation and spectral whitening procedures performed on the 1988 surveys (Table 3).

### ***Integration and Phase***

A prestack trace-by-trace running summation was performed on the 1988 survey data, whilst the 1997 survey remained a zero-phase reflection coefficient dataset. Running summation is the time-series equivalent of integrating continuous (analogue) data (Deshpande et al., 1997), If there are more positive or more negative reflection coefficients in a particular region, then a “drift” will be introduced into the data. This is removed by the attenuation of very low frequencies.

Integrating a time series is mathematically equivalent to rotating its phase by  $-90^\circ$  and attenuating frequencies at rate of 6dB/octave, since

$$F \left[ \int_{-\infty}^{\infty} f(x) dx \right] = \frac{F(\mathbf{w})}{j\mathbf{w}} + \mathbf{p}F(0)\mathbf{d}(\mathbf{w}) \quad (\text{B-1})$$

where  $F$  denotes the Fourier Transform,  $f(x)$  is the time-domain representation of a time series,  $F(\mathbf{w})$  is the frequency domain representation of the time series,  $j$  is the square root

of  $-1$ ,  $\omega$  is angular frequency, and  $\mathbf{p}F(0)\mathbf{d}(\omega)$  is an additive term to account for the possibility of a DC component (drift) in the integral (Oppenheim, 1999).

Shell's method of performing the running summation is usually carried out in the frequency domain by applying a  $-90^\circ$  phase-shift combined with the frequency ramp of  $-6$  dB/octave (Jones, 2001). A ramp of  $-3$  dB/octave is often chosen if greater bandwidth is desired in the integrated data. If the seismic dataset was initially zero-phase, then running summation results in data that has an embedded wavelet with phase of approximately  $-90^\circ$ .

Above tuning thickness, in a normal polarity dataset, the top of a (lower impedance) sand will correspond to the zero crossing between a peak and a larger trough. The base of the sand corresponds to the zero crossing between the trough and the subsequent peak (Figure B-3a). In thinner sands, the "loop thickness" approximates the sand thickness (Figure B-3b). Integrated data is therefore similar to an impedance volume.

## ***Frequency***

The high frequency 1988 surveys have the broadest power spectra, with significant frequencies present up to 60 Hz (Figure B-4). The spectral balancing is performed as a post-stack process by boosting higher frequencies where there is still a good signal to noise ratio (Jones, 2001). The 1988 N-S LF survey has the narrowest frequency spectrum, with a dominant frequency range of 8-15 Hz. The 1997 survey has intermediate frequency content. If 6dB lower than the peak frequency is considered as the limit of significant frequency, then this point corresponds to approximately 50 Hz in

the high frequency 1988 surveys, 22 Hz in the original 1988 N-S LF survey, and 35 Hz in the 1997 survey.

This variation in frequency has an important role in determining the vertical resolution in the seismic surveys. It has been observed that it is typically possible to resolve layers that are greater than one quarter of the dominant wavelength ( $I$ ) in the survey (Yilmaz, 1987). Table B-2 was constructed using the following relationships:

$$I = \frac{v_p}{n} \quad (\text{B-2a})$$

and

$$\text{Min Thickness} \approx \frac{I}{4} \quad (\text{B-2b})$$

*Min Thickness* is the minimum resolvable layer thickness (m),  $v_p$  is the acoustic velocity of the layer (assumed to be 2000 m/s), and  $n$  is the dominant frequency in the survey.

Approximately one third of the vertical thickness of the thinnest resolvable bed in the 1988 N-S LF survey (51 m) can be resolved in the 1988 high frequency survey surveys (17 m) (Table B-2). It is essential to consider this information is when interpreting the datasets.

Type dip-sections from the seismic surveys (Figures B-6-B-10) clearly illustrate the differences in stratigraphic resolution and also in the phase of the data. The polarity reversals observed in the J3 and J4 seismic amplitude maps (Figures B-12-B-18) are also evident.

## ***Depth Conversion***

Since seismic data is recorded and usually processed in time rather than depth, it was necessary to perform a time to depth conversion in order for the horizon structure maps to be geologically useful. Firstly, an approximate depth conversion was applied for each interpreted event using a time-depth table for a single well in the field. Well 109-1 was used for this purpose because it is a non-deviated hole and a check-shot survey was performed at the well. The time-depth table relates the true-vertical depth in the well to the observed p-wave travel time down to that point. However, this time-depth table is only accurate at the 109-1 location so there will be errors in the depth of the horizon elsewhere.

These errors can be calculated at location of the other wells in the field. The approximate depth horizons were manipulated into a regularly sampled grid, and then a back interpolation algorithm was used to calculate the value of the depth grid ( $H$ ) at each well location. This was then subtracted from the actual depth of the horizon from the well logs ( $W$ ), in order to find the error at this point in the depth grid ( $E$ ) (Figure B-11).

The calculated errors at the well location were then gridded in to a region larger than the input horizon. A corrected horizon depth was then produced by subtracting this error grid from the original approximate depth grid. The procedure was very successful in regions of close well control and errors in the final depth grid were typically less than 1 m at the well locations.

## ***Amplitude and Structure Maps***

Seismic amplitude and structure maps were produced by interpreting the five major reservoir sands in each of the Bullwinkle 3-D surveys (Figures B-12-B-30). These are early Nebraskan interconnected channel and sheet turbidite sands and are collectively known as the “J-sands”. The I10 and Rocky sands are included in this description because they are geologically very similar, and are also in pressure communication with the J1-J4 sands.

The amplitude maps were constructed by attempting to extract the greatest negative amplitude of the trough corresponding to the top of each sand. This was also done in the integrated surveys in order to make the most meaningful amplitude maps, despite the fact that the interpreted events would lie beneath the sand tops (Figure B-3). The maps are arranged in stratigraphic order and a brief overview of each of the sands is also included.

***J4 Sand.***- The J4 is a ponded sheet turbidite sheet sand that lies on the western flank of the Bullwinkle minibasin. It is typically 6-20 m thick. The present day structural high point of the sand is adjacent to the western salt flank of the basin, with the uppermost 300 m being oil-filled. The original oil-water contact is seismically visible at approximately 3610 m (11 855 ft) sub-sea depth (Figures B-12-B-14).

The J4 sand lies very close to the J3 sand above, making the two events difficult to distinguish seismically. This is especially true in the case of the 1988 N-S LF survey, which does not have sufficient resolution to distinguish the sands. For this reason, a separate 1988 N-S LF amplitude and structure map is not presented. This also means that

the J4 event experiences the same polarity reversal that affects the J3 sand in all the surveys, as discussed in the following section.

The observable extent of the sand in the different surveys is affected by their vertical resolution. Therefore, it cannot be traced as far in the 1997 survey as it can in the 1988 E-W HF survey. Pressure measurements show that the sand around well 108-2 is stratigraphically disconnected from the rest of the reservoir. This is thought to be a slump related feature, and is also evident in the J3 and J2 sands. However, this cannot be observed seismically in the J4 event. The southern region of the J4 sand is offset by two normal faults.

**J3 Sand.-** The J3 sand is geologically very similar to the J3 event, and is also a ponded turbidite event (*Flemings et al, 2001*). Its true vertical thickness generally ranges from 6-15 m. The original oil-water contact is seismically visible at approximately 3610 m (11 850 ft) sub-sea depth (Figures B-15-B-18). The J3 has a gas cap and an original gas-oil contact was found in well A-35 at a depth of 3503 m. This has remained fairly constant over time, and was estimated by Shell to lie at 3497 m in 1999.

The J3 is separated from the J2 event by a thin succession of debris flow deposits and shales. The imaging of the J3 sand in all three surveys is dramatically affected by tuning with the J2. This is particularly noticeable just beneath the J3 oil-water contact and above the J2 oil-water contact. Here, the J3 event is dominated by a large amplitude J2 post-cursor (Figures B-6-B-10), and is represented by negative amplitudes in all three surveys (Figures B-15-B18).

There is a flow barrier separating the 108-2 region can be observed in the high frequency surveys. The barrier is also confirmed by pressure measurements. The normal

faults observed in the J4 event also offset the J3 sand and the southernmost fault may delineate the sand edge at this point.

**J2 Sand.-** The J2 sand is the major hydrocarbon producer at Bullwinkle. It is laterally extensive in the northern and western section of the minibasin and is typically 10–30 m thick. It appears that the J2 sand extends across the southern extremity of the basin, which may provide a channel for water influx (Figures B-19-B-22).

The sand is well imaged in the seismic surveys, particularly when it is hydrocarbon filled. However, this is not the case when the sand thins in the region of well A-11-BP, where slumping may have occurred. This poor imaging is due to destructive interference with the thick J1 sand, which lies a short distance above. Conversely, constructive interference occurs, particularly in the 1988 E-W HF survey, where the J1 and J2 events become very close at the southern edge of the J1 sand (near well 109-1). The 1988 surveys exhibit a clear seismic OOWC at 3785 m (12 415 ft). Production data and PNC logs show that this moved up to around 3535 m in 1997, and this is imaged to some extent by the 1997 survey (Figure B-22).

The J2 RA and RB reservoirs are separated by a seismic discontinuity, which provides a barrier to fluid flow. An original gas-oil contact was discovered in the RA reservoir at 3718 m (12 197 ft) in well 65-1. Another discontinuity is visible in the 1988 N-S HF survey approximately 300 m to the east of well A-4-BP, and a small fault appears to exist between wells A-4-BP and A-38-ST. However, it is possible that these may be due to imaging problems close to the salt body to the north.

The 108-2 flow barrier is observable in all the seismic surveys. An oil-water contact was found in this up-dip well, which provides further evidence for the existence for this feature. The normal faults in the southern region are thought to have J2 sand-on-sand contacts. If these are not sealing, then it is possible that the original oil-water contact continues through this region. The region of large amplitude in the RB reservoir appears to terminate to the south against a small fault that does not displace the J2 horizon in the seismic surveys. It does, however, offset the J4 event below, and its path can be traced by a reduction in horizon amplitude. It is possible that this feature defines the edge of the J2 reservoir, and not the larger fault further to the south.

**J1 Sand.-** The J1 sand contains the second greatest volume of hydrocarbons in the Bullwinkle Field, after the J2 event. It is more channelized than the lower J-sands and is truncated by the Rocky event towards the southeast of the basin. A large region of the J1 sand appears to have been eroded away after deposition (Figures B-23-B-26).

A thin shale layer separates the J1 and J2 sands, which may decline to zero thickness in the region of well 109-1. This would allow these sands to merge in this location and allow pressure communication between them. The close proximity of the J1 and J2 sands means that they are rarely imaged separately in the lower frequency 1988 N-S LF and 1997 seismic surveys, but instead form a seismic doublet (Figures B-9 and B-10).

A seismic original oil-water contact can is visible in all the surveys, which corresponds to a depth of approximately 3755 m (12 320 ft). Production data suggest that



the OWC had risen to about 3475m when the 1997 survey was acquired, but this is not easily visible in the seismic.

The same seismic discontinuities that separate the J2 RA and RB reservoirs are also present in the J1 sand. The J1-RA reservoir had a seismically estimated original gas-oil contact at 3760 m (12 335 ft).

***I10 and Rocky sands.***- The I10 and Rocky sands are the youngest of the major hydrocarbon reservoirs in the Bullwinkle Field. They form a largely continuous turbidite sand body (Kikani and Smith, 1996) that conformably and unconformably overlies the J1 sand on the northwest (Bullwinkle) side of the basin. However, the I10 sand can be seen to also overlie the Rocky event in the southern extremity of the basin, indicating that the two sands were not deposited by the same event.

The I10 reservoir is oil-filled and clearly imaged in each of the surveys (Figures B-27-B-30). Pressure measurements show that the reservoir is compartmentalized into at least two sections. The largest of these is penetrated by well A-36, which contains 6 m of net oil-sand. There is a clear seismic oil-water contact at depth of approximately 3815 m (12 515 ft). The other major compartment is located up-dip and centered on well A-32-BP, which penetrates 12 m of oil-filled I10 sand.

The Rocky reservoir is characterized by very high seismic amplitudes (Figures B-27-B-30). It lies at the southeastern corner of the mini-basin and is fault bounded. It was originally oil filled, with an estimated original oil-water contact at 3705 m (12 150 ft). However, the reservoir pressure decreased below the bubble-point pressure in response to Bullwinkle production, which lead to the formation of a gas cap. The gas-oil contact is

not observable on the 1997 survey, but gas is presently being produced from well SOI-110-1.

## ***Conclusion***

The Bullwinkle 3-D seismic datasets have enabled accurate high quality J-sand amplitude and structure maps to be constructed. This has been facilitated by the excellent well control in the field, which made accurate depth conversion possible. The resulting maps have been vital inputs for a reservoir simulation model, and have aided a time-lapse analysis of the Bullwinkle J-sand reservoirs.

The reservoir sands can be interpreted quite consistently in each of the seismic surveys, despite considerable differences in their acquisition and processing. However, some differences exist, even between the pre-production 1988 surveys, that are a function of frequency content and acquisition direction.

The 1988 E-W HF and 1988 N-S HF surveys are very high frequency datasets, which permit the separate interpretation of all of J-sand reservoirs. This is not the case with the 1988 N-S LF survey, and pushes the limit of the 1997 survey resolution. The 1988 E-W HF survey arguably provides the clearest imaging of the J-sands due to its acquisition direction and smaller bin size in the downdip direction.

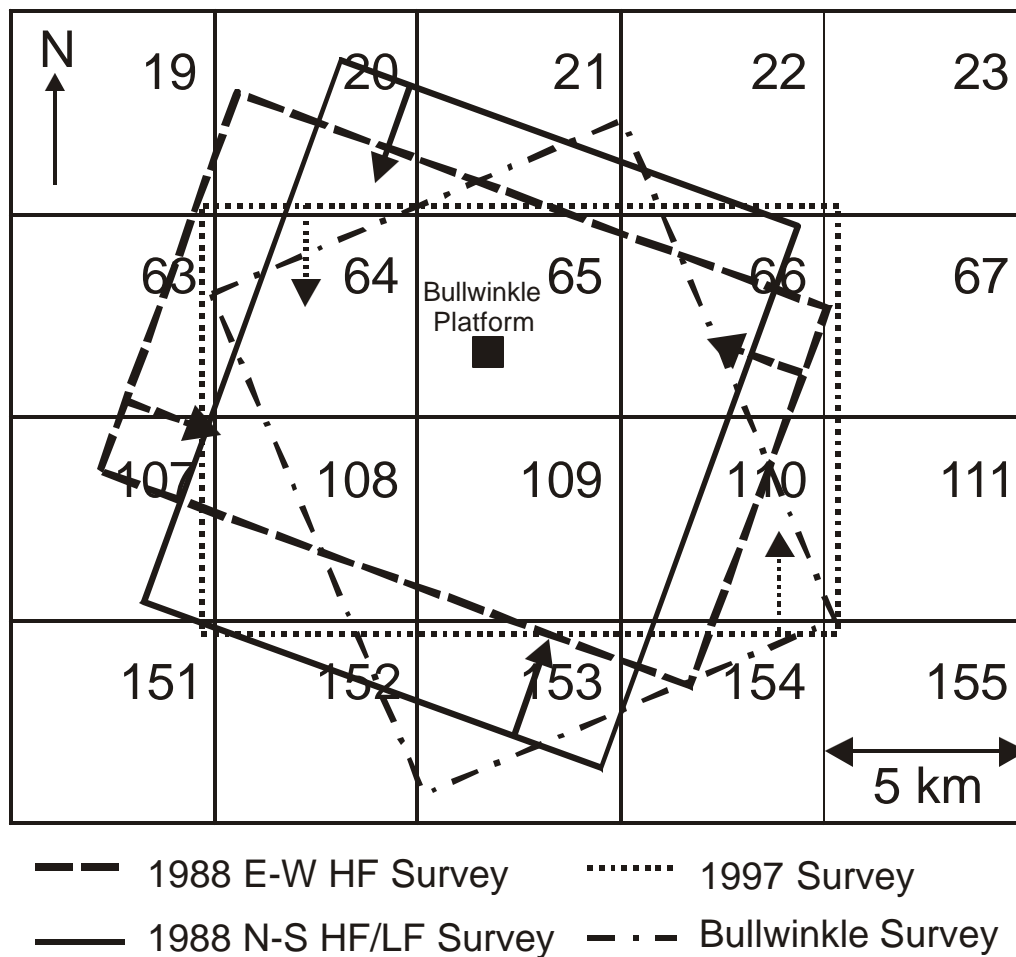


**Figure B-1:** Green Canyon Basemap showing the location of the 3-D surveys acquired over Bullwinkle. Arrows represent the survey acquisition direction.

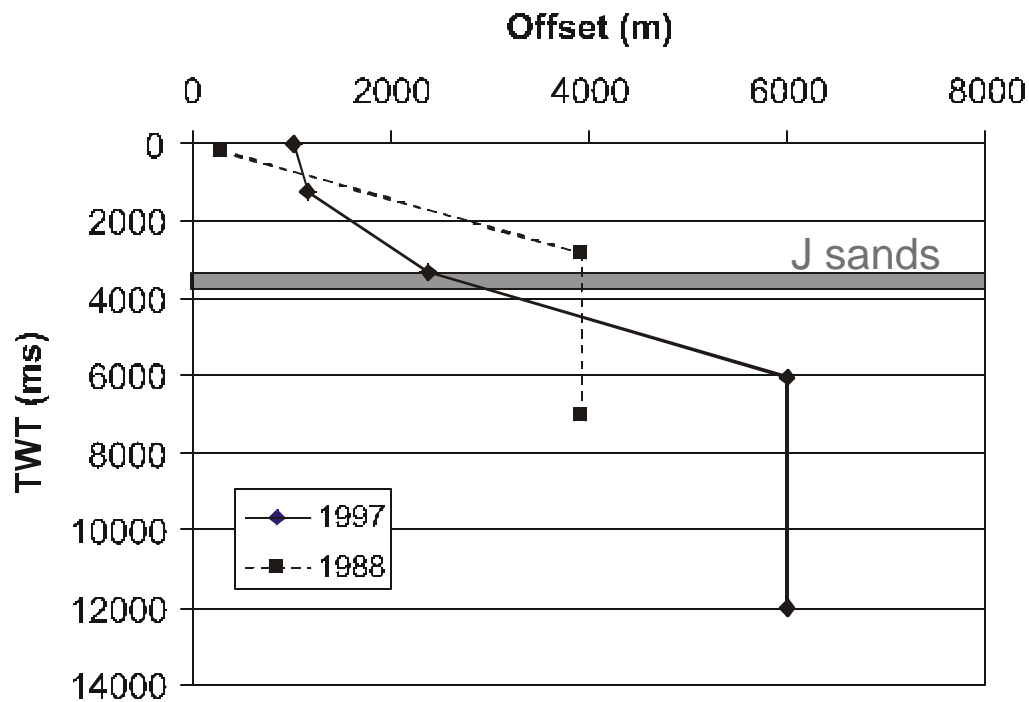


**Figure B-2:** Offset tapering functions for the 1997 and 1988 surveys. All offsets greater than the lines plotted are completely muted. An offset weighting procedure and near offset mute is also performed on the 1988 data.

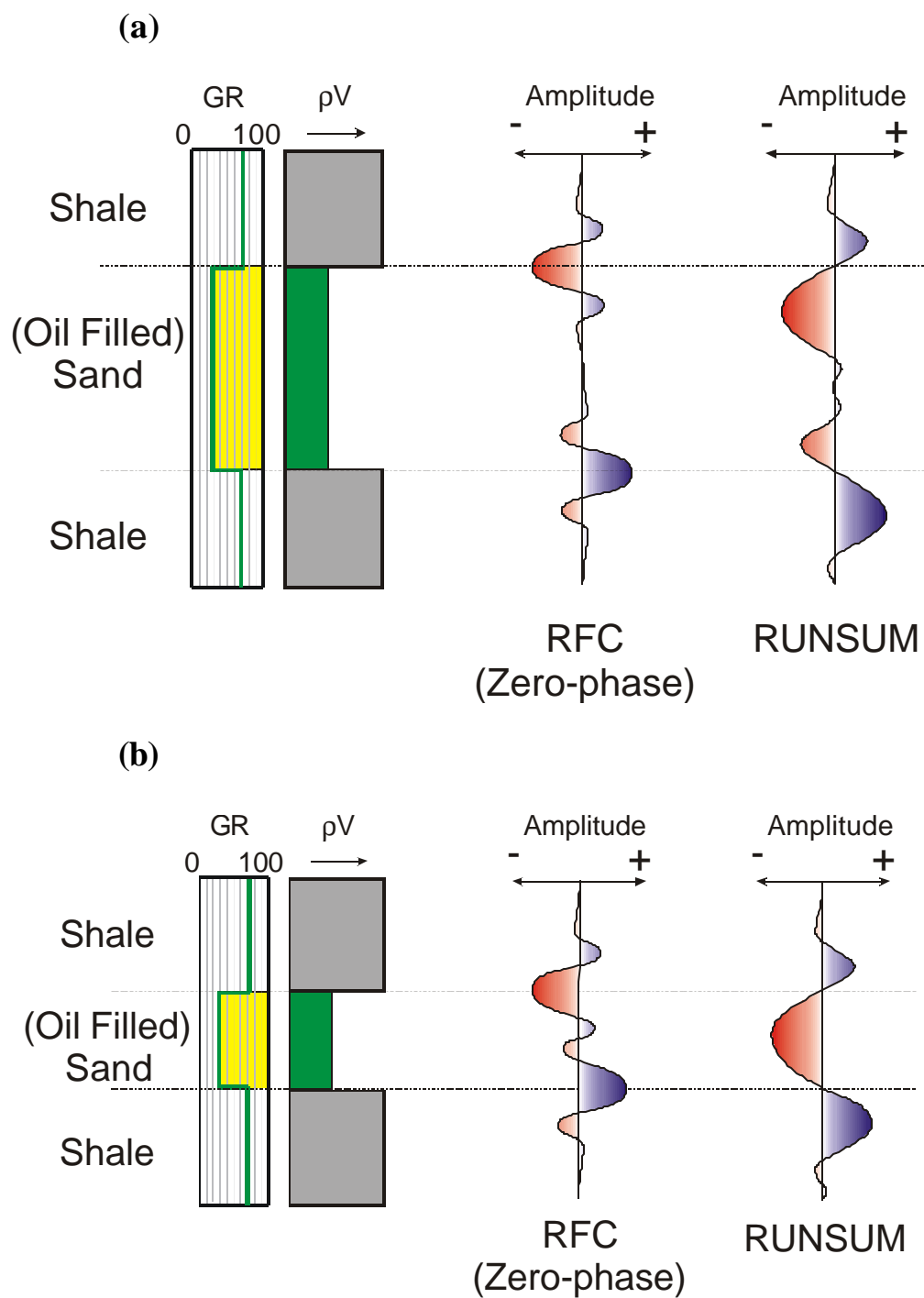


**Figure B-3:** Theoretical zero-phase reflection coefficient and integrated traces illustrating the signature of the top and base of (a) a thick oil-filled sand body, and (b) a thin oil-filled sand body. Red represents negative amplitude and blue corresponds to positive amplitudes.

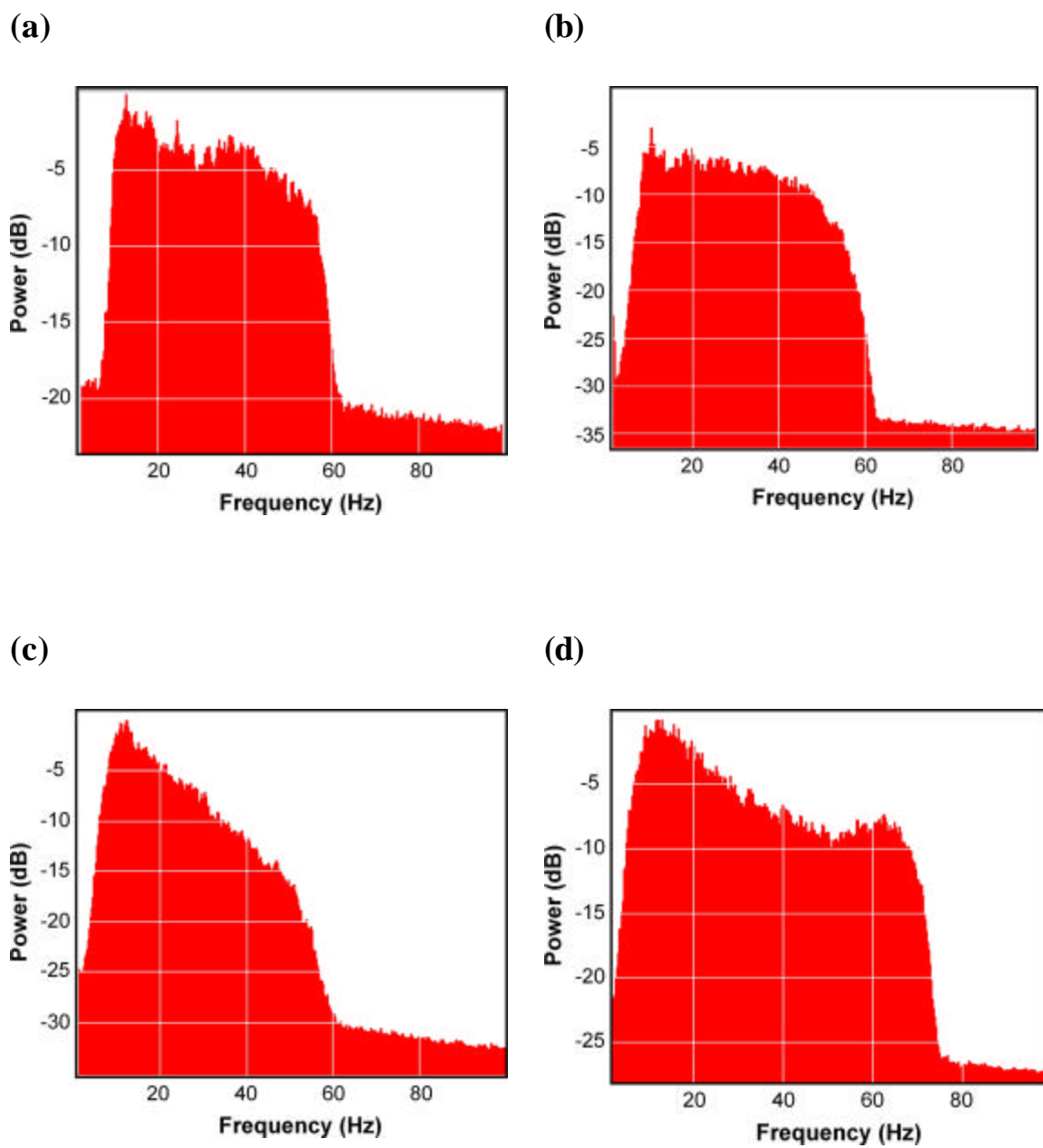


**Figure B-4:** Power spectra of (a) the 1988 E-W HF survey, (b) the 1988 N-S HF survey, (c) the 1988 N-S LF survey, and (d) the 1997 survey. The derivation region was restricted to the upper 7 s the surveys, since the 1988 surveys only extend down to 7 s.

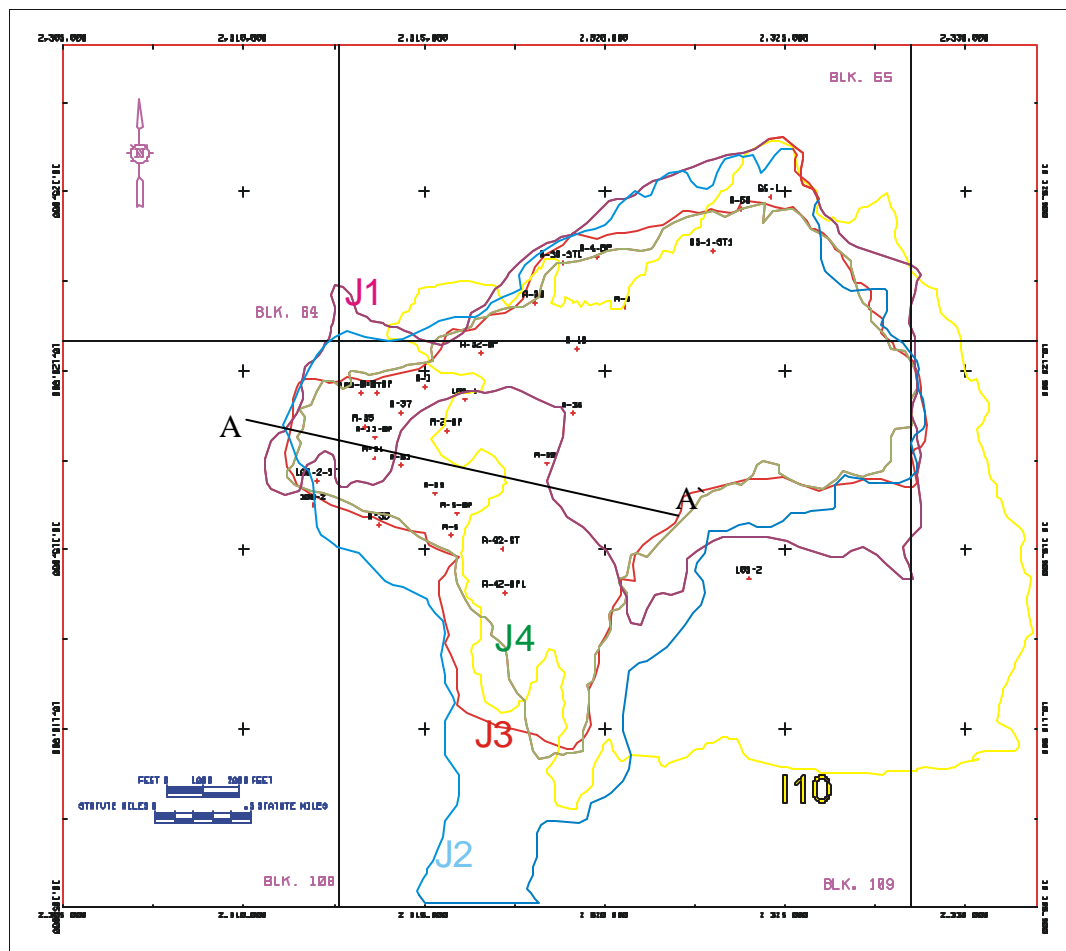


**Figure B-5:** Basemap showing the bounding polygons of the major horizons interpreted in the 1988 E-W HF survey. The locations of the Bullwinkle wells in the J2 Horizon are also included for reference. The line A-A` corresponds to the seismic sections in Figures B-6-B-10.

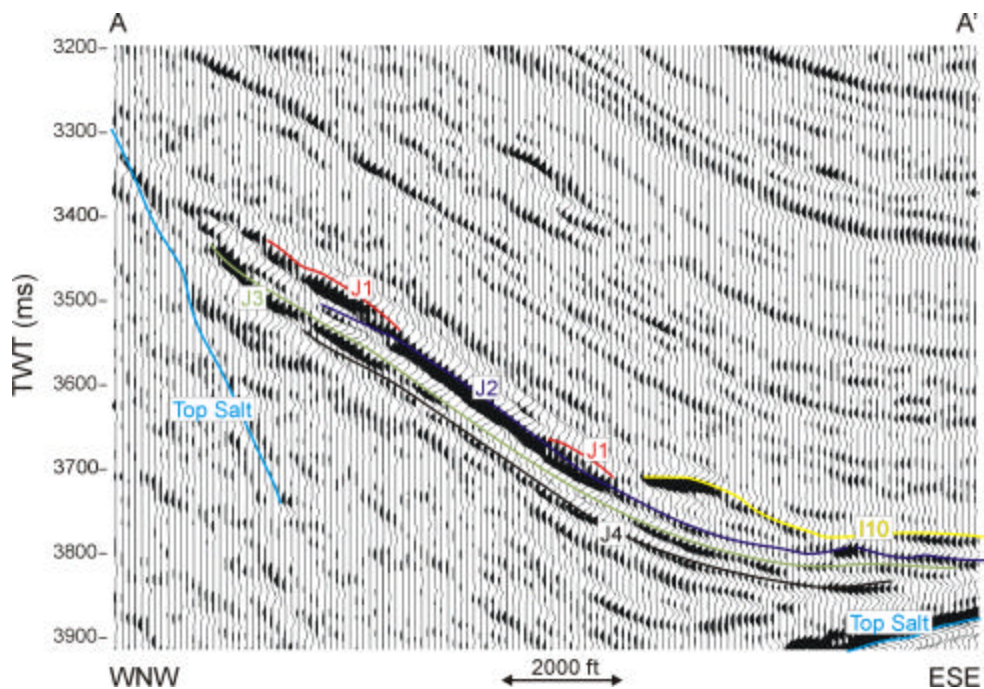


**Figure B-6:** Dip-section along A-A' from the 1988 E-W HF survey, displayed as negative-fill wiggle-traces. The tops of the major hydrocarbon sands are interpreted, which typically correspond to the zero crossing from positive to negative amplitude. The top of the salt is a “hard” event and therefore has opposite polarity.



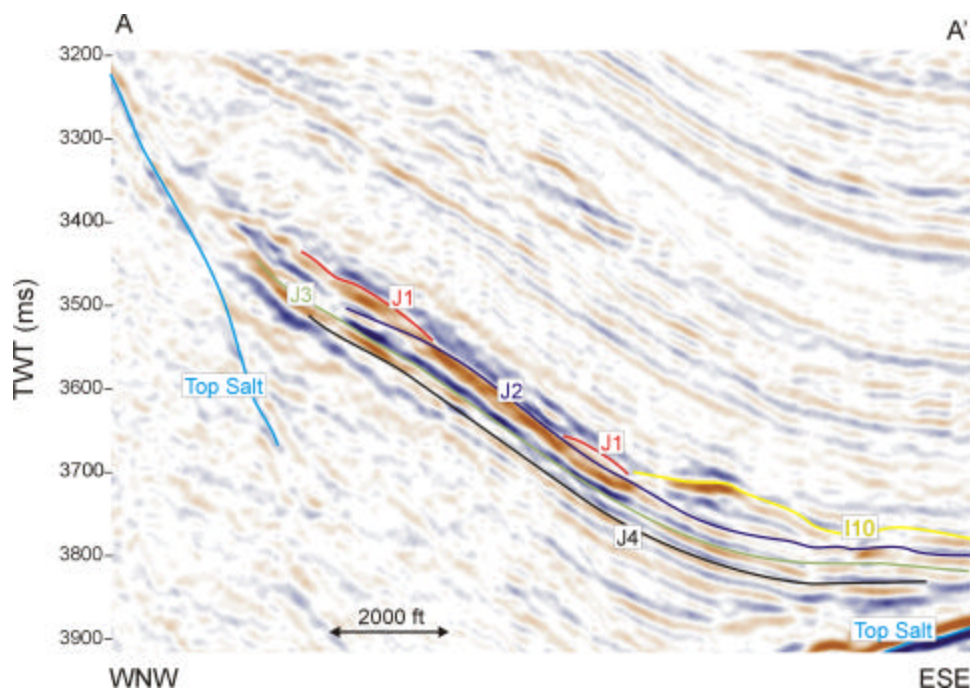


**Figure B-7:** Dip-section along A-A' from the 1988 E-W HF survey, shown in variable density mode. Red colors represent negative amplitude, whilst blue colors are positive amplitudes. Note the polarity reversal of the J3 and J4 sands underneath the thick J2 event in the center of the section.

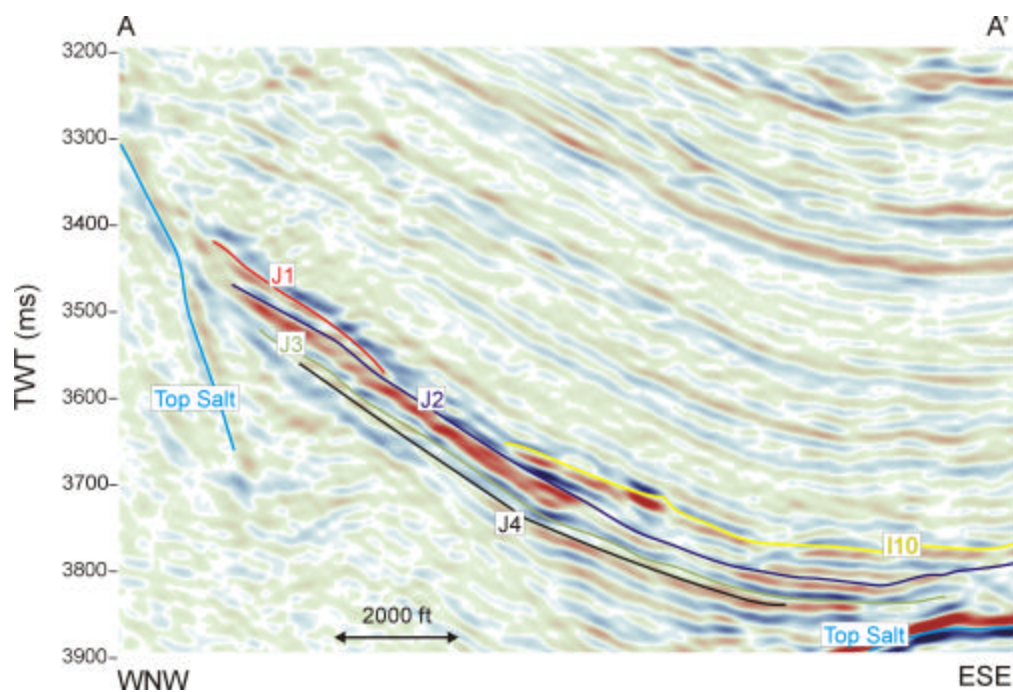


**Figure B-8:** Variable density dip-section along A-A' from the 1988 N-S HF survey. The image of the J-sand package is somewhat disrupted by stair-step noises and migration problems.

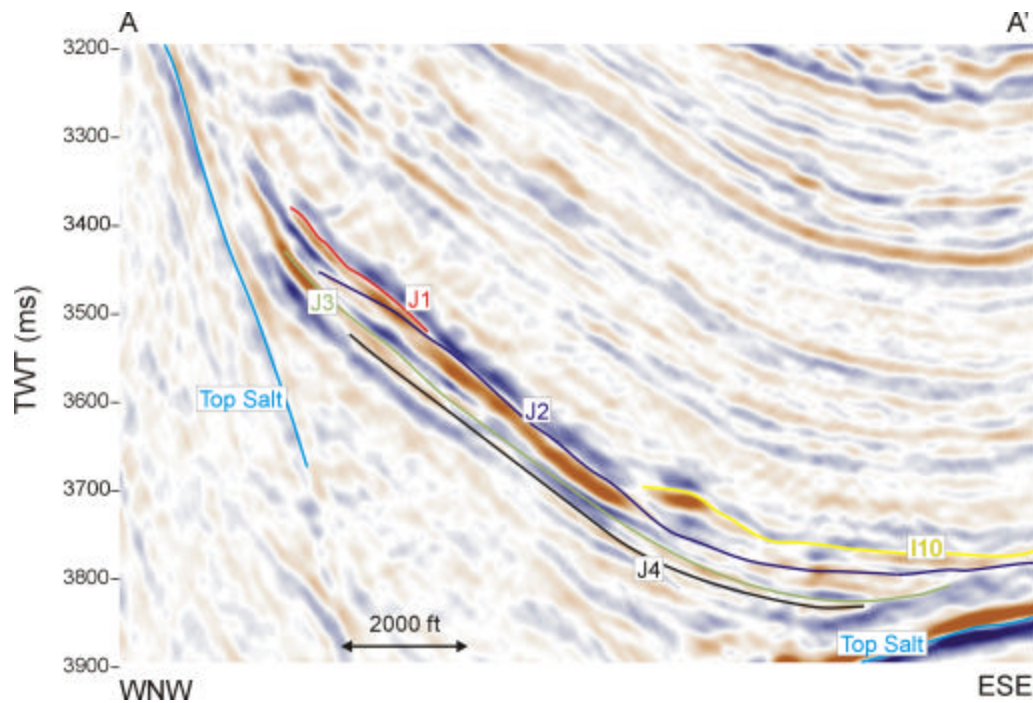


**Figure B-9:** Variable density dip-section along AA' from the 1988 N-S LF survey. Note the much lower frequency content of the data, and the poorer vertical resolution of the sands.

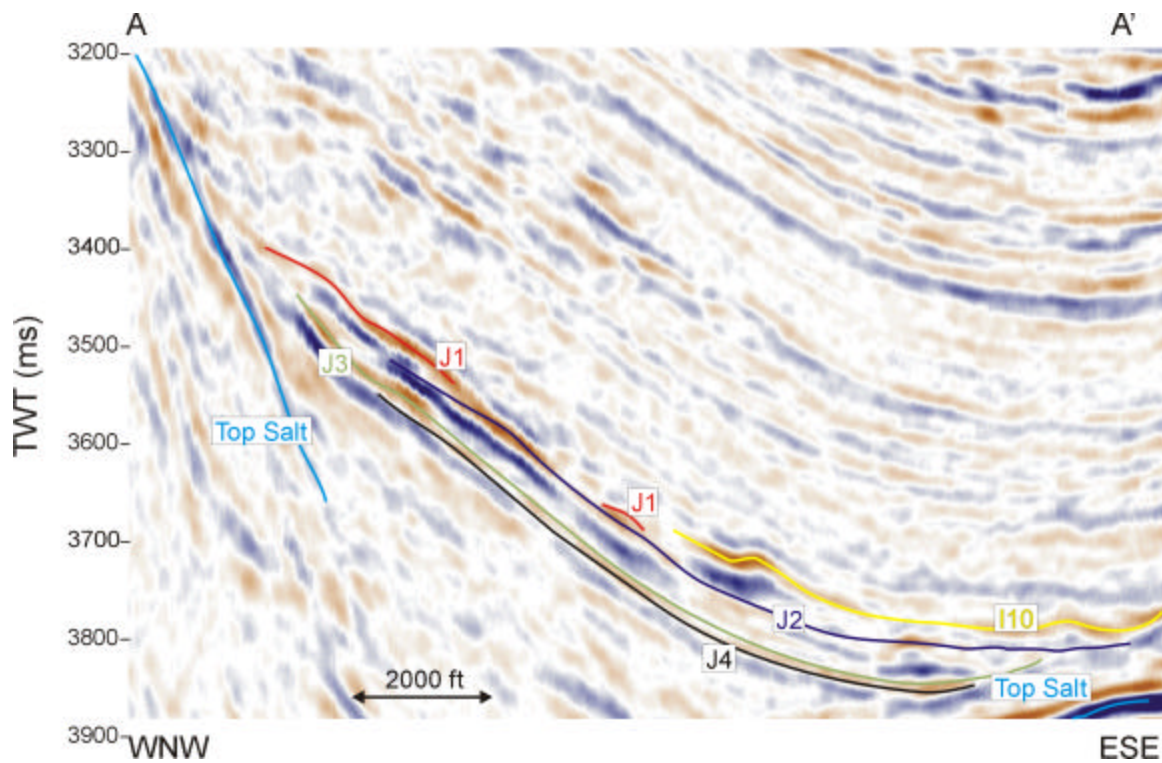


**Figure B-10:** Variable density dip-section along A-A' from the 1997 survey (arbitrary line). Note that this survey is not integrated; so sand tops are typically imaged as the center of seismic troughs.

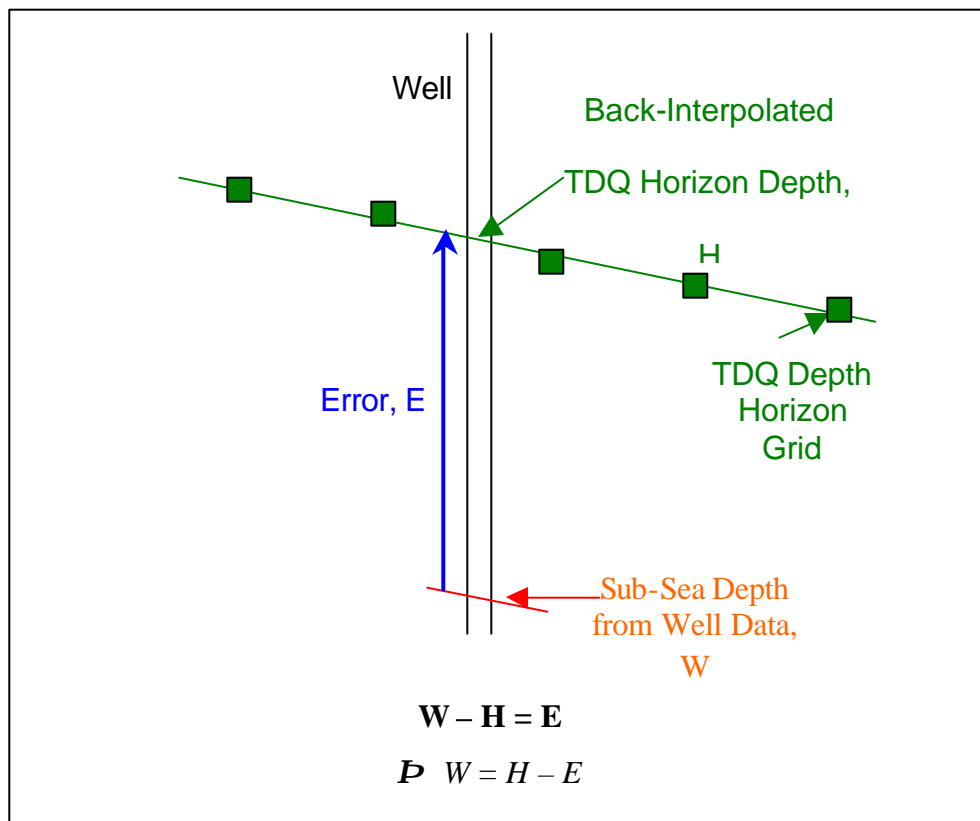


**Figure B-11:** Diagram illustrating the theory behind the back-interpolation method of depth error estimation.

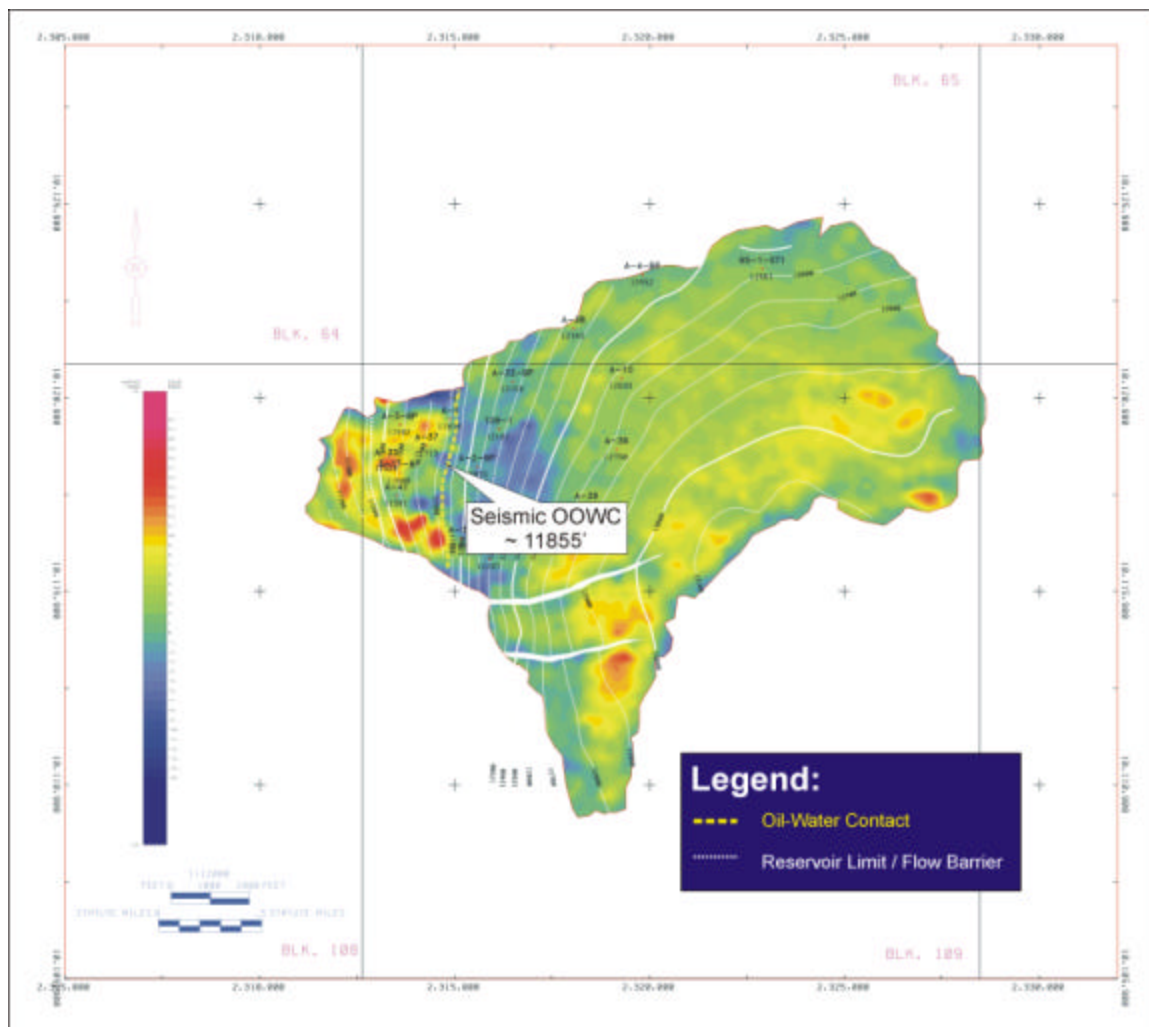


**Figure B-12:** 1988 E-W HF J4 amplitude and structure map showing well penetrations and original fluid contacts. Bright colors represent strongly negative amplitudes.



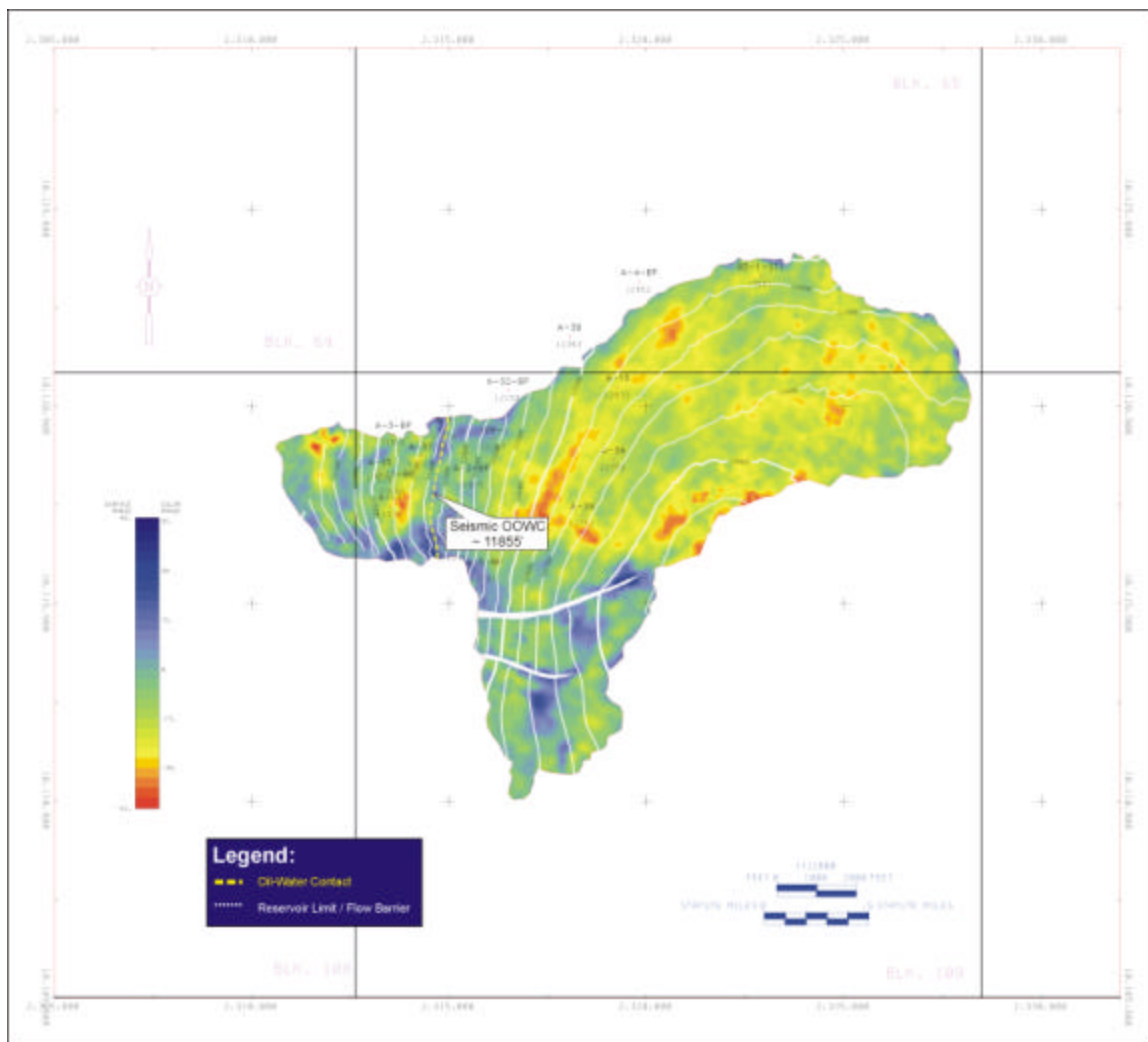


**Figure B-13:** 1988 N-S HF J4 amplitude and structure map showing well penetrations and original fluid contacts. Bright colors represent strongly negative amplitudes.

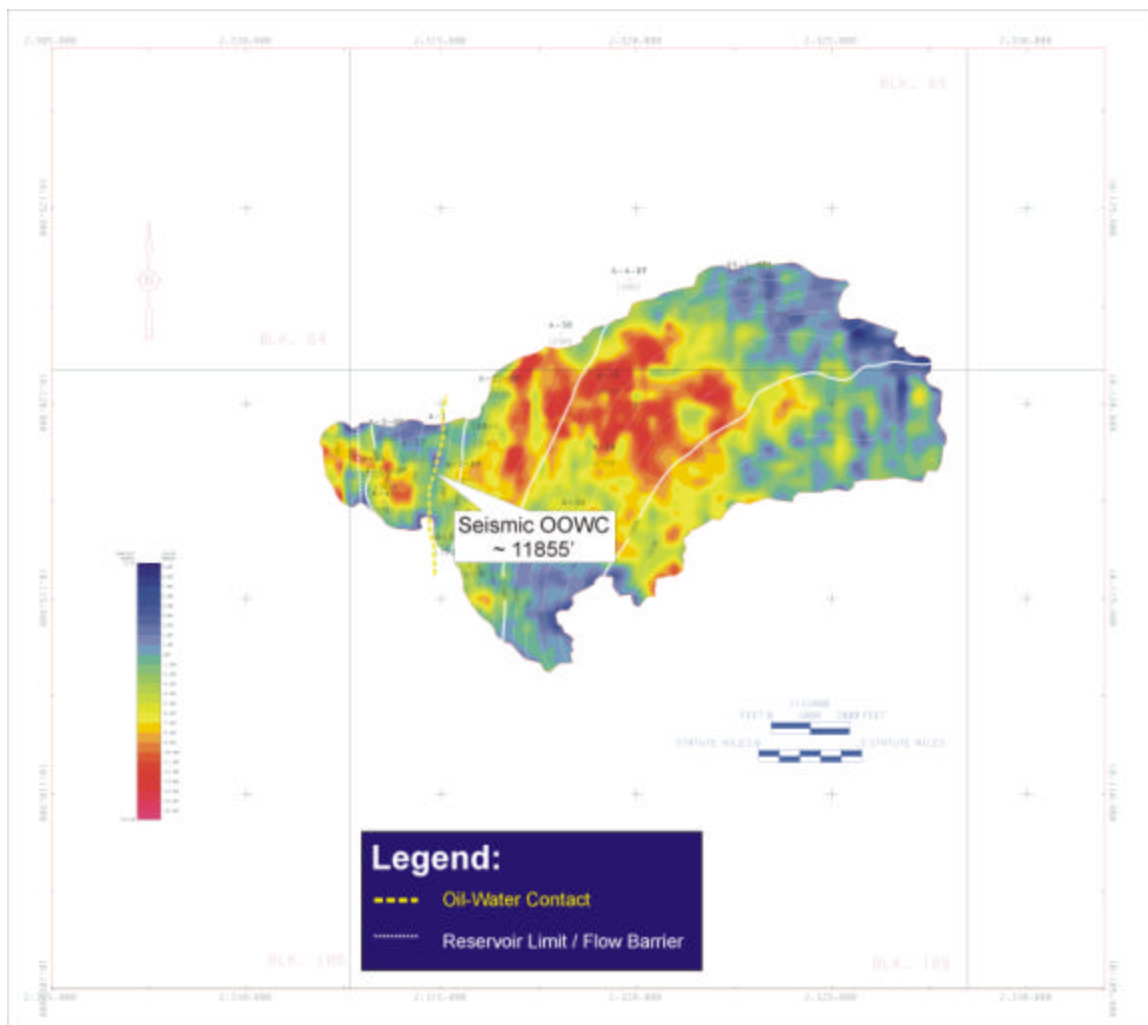


**Figure B-14:** 1997 J4 amplitude and structure map showing well penetrations and original fluid contacts. Bright colors represent strongly negative amplitudes.



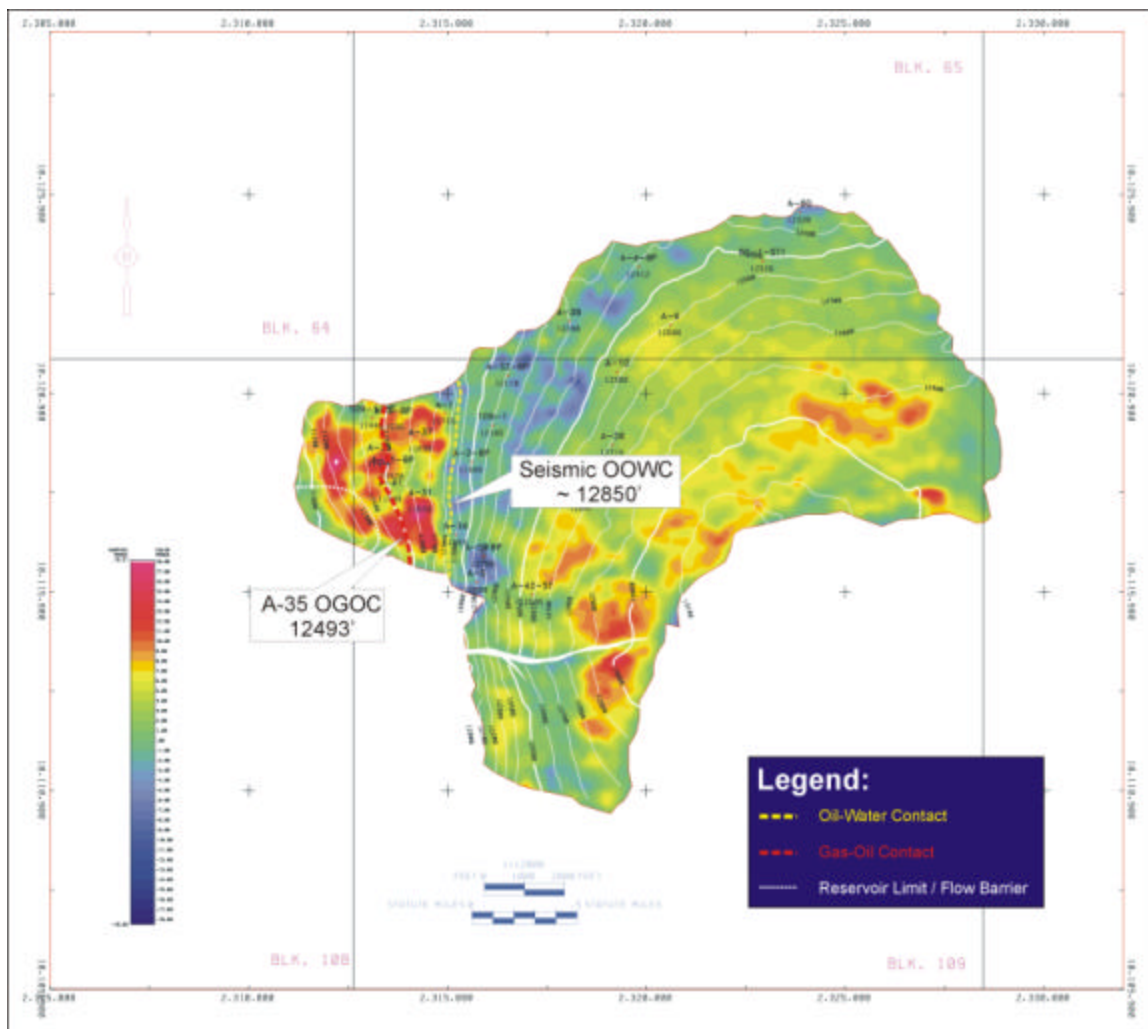


**Figure B-15:** 1988 E-W HF J3 amplitude and structure map showing well penetrations and original fluid contacts. Bright colors represent strongly negative amplitudes.

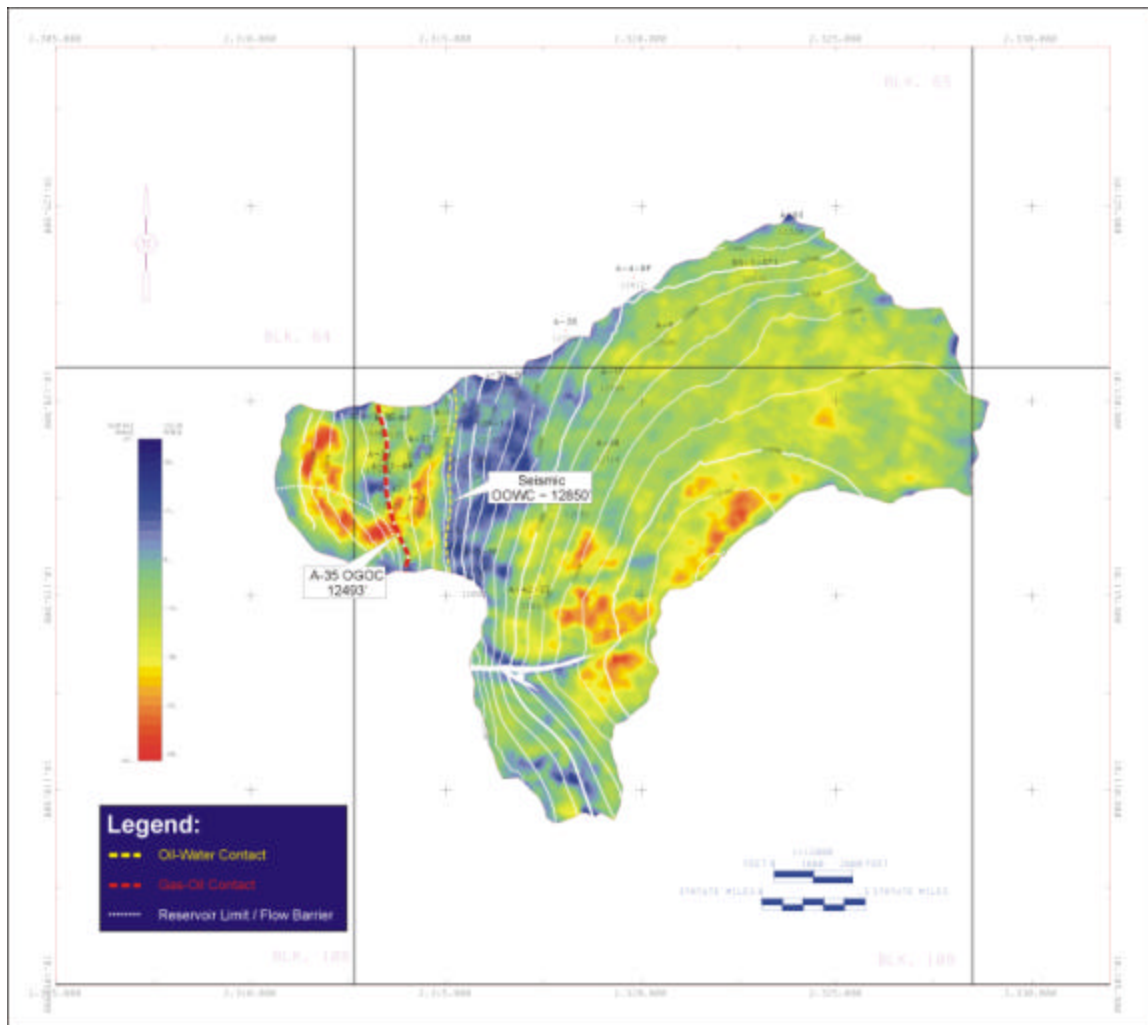


**Figure B-16:** 1988 N-S HF J3 amplitude and structure map showing well penetrations and original fluid contacts. Bright colors represent strongly negative amplitudes.

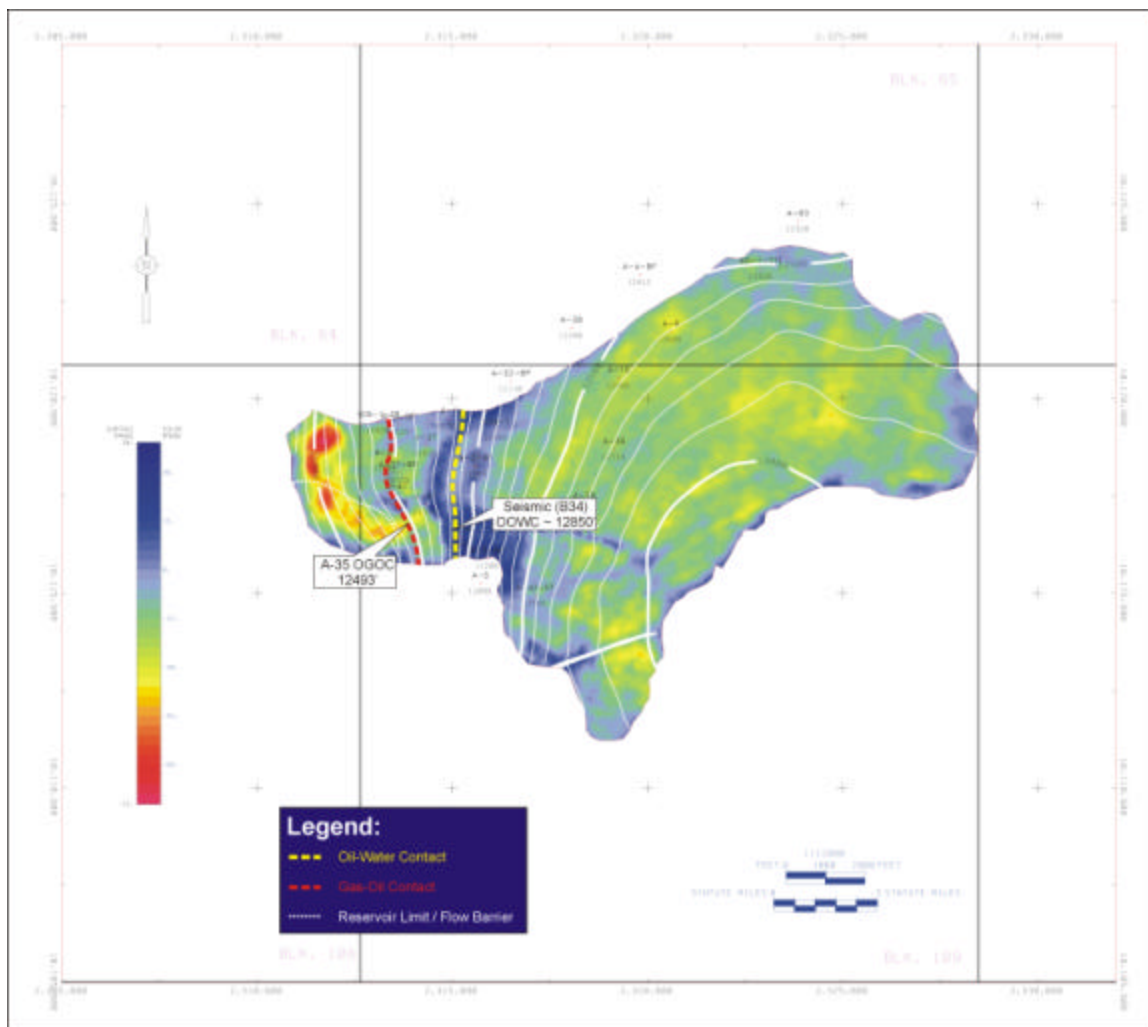


**Figure B-17:** 1988 N-S LF J3 amplitude and structure map showing well penetrations and original fluid contacts. Bright colors represent strongly negative amplitudes.

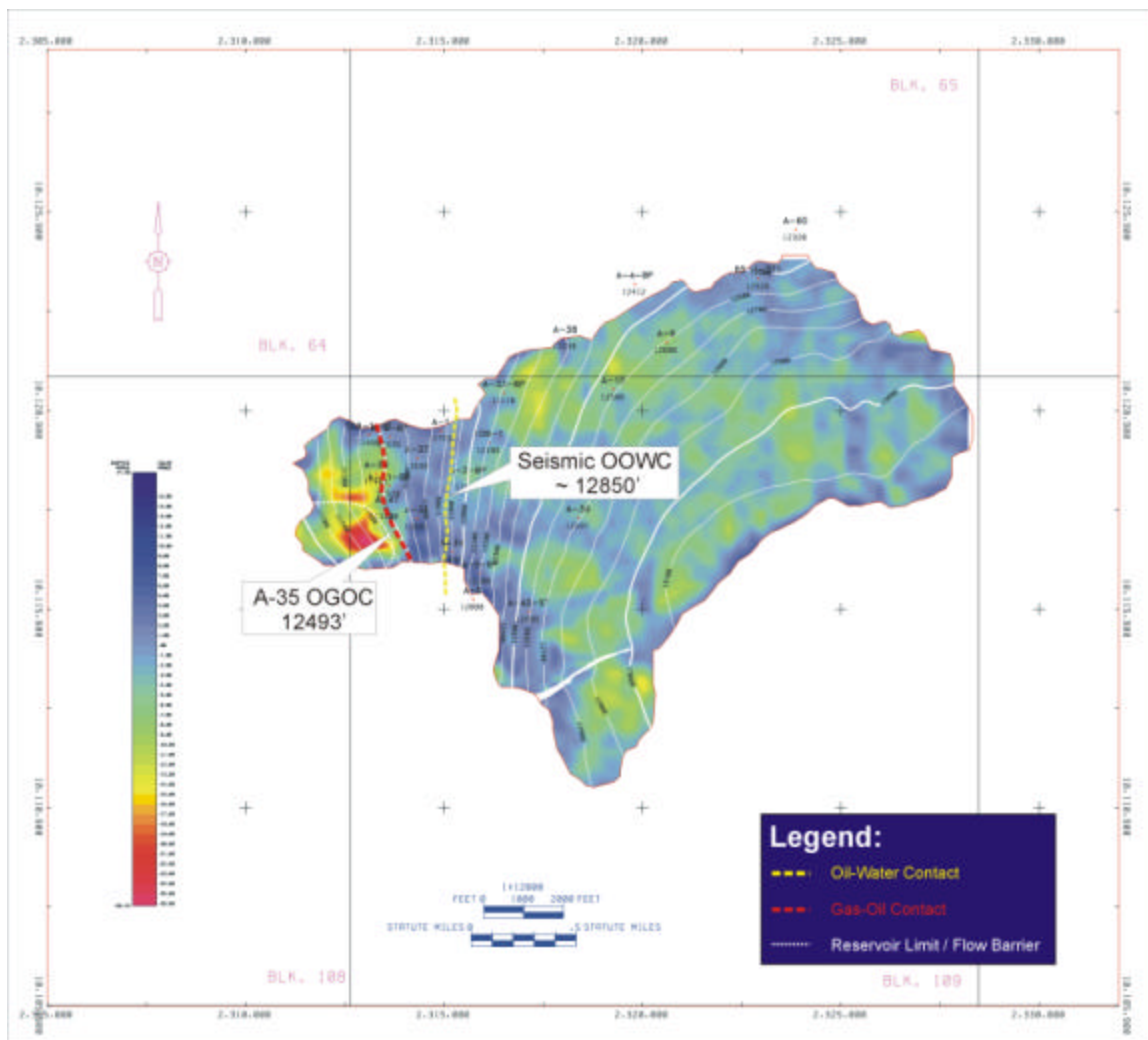


**Figure B-18:** 1997 J3 amplitude and structure map showing well penetrations and original fluid contacts. Bright colors represent strongly negative amplitudes.

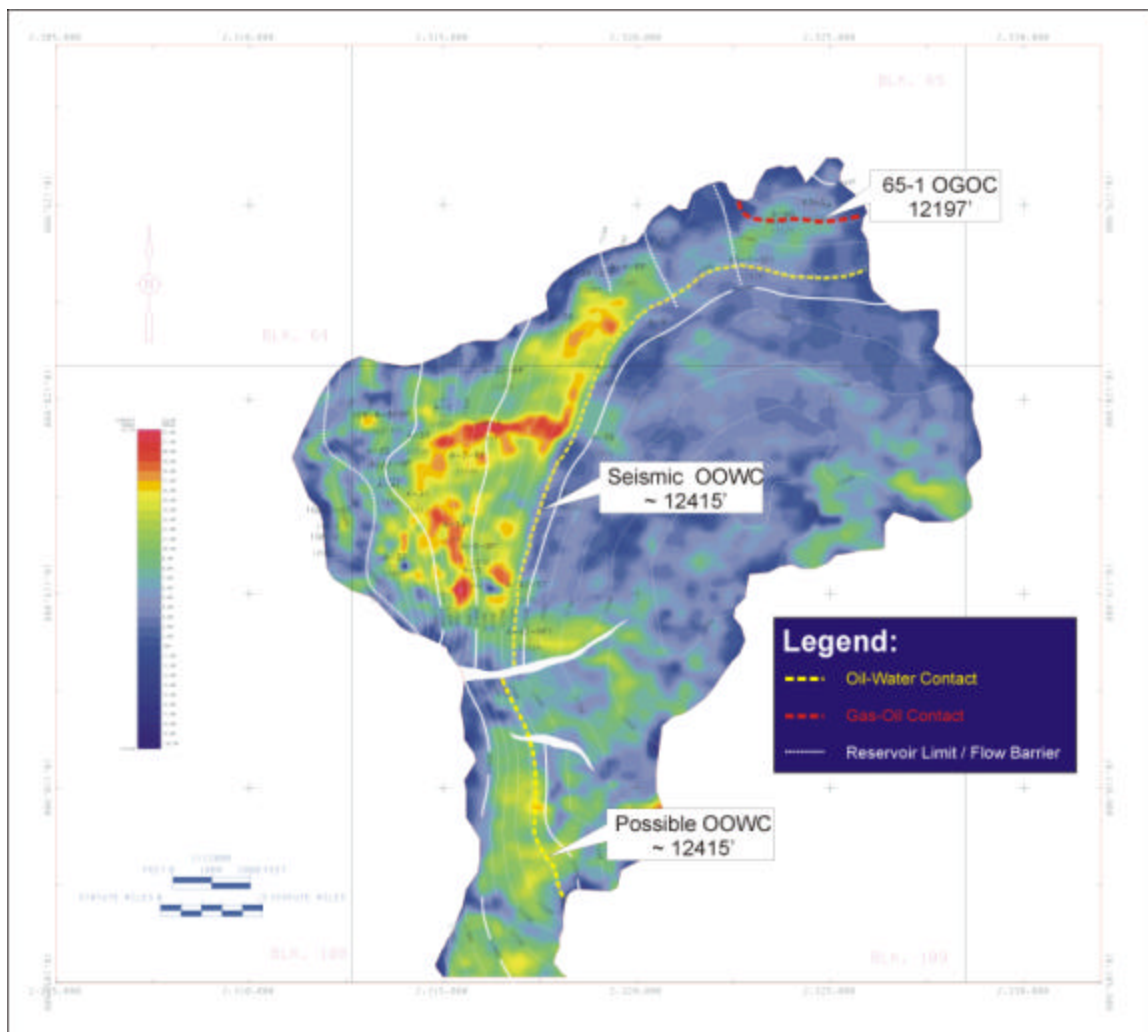


**Figure B-19:** 1988 E-W HF J2 amplitude and structure map showing well penetrations and original fluid contacts. Bright colors represent strongly negative amplitudes.

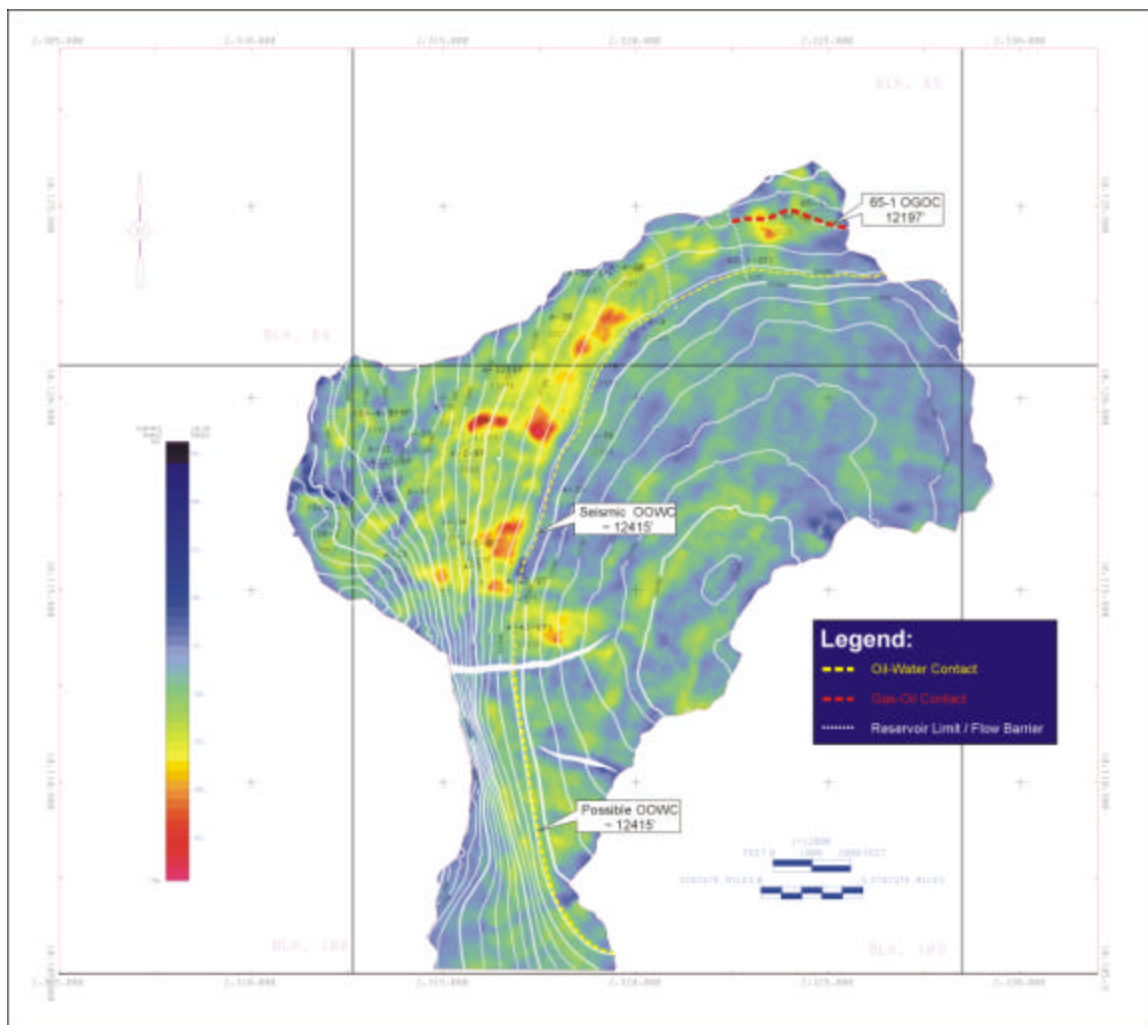


**Figure B-20:** 1988 N-S HF J2 amplitude and structure map showing well penetrations and original fluid contacts. Bright colors represent strongly negative amplitudes.

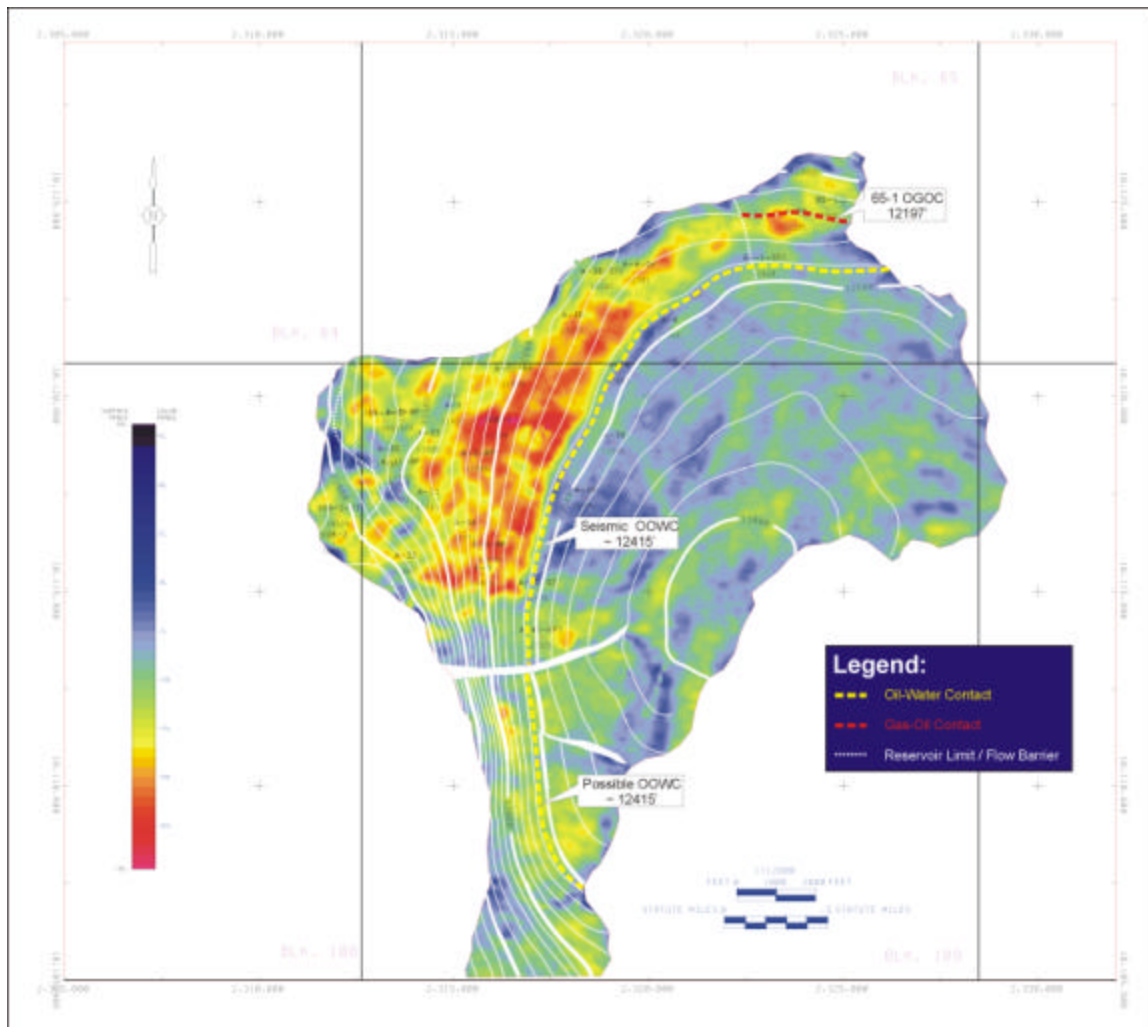


**Figure B-21:** 1988 N-S LF J2 amplitude and structure map showing well penetrations and original fluid contacts. Bright colors represent strongly negative amplitudes.



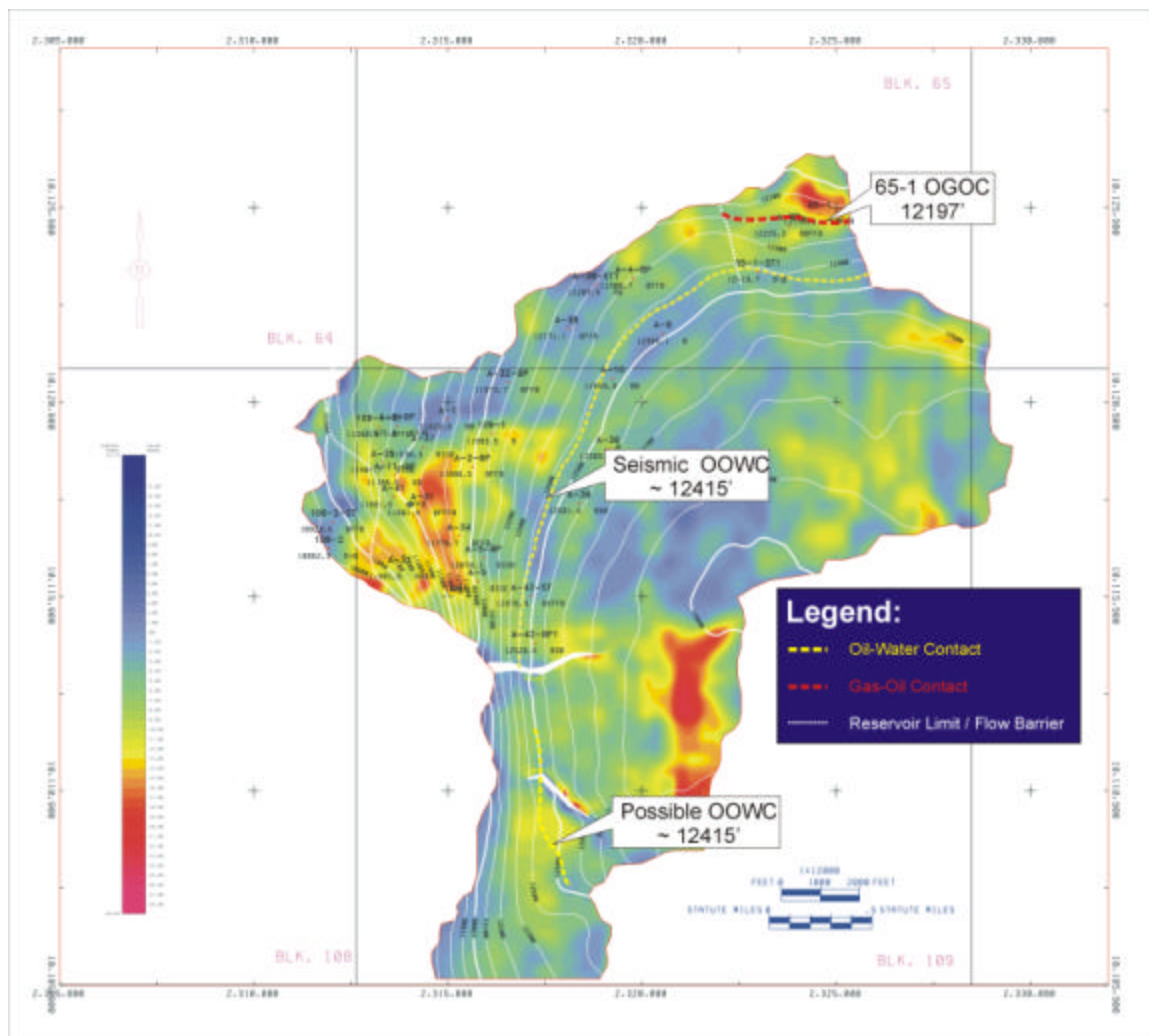


**Figure B-22:** 1997 J2 amplitude and structure map showing well penetrations and original and 1997 fluid contacts. Bright colors represent strongly negative amplitudes.



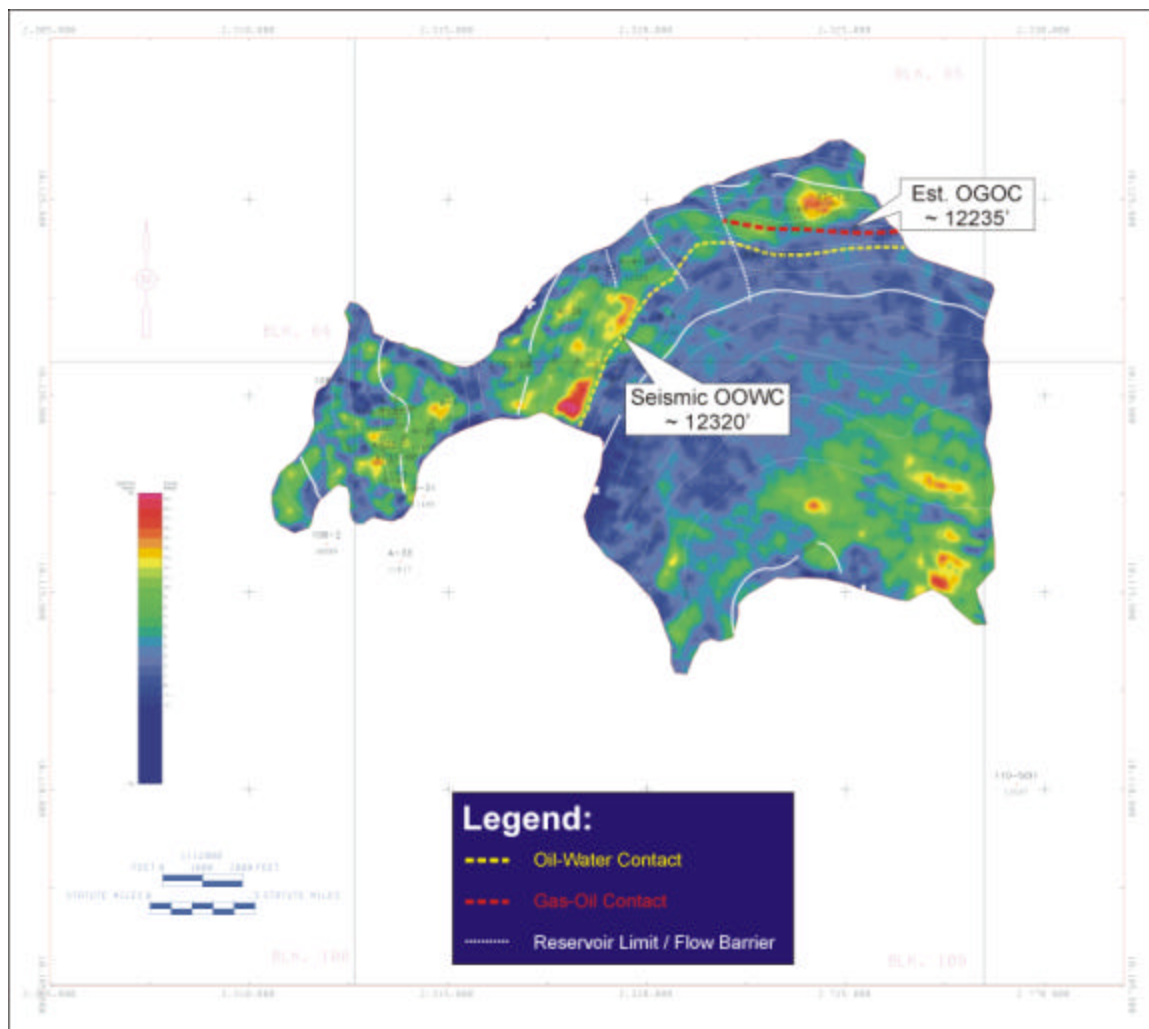


**Figure B-23:** 1988 E-W HF J1 amplitude and structure map showing well penetrations and original fluid contacts. Bright colors represent strongly negative amplitudes.

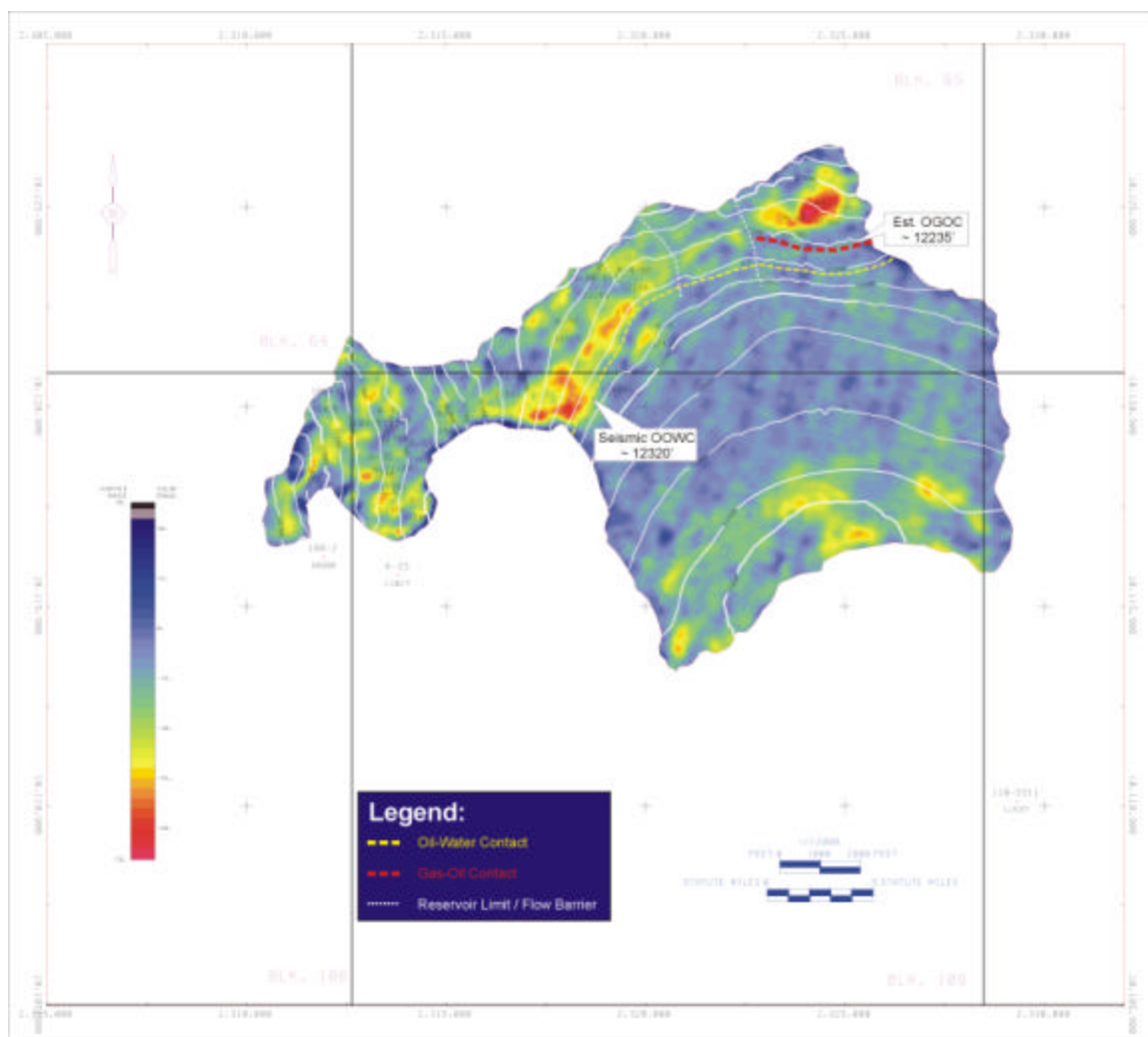


**Figure B-24:** 1988 N-S HF J1 amplitude and structure map showing well penetrations and original fluid contacts. Bright colors represent strongly negative amplitudes.

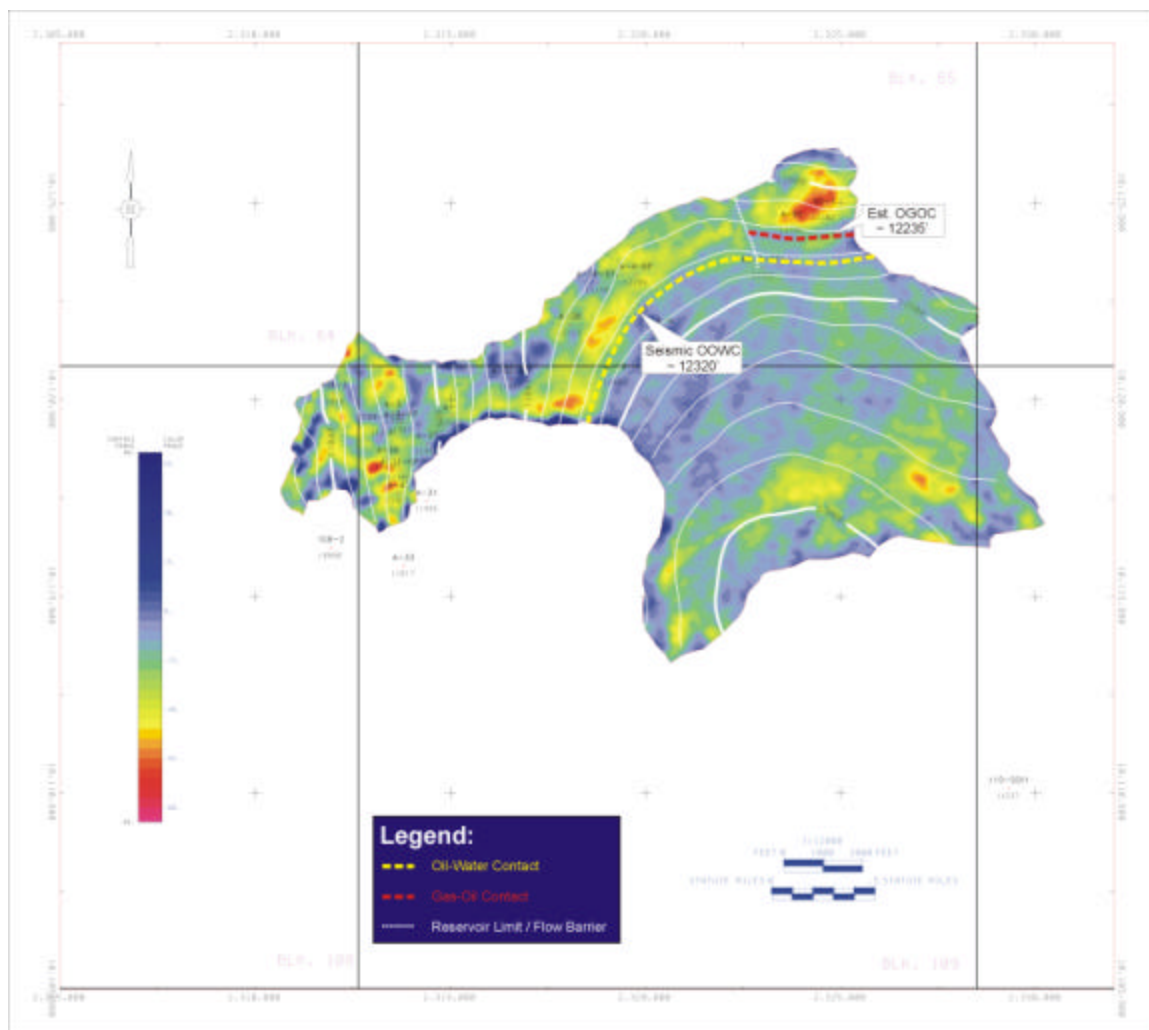


**Figure B-25:** 1988 N-S LF J1 amplitude and structure map showing well penetrations and original fluid contacts. Bright colors represent strongly negative amplitudes.

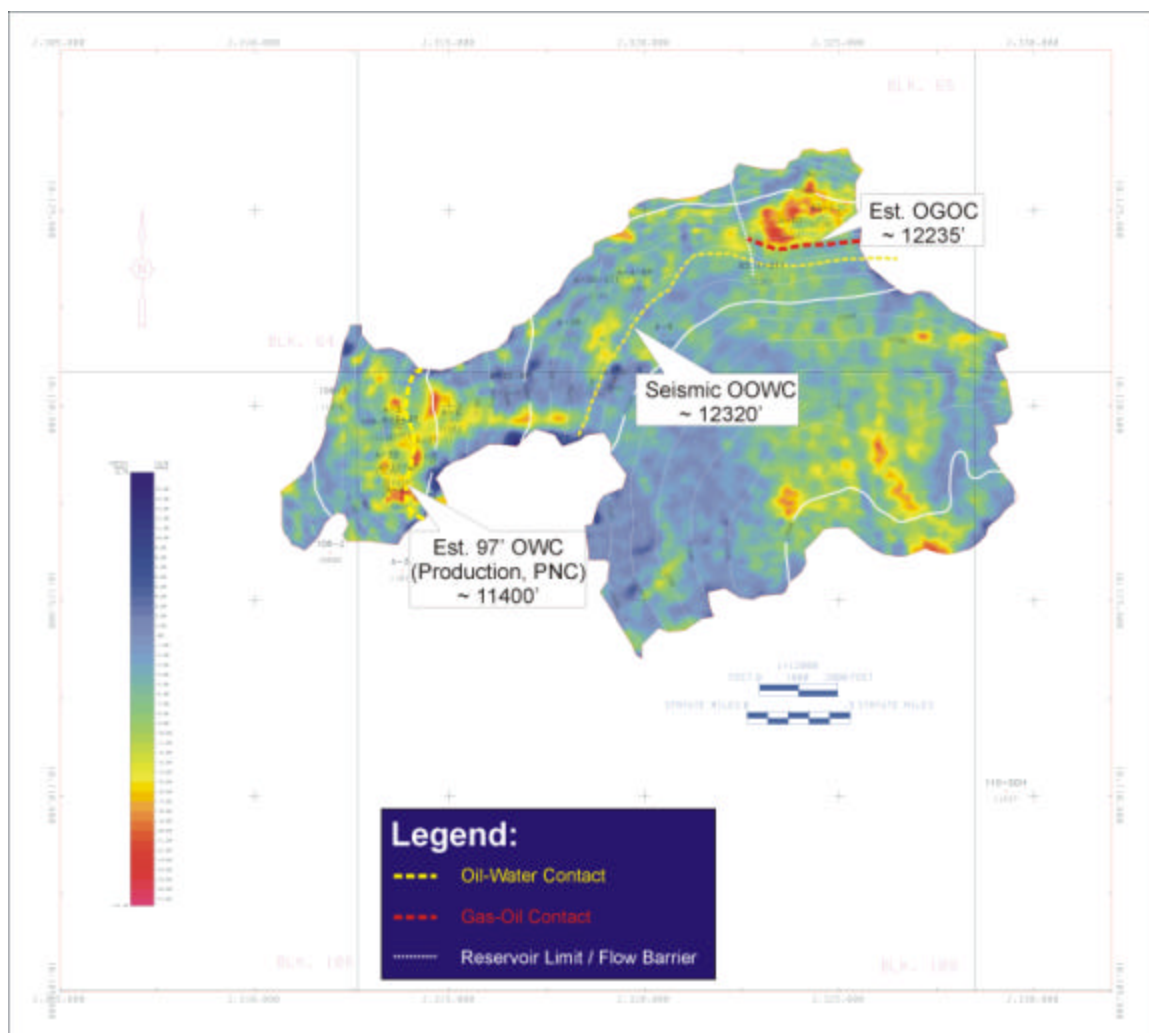


**Figure B-26:** 1997 J1 amplitude and structure map showing well penetrations and original and 1997 fluid contacts. Bright colors represent strongly negative amplitudes.

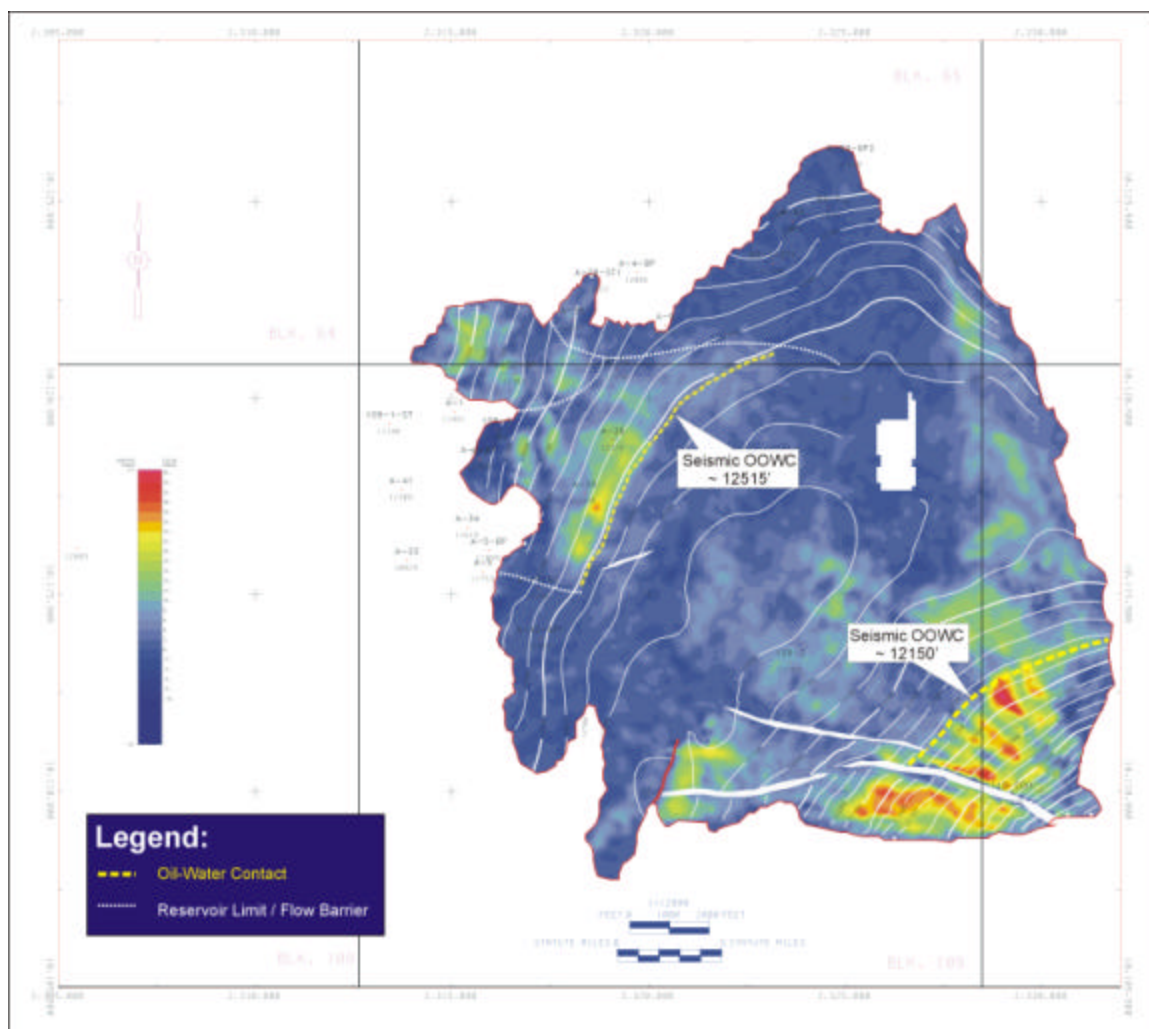


**Figure B-27:** 1988 E-W HF I10 and Rocky amplitude and structure Map showing well penetrations and original fluid contacts. Bright colors represent strongly negative amplitudes.

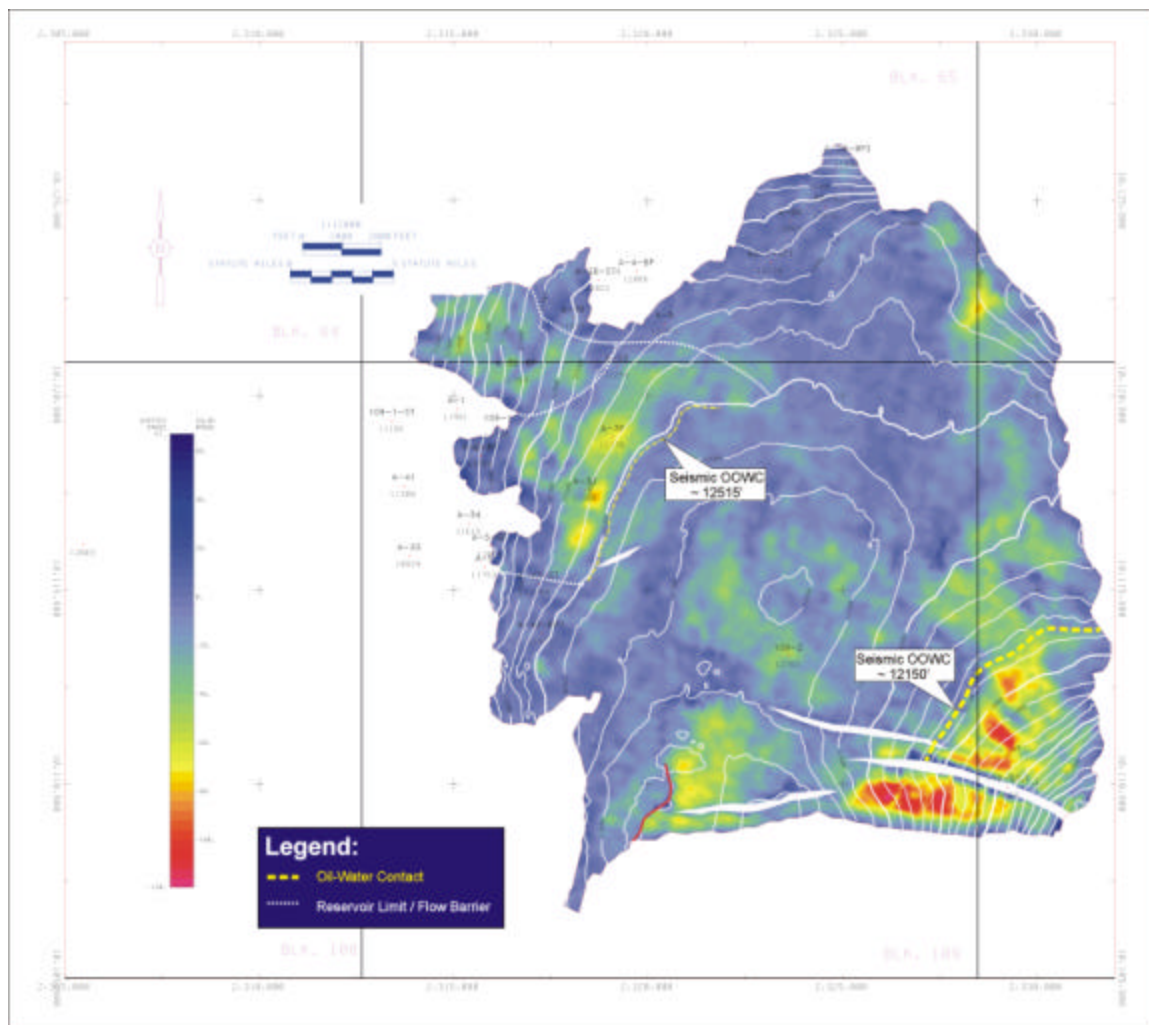
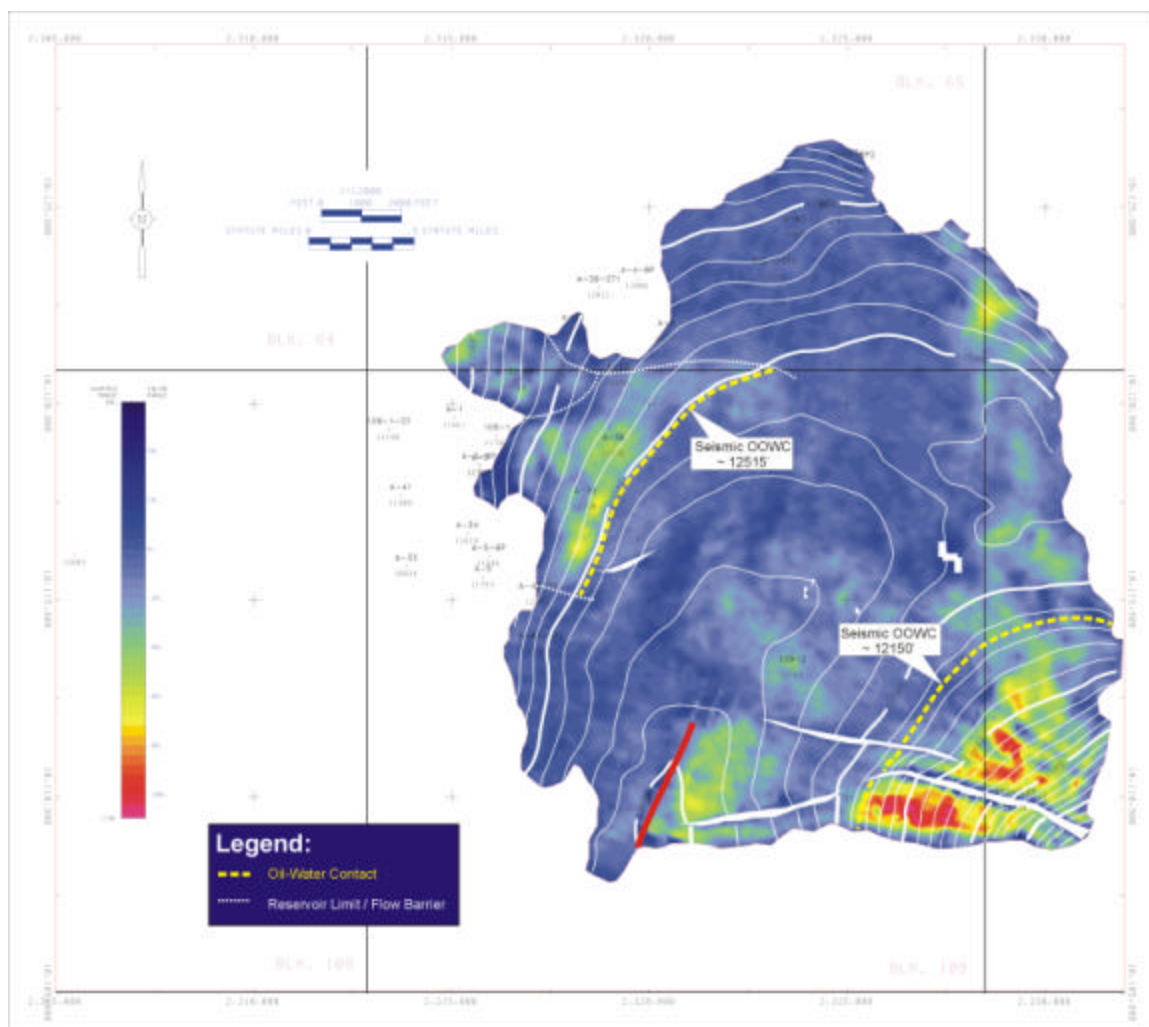


**Figure B-28:** 1988 N-S HF I10 and Rocky amplitude and structure map showing well penetrations and original fluid contacts. Bright colors represent strongly negative amplitudes.





**B-29:** 1988 N-S LF I10 and Rocky amplitude and structure map showing well penetrations and original fluid contacts. Bright colors represent strongly negative amplitudes.

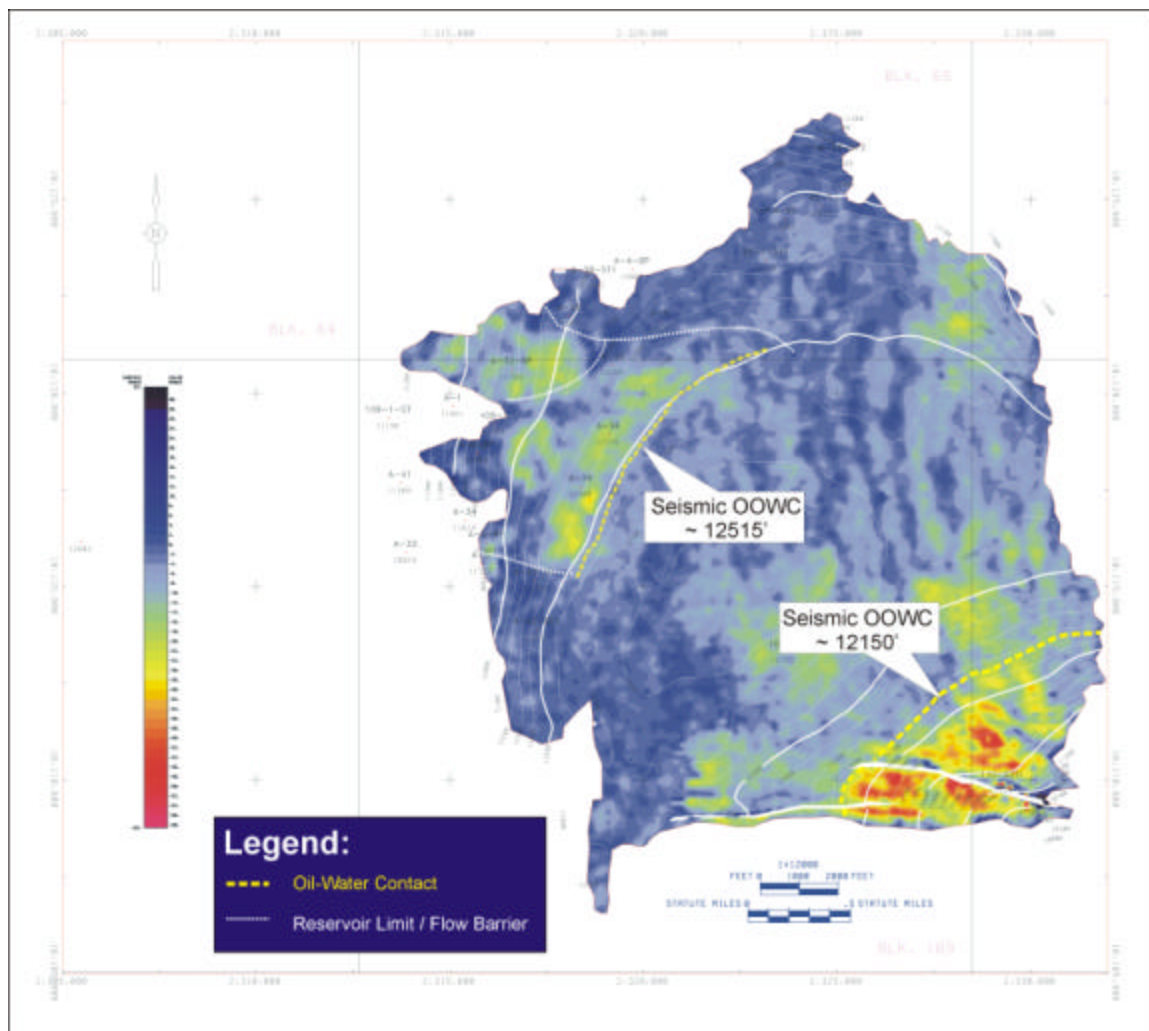


**Figure B-30:** 1997 I10 and Rocky amplitude and structure map showing well penetrations and original fluid contacts. Bright colors represent strongly negative amplitudes.



**Table B-1:** Appendix B Nomenclature

<b>Variable</b>	<b>Description</b>	<b>Dimensions</b>
$l$	Dominant wavelength of seismic survey	L
$n$	Dominant frequency of seismic survey	T <sup>-1</sup>
$w$	Angular frequency	T <sup>-1</sup>
$E$	Depth error at well location ( $E = W-H$ )	L
$F$	Fourier Transform	-
$F(w)$	Frequency-domain representation of time series	-
$f(x)$	Time-domain representation of time series	-
$H$	Actual horizon depth at well location	L
$j$	Square-root of -1	-
<i>Min Thickness</i>	Minimum resolvable layer thickness	L
$v_p$	Acoustic (P-wave) velocity	L/T
$W$	Value of horizon depth grid at well location	L

**Table B-2:** Comparison of minimum resolvable layer thickness at 3.5s TWT in the four surveys.

<b>Survey</b>	<b>Approx. Dominant Frequency (Hz)</b>	<b>Dominant Wavelength (m)</b>	<b>Minimum Resolvable Thickness (m)</b>
1988 E-W HF	30	67	17
1988 N-S HF	30	67	17
1988 N-S LF	10	200	50
1997	18	111	28

## REFERENCES

- Batzle, M., and Wang, Z., 1992, Seismic properties of pore fluids: *Geophysics*, **57**, 1396-1408.
- Berni, A. J., Barros, J. C., Kohli, M., Stellman, T. A., and Perdy, G. E., 1997: On the use of data transformation filters in time-lapse imagery: *Offshore Tech. Conf., Proceedings*, OTC paper 8291, 153-160.
- Burkhart, T., Hoover, A. R., and Flemings, P. B., 2000, Time-lapse (4-D) seismic monitoring of primary production of turbidite reservoirs at South Timbalier Block 295 field, offshore Louisiana, Gulf of Mexico: *Geophysics* **65**, 351-367.
- Davies, P., and Warner, M., 1999, Non-linear cross-equalization of seismic surveys acquired with different bandwidths: 69th Ann. Internat Mtg., Soc. Expl. Geophys., Expanded Abstracts, 1687-1690.
- Deshpande, A., and Flemings, P. B., 1997, Quantifying lateral heterogeneities in fluvio-deltaic sediments using three-dimensional reflection seismic data: *Offshore Gulf of Mexico: J. Geophys. Res.*, **102**, 15 385-15 401.
- Flemings, P. B., Comisky, J. T., Liu, X., and Lupa, J. A., 2001, Stress-controlled porosity in overpressured sands at Bullwinkle (GC65), deepwater Gulf of Mexico: *Offshore Tech. Conf., Proceedings*, OTC paper 13103.
- Gardner, G. H. F., Wang, S. Y., Pan, N D., and Zhang, Z., 1986, Dip Moveout and Prestack Imaging: *Offshore Tech. Conf., Proceedings*, OTC paper 5158.
- Gassmann, F., 1951, Elastic waves through a packing of spheres: *Geophysics*, **16**, 673-685.

- Holman, W. E., and Robertson, S. S., 1994, Field development, depositional model, and production performance of the turbiditic “J” Sands at prospect Bullwinkle, Green Canyon 65 Field, outer-shelf Gulf of Mexico: GCSSEPM Foundation 15th Annual Research Conference, Submarine Fans and Turbidite Systems, December 4-7, 139-150.
- Harris, P. E., and Henry, B., 1998, Time-lapse processing: A North Sea case study: 68th Ann. Internat Mtg., Soc. Expl. Geophys., Expanded Abstracts, 1-4.
- Hoover, A. R., Burkhart, T., and Flemings, P. B., 1999, Reservoir and production analysis of the K40 sand, South Timbalier 295, offshore Louisiana, with comparison to time-lapse (4-D) seismic results: AAPG Bulletin, **83**, 1624-1641.
- Johnston, D. H., Eastwood, J. E., Shyeh, J. J., Vauthrin, R., Khan, M., and Stanley, L. R., 2000, Using legacy seismic data in an integrated time-lapse study: Lena Field, Gulf of Mexico: The Leading Edge, **19**, No. 3, 294-302.
- Jones, T.C., 2001: Personal Communication.
- Koster, K., Gabriels, P., Hartung, M., Verbeek, J., Deinum, G., and Staples, R., 2000, Time-lapse seismic surveys in the North Sea and their business impact: The Leading Edge, **19**, No. 3, 286-293.
- Kragh, E., and Christie, P., 2001, Seismic Repeatability, Normalized RMS and Predictability: 71th Ann. Internat. Mtg., Soc. Expl. Geophys., Expanded Abstracts, RC 4.6.
- Kikani, J., and Smith, T. D., 1996, Recovery optimization and Modeling depletion and fault block differential at Green Canyon 110: Soc. Ptr. Eng. J., 366693, 157-170.

- Kristiansen, P., Christie, P., Bouska, J., O'Donovan, A., Westwater, P., Thorogood, E., 2000, Foinaven 4-D: Processing and analysis of two designer 4-Ds: 70th Ann. Internat. Mtg., Soc. Expl. Geophys., Expanded Abstracts, RC 3.2.
- Landrø, M., Solheim, O. A., Hilde, E., Ekren, B. O., and Stronen, L. K., 1999, The Gulfaks 4D seismic study: *Petroleum Geoscience*, **5**, 213-226.
- Landrø, M., 2001, Discrimination between pressure and fluid saturation changes from time lapse seismic data: *Geophysics*, **66**, No. 3, 836-844.
- Leggott, R. J., Williams, R. G., and Skinner, M., 2000, Co-location of 4D seismic data in the presence of navigational and timing errors: *The Leading Edge*, **19**, No. 3, 303-307.
- Lumley, D. E., 2001, Time-lapse seismic reservoir monitoring: *Geophysics*, **66**, No. 1, 50-53.
- O'Connell, J. K., Kohli, M. and Amos, S., 1993, Bullwinkle: A unique 3-D experiment: *Geophysics*, **58**, No.1, 167-176.
- Oppenheim, A. V., and Schaffer, R. W., 1999, *Discrete-Time Signal Processing*: Prentice Hall Inc.
- Ricker, W. E., 1973, Linear regressions in fishery research: *J. Fisheries Res. Board Canada*, **30**, 409-434.
- Rickett, J., and Lumley, D. E., 2001, A cross-equalization processing flow for time-lapse seismic reservoir monitoring: A case study from the Gulf of Mexico: *Geophysics*, **66**, No. 4, 1015-1025.
- Robinson, E. A., and Treitel, S., 1967: *Principles of digital Wiener filtering*: *Geophys. Pros.*, **15**, 312-333.

- Ross, C.P., Cunningham, G. B., and Weber, D.P., 1996, Inside the cross-equalization black box: *The Leading Edge*, **15**, No. 11, 1233-1240.
- Sherriff, R. E., and Geldart, L. P., 1995, *Exploration Seismology*: Cambridge Univ. Press
- Smith, P., Berg, J. I., Eidsvig, S., Magnus, I., Verhelst, F., and Helgeson, J., 2001, 4-D seismic in a complex fluvial reservoir: The Snorre feasibility study: *The Leading Edge*, **20**, No. 3, 270-276.
- Stephen, R. A., 2000, Ambient seismic noise below the deep seafloor: *The Leading Edge*, **19**, No. 3, 276-281.
- Wang, Z., and Hirsche, W. K., and Sedgwick, G., 1991, Seismic monitoring of water floods? A petrophysical study: *Geophysics*, **56**, 1614-1623.
- Yilmaz, O., 1987. *Seismic Data Processing, Investigations in Geophysics*, v. 2, p. 468-469.